University of Tennessee, Knoxville
Trace: Tennessee Research and Creative Exchange

Masters Theses | Graduate School

5-2013

Quantifying the Relationship Among Ground Penetrating Radar Reflection Amplitudes, Horizontal Sub-Wavelength Bedrock Fracture Geometries, and Fluid Conductivities

Carolyn Morgan Tewksbury-Christle
ctewksbu@utk.edu

Recommended Citation

Tewksbury-Christle, Carolyn Morgan, "Quantifying the Relationship Among Ground Penetrating Radar Reflection Amplitudes, Horizontal Sub-Wavelength Bedrock Fracture Geometries, and Fluid Conductivities. " Master's Thesis, University of Tennessee, 2013.
https://trace.tennessee.edu/utk_gradthes/1702

This Thesis is brought to you for free and open access by the Graduate School at Trace: Tennessee Research and Creative Exchange. It has been accepted for inclusion in Masters Theses by an authorized administrator of Trace: Tennessee Research and Creative Exchange. For more information, please contact trace@utk.edu.

To the Graduate Council:

I am submitting herewith a thesis written by Carolyn Morgan Tewksbury-Christle entitled "Quantifying the Relationship Among Ground Penetrating Radar Reflection Amplitudes, Horizontal Sub-Wavelength Bedrock Fracture Geometries, and Fluid Conductivities." I have examined the final electronic copy of this thesis for form and content and recommend that it be accepted in partial fulfillment of the requirements for the degree of Master of Science, with a major in Geology.

Gregory S. Baker, Major Professor

We have read this thesis and recommend its acceptance:

James A. Mason, Edmund Perfect

Accepted for the Council:
Dixie L. Thompson

Vice Provost and Dean of the Graduate School

(Original signatures are on file with official student records.)

Quantifying the Relationship Among Ground Penetrating Radar Reflection Amplitudes, Horizontal Sub-wavelength Bedrock Fracture Geometries, and Fluid Conductivities

A Thesis Presented for the
Master of Science
Degree
The University of Tennessee, Knoxville

Carolyn Morgan Tewksbury-Christle
May 2013

Copyright © 2013 by Carolyn Morgan Tewksbury-Christle
All rights reserved.

DEDICATION

For my husband, for his unwavering support and tireless help throughout this entire process; for my grandfather, who introduced me to science practically before I could walk; for my parents, for taking me into the field and allowing me to carry around equal parts of My Little Ponies and rocks and for being editors, sounding boards, and tech support; and for my pets, for always knowing the perfect time to sprawl out in the middle of my work.

ACKNOWLEDGEMENTS

I would like to thank my advisor and committee for all of their advice and help throughout this project. My advisor's mentoring allowed me to tackle and complete a project that is in a different field than any of my previous research. The outside expertise brought to this project by my committee was invaluable in helping me formulate the project as a whole. I would also like to thank my field help; the 800-pound blocks would have been impossible to manage on my own. This research was partially funded by the Jones/Bibee Endowment in Geophysics and could not have been accomplished without it.

ABSTRACT

Accurate characterization of subsurface fractures is indispensible for contaminant transport and fresh water resource modeling because discharge is cubically related to the fracture aperture; thus, minor errors in aperture estimates may yield major errors in a modeled hydrologic response. Ground penetrating radar (GPR) has been successfully used to noninvasively estimate fracture aperture for sub-horizontal fractures at outcrop scale, but limits on vertical and horizontal resolution are a concern. Theoretical formulations and field tests have demonstrated increased GPR amplitude response with the addition of a saline tracer in a sub-millimeter fracture; however, robust verification of existing theoretical equations without an accurate measure of aperture variation across a fracture surface is difficult. The work presented here is directed at better verification of theoretical predictions of GPR amplitude and phase response. For sub-vertical resolution features, the response of a 1000 MHz PulseEKKO Pro transducer to a fluid-filled bedrock fracture analog composed of two plastic (UHMW-PE) blocks was measured, where fracture aperture ranged from 0-40 ± 0.3 mm and fluid conductivity from 0-5700 ± 5 mS/m. The GPR profiles were acquired down the centerline of the block, horizontally stacked to reduce errors, normalized to the control response at zero aperture, used to calculate reflection coefficient by dividing by the magnitude of the direct wave, and used to calculate the instantaneous phase. For sub-horizontal resolution features, lateral fracture extent ranged from 0-20 cm and fluid conductivity from 20-5700 ± 5 mS/m. GPR

profiles were acquired parallel and perpendicular to the fracture. Comparison of the measured GPR response to analytical and numerical modeling suggests that numerical modeling best predicts both amplitude and phase variations due to changes in fracture aperture and conductivity. The Widess equation combined with an empirically derived scaling factor also predicts GPR amplitude response but not phase. Future applications to inversions of field data to map subsurface fracture networks will rely on easily invertible models, and numerical modeling using GPRMax2D can help develop a theoretical model for computationally effective and accurate inversion.

The views expressed in this thesis are those of the author and do not reflect the official policy or position of the United States Air Force, Department of Defense, or the U.S. Government.

TABLE OF CONTENTS

LIST OF TABLES

LIST OF FIGURES

CHAPTER 1: INTRODUCTION

1.1 Introduction

Groundwater flow is strongly controlled by anisotropy and heterogeneities in the subsurface. Fracture networks are one of the most pervasive forms of heterogeneities in bedrock, and because discharge has a cubic relationship with fracture aperture, even small fractures can significantly affect groundwater flow (Lamb, 1932; Snow, 1969). Although modeling of contaminant transport in fractured bedrock does incorporate fracture networks, errors in input fracture geometry result in significant errors in calculated discharge. A two-fold error in fracture aperture will result in an eight-fold error in discharge; therefore, characterization of fracture networks in the subsurface, including aperture and lateral variation in aperture, is crucial for hydrogeologic modeling as applied to both fresh water resources and contaminant studies (Berkowitz, 2002).

Currently, non-geophysical methods for estimating fracture geometry rely on the drilling and inspection of cores, borehole cameras, hydrologic pumping tests, and/or the surface expression/exposure of geologic materials (Berkowitz, 2002). These techniques either measure fracture aperture at a few discrete points or measure an average aperture over a discrete distance from a borehole. For typical data analysis of non-geophysical methods, surface expression in the form of a 2D trace map or borehole measurements in the form of 1D scans of fracture exposures are used to generate Monte Carlo realizations of fracture patterns with

the same statistical distribution and observed exposure (Berkowitz, 2002). This may work well for fracture geometry distribution, but fracture aperture must still be extrapolated or inferred from surface, borehole, or pump-test measurements. Inherent variations in rock structure and strength almost guarantee highly variable apertures and geometries of the fractures. Incorporating numerous measurements across a site using non-geophysical methods will help further constrain variations in fracture geometry, but increased sampling and analysis is time-limited and cost-intensive.

Geophysical techniques that allow for non-invasive measurements of the subsurface to characterize subsurface fracture networks include electrical resistivity tomography (ERT), seismic reflection, seismic first arrival tomography (SFT or seismic refraction), and Ground Penetrating Radar (GPR). Although each of these techniques can detect fractures, what is important for transport modeling is the ability of the technique to characterize small-scale fracture attributes including location, orientation, and aperture.

Because of the nature of tomography, ERT and SFT data generate cross-sections or 3D volumes of the best-fit distribution of resistivity and velocity values in the subsurface, respectively, and can be used to identify the presence of fractures. Recent research in azimuthal SFT suggests that velocity is related to the orientation of the seismic line with respect to the fracture, suggesting the

ability to identify fracture orientation and characterize anisotropy of hydraulic conductivity (Edmunds, 2012). Although this technique is promising, the data collection is highly labor-intensive and cannot yet be used to extract specific fracture attributes. LaBrecque et al. (2004) demonstrated fracture identification, but not attribute characterization, using ERT, while Robinson et al. (2012) developed an accurate inversion scheme of cross-borehole ERT data to characterize variations in groundwater conductivity given *a priori* knowledge of fracture location and aperture. These techniques help locate fractures and constrain current contaminant locations in the subsurface but still have significant limitations, either in terms of a reduced spatial resolution or a reduced spatial coverage.

Seismic reflection and GPR both produce cross-sectional images of the subsurface that illuminate interfaces between layers having contrasting geophysical properties. Vibrational elastic waves (seismics) or electromagnetic waves (GPR) reflect from an interface at a contrast boundary and produce an energy return to the receiver.

For the GPR technique, the phase and amplitude of the reflected waves vary due to the contrast between the dielectric permittivities, producing an interpretable image of the subsurface (*see* Section 2.2 and Appendix A for further discussion of GPR). Interfaces are commonly identified by reflection of a portion of the input

wavelet, where each reflected wavelet represents a single interface. Fracture aperture is most simply measured by the time delay between the wavelets reflected from the top and bottom interfaces of the fracture if the distance between the top and bottom of the fracture interface is greater than the resolution, as shown schematically in Figure 1.1. In the limit of small features, therefore, the time offset between the two wavelets decreases to zero. In a landmark paper in 1973, Widess asserted that, for a feature ≤ λ/4 thick for real-world systems (where λ represents the wavelength of the energy wave), the two wavelets are not adequately separated and cannot be identified as discreet. The wavelength of the system, therefore, determines the minimum fracture aperture that may be detected in a given system.

Traditional seismic reflection methods typically use a source with a high frequency range upwards of 40 Hz, so the vertical resolution limit for a typical Earth material would be approximately 10 m. Research on characterizing beds smaller than the resolution, 'thin-beds,' has improved measurement of those features for oil and gas prospecting applications (e.g. Puryear and Castagna, 2008). The improved resolution limit is now commonly expressed as ~λ/16, or approximately 0.6 m for traditional seismic applications. This improvement, however, is still not small enough to accurately measure fracture apertures for near-surface, hydrogeologic applications.

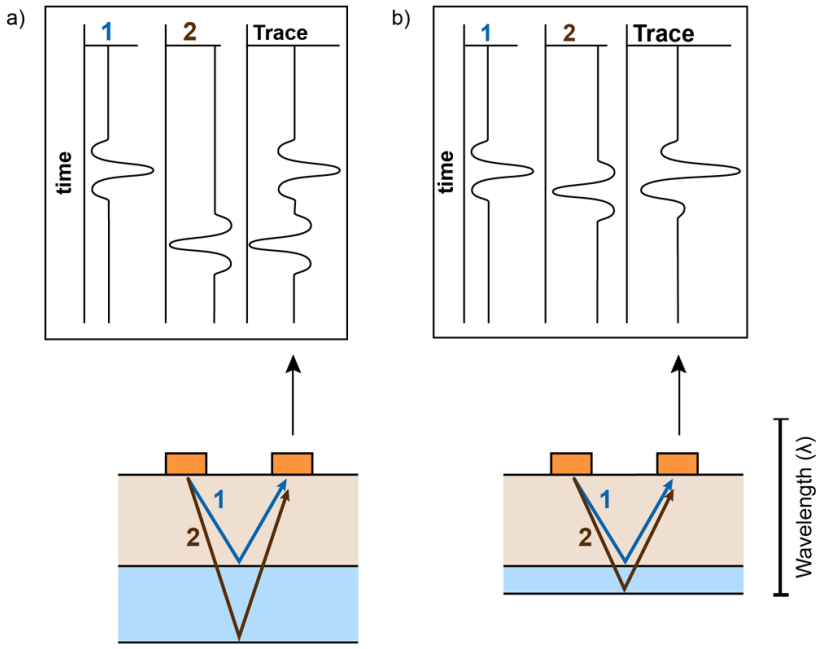

Figure 1.1. Example GPR response to a layer larger than the resolution limit (a) and smaller than the resolution limit (b). The wavelets are easily identifiable when the layer is large enough (a) and the thickness of the layer is simply measured as the time difference between the two peaks. If the layer is smaller than the resolution length, the wavelets interfere, and the response from each one cannot be adequately separated. Widess (1973) asserted that, for features < λ/4 in thickness, the reflected wavelets could not be adequately separated (b).

The typical GPR devices emit an electromagnetic pulse with a set frequency range into the subsurface that subsequently reflects or scatters off interfaces between layers with different dielectric permittivities – e.g. buried targets, discrete lithic layers, or fractures (*see* Section 2.2 and Appendix A). Because GPR uses EM energy rather then acoustic energy as a source, and because of the defining dielectric permittivity values of typical Earth materials, the characteristic wavelength of all GPR systems is significantly shorter than that of seismics. Typically, GPR resolution ranges from millimeters to 10s of centimeters.

As a result of the inherently small signal wavelengths associated with the technique, GPR has been used to characterize subsurface fracture networks for applications in mining, geotechnical engineering, and hydrogeology. For ornamental stone mining purposes, Porsani et al. (2005) mapped fracture sets to determine competent rock areas and more economical placement of explosives for the extraction of blocks. Geotechnical engineering studies examined fracture characterization using GPR as a measurement of rock stability for construction (e.g. Orlando, 2003), rock fall hazard assessment (e.g. Jeannin et al., 2006), restoration (e.g., Leucci et al., 2007), and hazardous waste disposal (Serzu et al., 2004). In hydrogeology, results from a GPR survey determined fracture orientation, connectivity, and aperture (Day-Lewis et al., 2003) for improved calibration of hydrologic models of contaminant transport through fractured media.

Although GPR resolution is better than that of seismics due to the characteristic wavelength, the resolution is still limited, and, because discharge through a fracture is strongly controlled by fracture aperture, identification and characterization of sub-resolution fractures in the subsurface is imperative. The research presented here includes the means to extract both fracture aperture and lateral variations in fracture aperture for subhorizontal fractures, including those much smaller than the current predicted resolution limit, from GPR data.

1.2 Motivation

Due to the cubic relationship between fracture aperture and discharge—a doubling in a fracture's aperture increases the related discharge by a factor of eight—errors in characterization of fracture networks for modeling of contaminant transport or groundwater resources, either through omission of small fractures or error in fracture aperture, can lead to significant errors in calculated discharge. The GPR technique provides the best coverage and resolution out of the available techniques but still has an inherent resolution limit predicted at λ/4 (Widess, 1973) when using standard interpretation techniques on a GPR cross-section. The wavelength of a GPR system is inversely related to the dielectric permittivity of the material and the frequency of the antennas used for acquisition. Although increasing the frequency can improve the inherent resolution, it decreases the depth of penetration, limiting applicability. Given the above, characterization of both small fractures and small variations in fracture aperture seems unlikely.

Below the resolution limit of λ/4 defined by Widess (1973), however, wavelets reflected from the top and bottom of the fracture interfere constructively and destructively (*see* Figure 1.1). Although the wavelets cannot be adequately separated, interference does change the amplitude and phase of the reflected wave. Equations derived by Widess (1973), Hollender and Tillard (1998), and

Annan (2005a) predict variations in the maximum reflected amplitude and phase of the superimposed reflected wavelets due to both interface separation and the contrast between the dielectric permittivity of each layer. These theoretical equations can be inverted to allow determination of fracture aperture for given a dielectric permittivity of the fracture fill and can, therefore, be used to characterize sub-resolution fractures in field data.

Deparis and Garambois (2009) used the Hollender and Tillard (1998) equation in conjunction with amplitude variation measured with offset (AVO). In an AVO study, increasing separation between GPR antennas changes the angle of incidence of the wave and therefore the nature of the reflection. Results from the Hollender and Tillard equation, applied with Jonscher parameters instead of the typical Fresnel reflection coefficients, agree well with results from a finite-difference, time-domain modeling software, GPRMax2D (Giannopoulos, 2005). Deparis and Garambois (2009) applied the inversion to field data taken over a 12 m Tithonian limestone cliff near Grenoble, France (Jeannin et al., 2006) and proposed probable fracture depth, aperture, and fill based on the inversion.

Sassen and Everett (2009) used a modified version of the Annan (2005a) equation combined with coherency – a measure of lateral variations – and polarimetric transmission GPR data to characterize fractures in the Glen Rose Formation in the Edwards Plateau, Texas. Transmissions through subsurface

interfaces are governed by GPR antenna orientation (*see* Appendix A), so collecting all possible antenna orientations (3D polarimetric) eliminates orientation biases from the data set. Sassen and Everett (2009) identified possible fractures using coherency measurements in the suite of 3D polarimetric data and inverted the data at possible fracture locations. They demonstrated the accuracy of their inversion technique on numerically simulated data for fractures filled with air, mineral, and soils. This technique relies on both a reference transmission that does not intersect the fracture and on the ability to gather transmission profiles instead of reflection profiles at the field site.

These studies suggest that these theoretical equations can be inverted to characterize sub-resolution fractures. Determining whether the equations accurately predict real-world relationships, however, is crucial for field applications. For both of these examples, the researchers characterized fractures based on theoretical equations that have not been verified and, because of natural variations in real-world fracture aperture, cannot be quantitatively verified in the field. Previously derived theoretical equations for GPR amplitude response must be empirically tested over a controlled physical model before a method can be developed for extracting fracture and fluid characteristics directly from field-scale GPR data.

Lab-scale tests over bedrock fracture analogs with controllable and repeatable fracture aperture are needed to determine the applicability of the proposed theoretical equations. Gregoire and Hollender (2004) developed an initial test of the Hollender and Tillard equation using a fracture analog composed of two 2.5 x 1.2 x 0.8 m blocks of granite stacked on top of each other to simulate a fracture. To fill the fracture, they used dry and saturated clay and sand, as well as granite and limestone. Results of their inversion agree well for fracture apertures > λ/4, but do not agree for fracture apertures smaller than the resolution limit. It is unclear whether the discrepancy was caused by the theoretical equation—i.e., the theoretical equation does not represent wave behavior in a real-world system—or their inversion technique.

In a similar experiment, Burns (2008) used a 1.2 m by 1.2 m physical fracture analog constructed from two blocks of ultra-high molecular weight polyethylene (UHMW-PE) plastic stacked on top of each other. He collected data across an air-filled fracture ranging in aperture from 0-300 mm using a 1 GHz GPR transducer. The data demonstrate that the increased GPR reflection amplitudes with increasing fracture aperture are best fit by a modified version of Widess' 1973 equation. At fracture apertures below ~λ/30, however, results oscillate in a consistent manner and are not predicted by any of the theoretical formulations. Use of the physical UHMW-PE model and comparison directly to the theoretical equations by Burns (2008) allowed for controlled testing of the equations

themselves that could not be accomplished in the field due to lack of knowledge of fracture aperture.

For contaminant transport in groundwater, data would be focused on saturated, as opposed to air-filled, fractures, and in practice, the GPR amplitude response would not depend solely on fracture aperture but would also depend on the contrast in dielectric permittivity between the two media. For a liquid-filled fracture, the contrast between dielectric permittivity depends primarily on the conductivity of the fluid. Amplitude of the reflected GPR signal increases with increasing conductivity as well as with increasing aperture, so a high amplitude reflection could be generated by a large fracture filled with air or other low-conductivity fluid, or by a narrow fracture filled with high-conductivity fluid.

Field tests have qualitatively demonstrated increased GPR response to a fracture with an aperture less than $\lambda/4$ with the addition of a saline tracer (e.g., Talley et al., 2005; Tsoflias and Becker, 2008; Becker and Tsoflias, 2010). Talley et al. (2005) monitored propagation of a saline tracer through a sub-horizontal fracture. Presence and flow of the saline tracer was only identified after the subtraction of a background GPR survey taken prior to tracer injection. Tsoflias and Becker (2008) conducted pump tests across the same sub-horizontal fracture with increasing conductivity tracers. GPR antennas were fixed in space, so variations in fracture aperture were constant over different conductivity tests, although the

response does represent an integrated fracture aperture over the illumination footprint—or Fresnel zone—of the GPR reflection. The conductivity of the tracer was only measured at the injection well, and mixing between resident water and tracer within the illuminated segment of the fracture could not be quantified. Though they demonstrated increased amplitude and increasingly negative phase response with increasing tracer conductivities, the relationship between GPR reflection amplitude and conductivity could not be established. Further research employed recirculation to stabilize conductivities between the injection and pumping well (Becker and Tsoflias, 2010). However, due to channelized flow, the conductivity is still likely not constant across the Fresnel zone footprint of the antennas at the fracture location. The amplitude and phase variation for this test is, therefore, still averaged over a range of conductivities. This previous research demonstrates the expected qualitative relationship between conductivity and GPR response - increased response with increasing conductivity - but the governing relationship simply cannot be derived through inherently poorly constrained field-scale testing.

Burns (2008) conducted a study over a single fracture aperture and a range of conductivities from 0 mS/m to 5700 mS/m using the physical analog described previously. His results suggest a bimodal trend between reflection amplitude and conductivity that does not support the qualitative field tests, but this trend was likely due to systematic air bubbles in the fracture.

Furthermore, none of the studies presented previously investigated the aspect of horizontal resolution and lateral variations in fracture aperture. As with vertical resolution, horizontal resolution is related to the time delay between reflected wavelets from two laterally separated targets (*see* Figure 1.2), and the resolution limit is defined with respect to the first Fresnel zone. Theoretical equations, as well as results from Gregoire and Hollender (2004) and Burns (2008) predict changes in the amplitude of the reflected wave below the resolution limit, suggesting similar behavior for lateral variations. Because small changes in fracture aperture can strongly influence discharge, lateral variations are of particular interest for possible field applications as well.

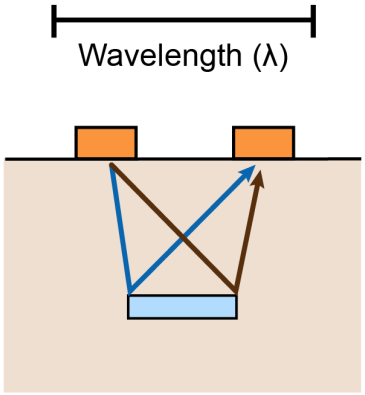

Figure 1.2. Horizontal resolution of a GPR system. If the separation between the two targets is larger than the Fresnel zone, then the time difference between the two reflected wavelets is large enough that they can be separately identified.

Conductivity cannot be adequately controlled or monitored in a field setting, and the aperture distribution of any sizeable "real" fracture in the subsurface cannot be known. A physical analog, therefore, remains the best option for attempting to determine the governing relationship between fracture aperture, lateral variations

in fracture aperture, fluid conductivity, and GPR reflection amplitude and phase. To reiterate, the new research presented here is focused on the analysis of a full suite of data collected for variations in vertical and horizontal fracture aperture and conductivity using a physical bedrock fracture analog. This allowed for robust comparison to results predicted by both theoretically derived equations and established numerical modeling software.

1.3 Objectives

Accurate characterization of fracture aperture below the resolution limit of GPR data relies on understanding how GPR amplitude and phase respond to vertical and horizontal changes in fracture aperture as well as changes in conductivity. Several theoretical formulations have been published but have not been verified. Although Burns (2008) conducted research into verifying the theoretical equations using a physical bedrock fracture analog, he measured the relationship between reflection amplitude and aperture of an air-filled fracture and between reflection amplitude and high conductivity of a 0.5 mm fracture only. Modeling of contaminant transport in groundwater requires characterization of fractures of different apertures filled with fluids of different conductivities and, therefore, requires evaluation of the theoretical equations as applied to fluid-filled fractures.

The research presented here covers three parameters for characterization of subsurface fracture networks: (1) fracture aperture, (2) conductivity of the fluid within the fracture, and (3) lateral extent of the fracture. In particular, the following two questions were used:

- When the fracture aperture is smaller than the vertical resolution limit, which does a better job of predicting the relationship between GPR amplitude and phase, fracture aperture, and fluid conductivity - the theoretical equations or the numerical models?
- When the lateral extent of a fracture is smaller than the horizontal resolution limit, can the fracture still be detected and characterized by examining variations in GPR amplitude and phase response?

To answer these questions, a physical bedrock fracture analog was constructed, composed of two blocks of ultra-high molecular weight polyethylene (UHMW-PE) plastic stacked on top of each other (*see* Figure 1.3). By varying fracture aperture, fluid conductivity, and lateral extent in a controllable and repeatable fashion, the accuracy of the theoretical equations and numerical modeling can be determined.

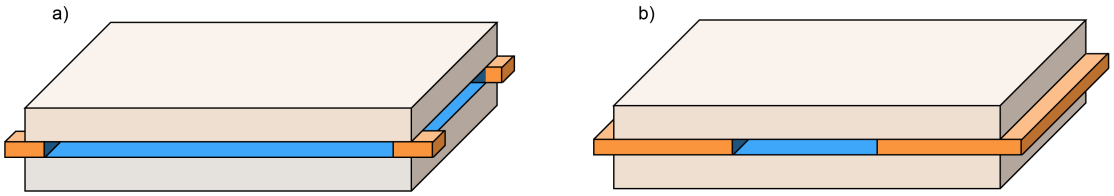

Figure 1.3. In this study, I used a physical bedrock fracture analog composed of two blocks of UHMW-PE plastic (gray above) partially immersed in water (blue) above. Inserts control fracture aperture (a, orange) and fracture lateral extent (b, orange). I investigated GPR amplitude response to variations in fracture aperture (Section 1.3.1 and Chapter 3), fracture lateral extent (Section 1.3.2 and Chapter 4), and fluid conductivity.

1.3.1 Fracture Aperture

To evaluate the accuracy of the theoretical and numerical predictions for GPR response to laterally consistent changes in fracture aperture and fluid conductivity, data were collected across a physical bedrock fracture analog composed of two blocks of UHMW-PE (*see* Figure 1.3). Inserts between the bottom and top of the corners of each block control the fracture aperture, and the blocks are partially immersed in a stock tank of water to saturate the fracture (*see* Figure 1.3a). The conductivity was varied between 0 mS/m (distilled water) to 5700 mS/m (seawater approximation) and selected fracture apertures that are both larger and smaller than the resolution limit of the system were tested. Chapter 3 details test specifications and presents results and discussion.

1.3.2 Lateral Fracture Extent

The ability of GPR data to be used for detecting fractures that are laterally shorter than the horizontal resolution limit is tested by comparing the results to numerical predictions for the same system. For this test, two sheets of UHMW-PE between the top and bottom blocks (*see* Sections 2.1 and 4.3.1 and Figure 1.3b) created a laterally discontinuous fracture with an aperture smaller than the vertical resolution limit. Data was collected over fractures both longer and shorter than the horizontal resolution limit. Chapter 4 details test specifications and presents results and discussion.

1.3.3 Theoretical and Numerical Predictions

The results from the physical bedrock fracture analog were compared to results from three theoretical equations [the Widess (1973), Hollender and Tillard (1998), and Annan (2005a) equations (briefly described in Section 1.2 and covered in depth in Section 2.3)] and an industry-accepted finite-difference, time-domain numerical modeling software [GPRMax2D (Giannopoulos, 2005; covered in depth in Section 2.4)]. The physical characteristics and dimensions needed for the equations and modeling were measured from the physical analog model (Burns, 2008).

Burns (2008) demonstrated that the Widess (1973) equation agreed more closely with data collected over an air-filled fracture than the other two theoretical

equations, and Deparis and Garambois (2009) demonstrated close agreement between the Hollender and Tillard (1998) equation and results from GPRMax2D modeling. These previous studies indicate that results from the new works presented here should reflect a similar relationship – with Widess' (1973) equation best predicting GPR reflection amplitudes and similar results between the Hollender and Tillard (1998) equation and GPRMax2D modeling.

1.4 Hypotheses

This research includes three hypotheses: (1) the reflection amplitude of 1000 MHz GPR radar signal increases with both increasing conductivity and increasing fracture aperture, (2) Widess' equation for reflection amplitude is the best fit for the 1000 MHz data, as suggested by data collected by Burns (2008) and (3) GPR reflection amplitude of 1000 MHz data has a low-slope relationship with conductivity, as predicted by initial modeling.

CHAPTER 2: GEOPHYSICAL TECHNIQUES AND METHODS

Accurate modeling of contaminant transport in groundwater relies on characterization of fracture networks. Ground penetrating radar (GPR) is arguably the best of the available techniques, but as with all reflective wave techniques, it still has limited resolution (Widess, 1973). Proposed theoretical equations have been inverted to characterize sub-resolution fractures (Sassen and Everett, 2009; Deparis and Garambois, 2009) but have not been verified for fluid-filled fractures (Gregoire and Hollender, 2004; Burns, 2008). The research presented here examines GPR response to a sub-resolution horizontal bedrock fracture by comparing results from a physical bedrock fracture analog saturated with a fluid of variable conductivity (in Section 2.1) to the response predicted by theoretical equations (in Section 2.3) and the response shown through numerical models (in Section 2.4).

The three components of this study—real-world GPR data, theoretical equations, and numerical modeling—produce amplitude data in different units. Real-world GPR systems measure the electric field intensity in volts per meter (V/m) and convert to a measure of voltage, in millivolts, of the reflected wave. The theoretical equations calculate the reflection coefficient, which is the percent of the incident wave that is reflected at a given interface. Numerical models calculate the electric field intensity in volts per meter. The numerical modeling cannot be directly compared to the real world data for two reasons. First, the internal conversion cannot be replicated on the numerical data without

proprietary knowledge of the initial wave generation, and second, the numerical modeling does not account for the internal electronics and structure of the transducer antennas. Given knowledge of the incident wave, however, results from both the real-world system and from numerical modeling can be converted to reflection coefficients (described in Sections 2.2.2 and 2.4.1, respectively). All amplitude data are therefore either calculated or converted to reflection coefficients to allow for comparison.

2.1 Physical Bedrock Fracture Analog

Field verification of theoretical equations and numerical modeling of GPR amplitude and phase response is impossible without *a priori* knowledge of the fracture aperture. A lab test using a bedrock fracture analog is a clear solution to this problem. The physical fracture analog allows for the collection of data using real-world systems over measureable, controllable, and repeatable fracture apertures, lateral extents, and fluid conductivity.

The bedrock fracture analog is composed of two 1.2 m x 1.2 m x 0.15 m blocks of ultra-high molecular weight polyethylene (UHMW-PE) plastic stacked on top of each other to form a continuous horizontal fracture (as first described and used in Burns, 2008). The UHMW-PE is an ideal material for a physical fracture analog, because the plastic is homogenous, isotropic, and lossless. Changes in

measured GPR amplitude and phase response are, therefore, solely due to changes in fracture aperture, lateral fracture extent, and/or fluid conductivity. The block's thickness is only accurate to ± 0.3 mm, which introduces an error in the fracture aperture, but inherent spatial averaging of the electromagnetic wave over the GPR footprint, horizontal stacking of the data, and repeatable collection locations all minimize this error.

The standard configuration of the experiment includes: (1) a 2.4 m stock tank, (2) the UHMW-PE blocks placed within the stock tank and partially immersed in water so that the fracture was completely saturated, and (3) a gantry crane and hoist to lift and position the top block (*see* Figure 2.1 and Appendix B for further information on the physical analog). For the fracture aperture test, inserts at each corner control the fracture aperture (*see* Section 3.3.1 and Figure 1.3a), and for testing GPR response to changes in lateral fracture extent, two 6.8 ± 0.2 mm sheets of UHMW-PE between the top and the bottom block form a discontinuous fracture of variable length (*see* Section 4.3.1 and Figure 1.3b).

During data collection for the two main tests, both fluid conductivity and either fracture aperture or lateral extent of the fracture were varied. Because of the use of inserts, the chosen fracture apertures or extents are easily repeatable. Therefore, all data for each aperture or extent were collected at a given conductivity before increasing the conductivity.

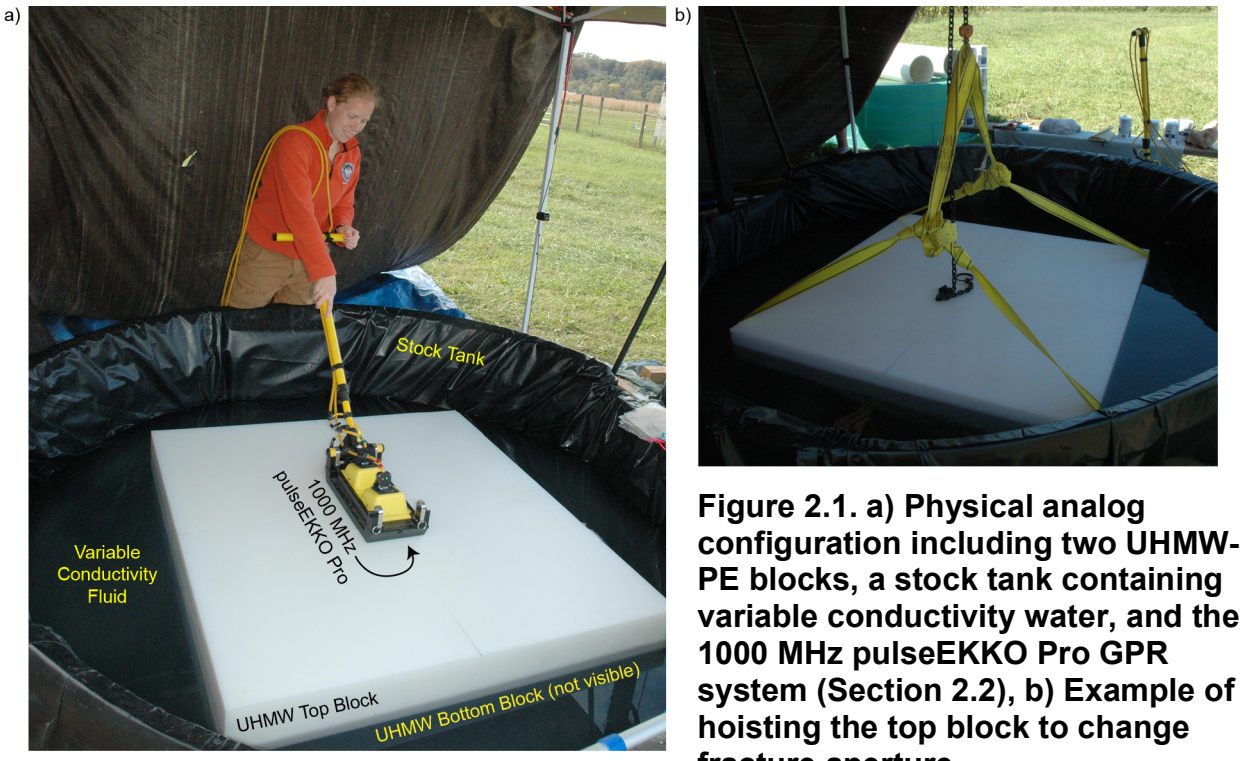

Figure 2.1. a) Physical analog configuration including two UHMW-PE blocks, a stock tank containing variable conductivity water, and the 1000 MHz pulseEKKO Pro GPR system (Section 2.2), b) Example of hoisting the top block to change fracture aperture.

The procedure for changing conductivity maximized homogenization of the water within the fracture. All inserts were removed so that the top block was flush against the bottom, forcing the majority of the water into the stock tank as opposed to having residual water remaining stagnant in the fracture. This procedure also applies to the investigation of fracture lateral extent except that the UHMW-PE sheets were placed flush to one another (*see* Figure 2.2). The fluid conductivity was increased by adding table salt to the existing fluid bath, and then mixing the water by hand and with a submersible pump. The water was allowed to equilibrate for a minimum of 15 minutes. The conductivity was then measured in four locations around the blocks to ensure even homogenization.

Because conductivity is dependent on temperature, the absolute conductance of the water varied throughout the day as air temperatures fluctuated. As an attempt to minimize the fluctuations as much as possible, a portable canopy was deployed over the experimental apparatus. It was determined that temperature changes accounted for the largest error in conductivity, so conductivity was recorded immediately before and after collecting each data set and used to determine the error in conductivity.

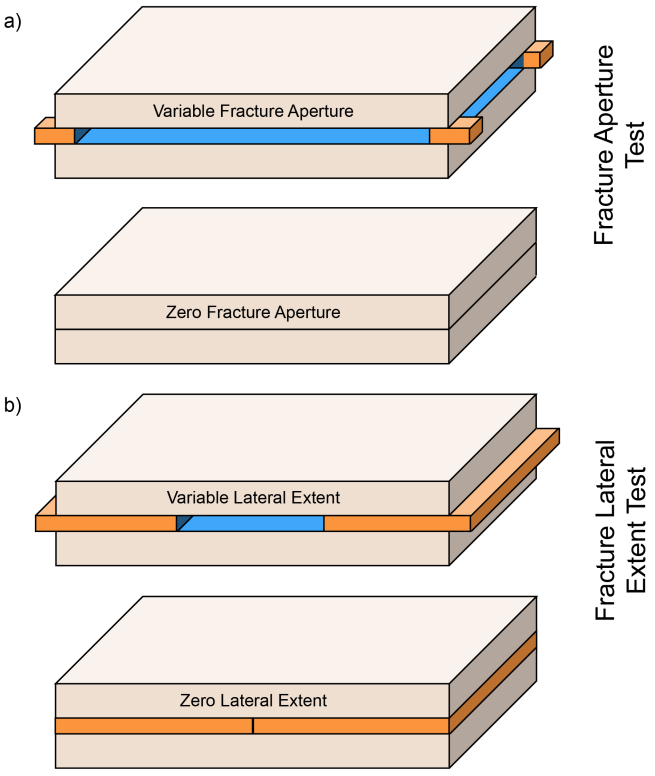

Figure 2.2. a) Block set-up for the fracture aperture test (top) and the zero aperture used to normalize the data (bottom), and b) Block set-up for the lateral extent test (top) and the zero extent used to normalize the data (bottom).

In previous studies, air bubbles within the fracture analog appear to greatly influence the results (Burns, 2008), so a systematic approach was taken to minimize the possibility of air bubbles. After increasing the conductivity, the system was set to the largest fracture aperture or widest lateral extent. The water was circulated within the fracture using a submersible pump to dislodge air bubbles.

2.1.1 Analog Characteristics

GPR wave propagation depends on the electromagnetic properties of the medium (*see* Appendix A). List 2.1 summarizes relevant constants measured from the physical model and used in the analytical and numerical models and indicates measurement techniques or sources of the information.

List 2.1. Relevant constants used in theoretical equations and numerical modeling.

UHMW-PE Characteristics

Depth to the interface (D) (measured)	0.152 m
Relative dielectric permittivity (ε_r) (measured by Burns, 2008)	2.0
Conductivity (σ_i) (Boedeker Plastics: Polyethylene Datasheet, 2013)	$<10^{-16}$ S/m
Magnetic permeability (μ_i) (Baker et al., 2007; Annan, 2005a)	$4\pi \times 10^{-7}$ H/m

Fluid Characteristics

Layer thickness (d) (measured)	*see* List 3.1

Relative dielectric permittivity (ε_r) (Baker et al., 2007)	80
Conductivity (σ_i) (measured)	*see* List 3.1
Magnetic permeability (μ_i) (Baker et al., 2007; Annan, 2005a)	$4\pi \times 10^{-7}$ H/m

Soil Characteristics

Layer thickness (d) (not measured, only used in numerical modeling)	0.5 m
Relative dielectric permittivity (ε_r) (Baker et al., 2007)	4.0
Conductivity (σ_i) (Grisso et al., 2009)	10 mS/m
Magnetic permeability (μ_i) (Baker et al., 2007; Annan, 2005a)	$4\pi \times 10^{-7}$ H/m

GPR Characteristics (all set through the Sensors & Software system)

Center frequency (f)	1000 MHz
Antenna separation (S)	0.15 m
Step size	0.01 m
Sampling interval	0.1 ns
Stacking	32

Constants (Baker et al., 2007)

Speed of light (c)	299,792,458 m/s
Dielectric permittivity of free space (ε)	8.854 x 10^{-12} F/m
Magnetic permeability of free space (μ_0)	4π x 10^{-7} H/m

2.2 Ground Penetrating Radar

A propagating EM wave generated by a GPR transmitter responds to changes in the electromagnetic properties in the subsurface (*see* Appendix A for further discussion). Consider a simple case of a point target imbedded in a homogenous, isotropic medium. The transmitting antenna emits a pulsed electromagnetic wavelet of a given frequency range into the subsurface (step 1 in Figure 2.3a). The wavelet propagates through the medium and reflects off the point target (step 2 in Figure 2.3a). Some reflected energy reaches the receiving antenna (step 3 in Figure 2.3a), and the time delay between pulse emission and pulse reception, combined with propagation velocity of the medium, is a measure of the depth of the target.

No target in real world applications, however, is a true point target, and the actual lateral and vertical extent of the target complicates the behavior of the wavelet. When a wavelet crosses an interface between materials of differing EM properties, a portion of the wave is reflected and a portion is transmitted (step 1

in Figure 2.3b). The contrast between dielectric permittivities of the medium and the target governs both how much of the wavelet energy is reflected and transmitted and the phase of the reflected and transmitted wave. The reflected wave returns to the receiving antenna, and the transmitted wave propagates through the subsurface until it encounters another interface (step 2 in Figure 2.3b). As with a point target, the time delay from emission to reception is a measure of depth of the interface.

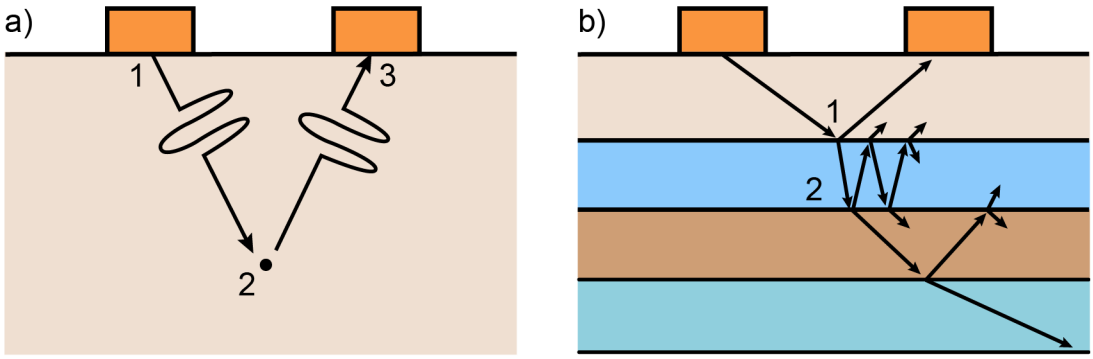

Figure 2.3. a) Diagram showing GPR reflection from a point target. The transmitting antenna emits a pulse (1) that reflects off the target (2) and returns to the receiving antenna (3), and b) More complex reflections occur in a layered system. At each interface, a portion of the incident wave is reflected and transmitted (1). The transmitted wave continues through the subsurface and is reflected and transmitted from each subsequent interface (2).

A single GPR measurement produces a 'trace,' which is a time-series measurement of recorded energy (*see* Figure 2.4a). A homogeneous media would generate no reflections, and the trace would show no anomalies, whereas a single interface would return a scaled version of the emitted wavelet. In

complex stratigraphy, the trace is composed of several reflected wavelets, often times overlapping in complex patterns of constructive and destructive interference.

A typical GPR profile is composed of multiple discrete traces taken at evenly spaced locations along the profile line. Typically, GPR data display systems shade positive anomalies in the trace with black, allowing for better visualization and interpretation (*see* Figure 2.4b). Numerous targets—e.g., stratigraphic layer boundaries, faults, fractures, the groundwater table, contaminant plumes, voids, underground storage tanks, tunnels, etc—can be identified in a GPR profile (e.g. Davis and Annan, 1989; Mellet, 1995; Annan, 2005a; Annan, 2005b). Resolution of the profile, however, is still limited by the center frequency of the GPR antenna used.

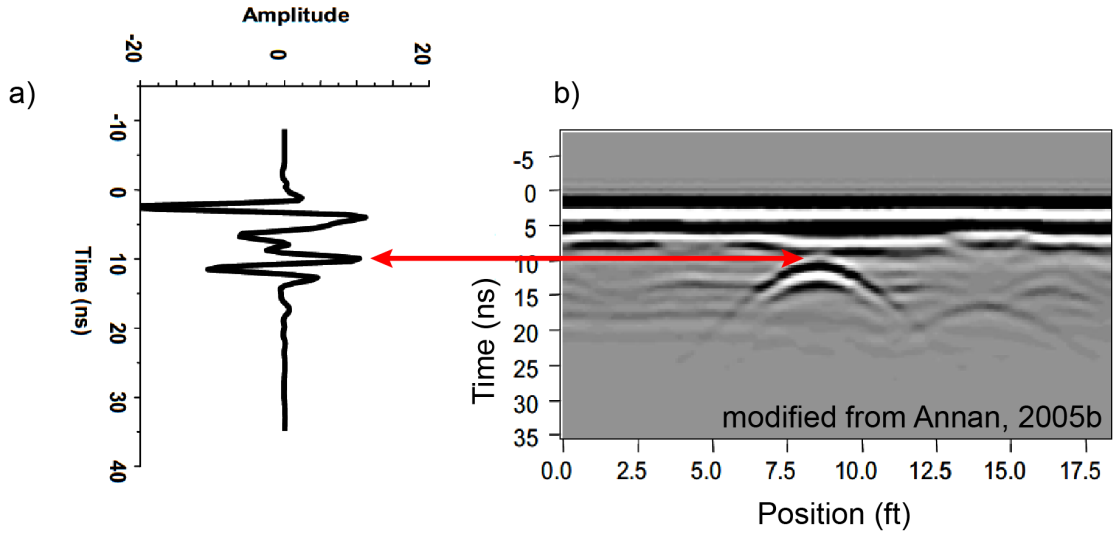

Figure 2.4. Example GPR trace (a) and profile (b) taken over a buried pipe. The pipe can be readily identified by the hyperbolic anomaly indicated by the red arrow and is located at the apex (Annan, 2005b).

For the test presented here, a Sensors & Software Inc., 1000 MHz pulseEKKO PRO GPR system was used. It consists of a transmitting antenna, receiving antenna, power source, odometer, recording DVL, and data display (*see* Figure 2.5). Section 2.2.1 details and rationalizes the GPR system settings, and Section 2.2.2 details the data processing.

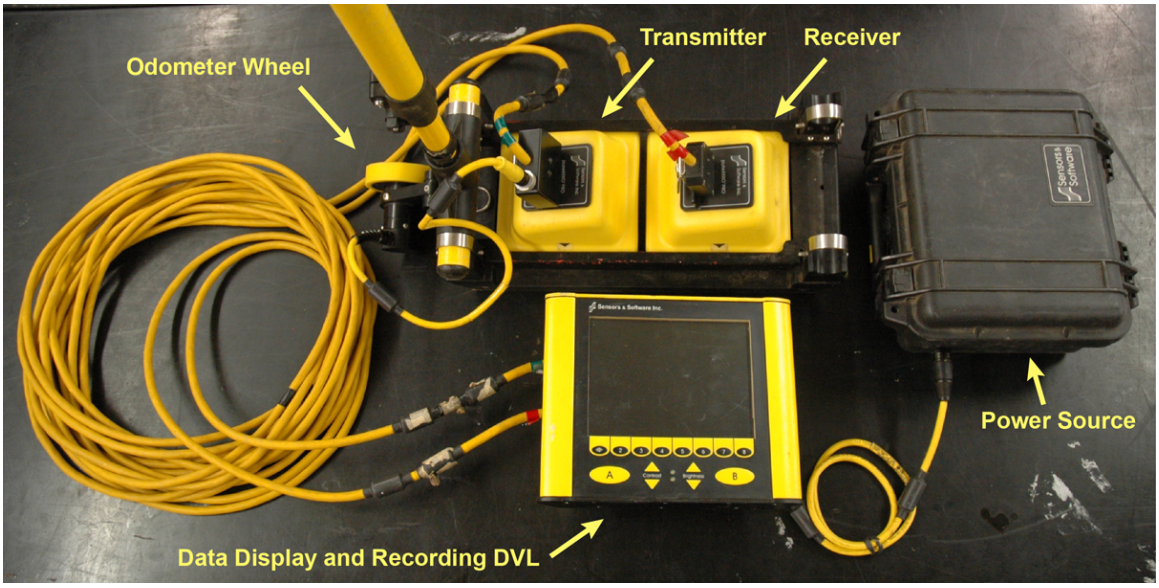

Figure 2.5. Sensors & Software pulseEKKO PRO 1000 MHz GPR system used in this study. All components are labeled above.

Commercially available GPR system frequencies range from 12.5 MHz to 2600+ MHz (e.g., Sensors & Software inc and Geophysical Survey Systems Inc). Because a trade-off exists between resolution and penetration depth, lower frequency systems are typically more useful for field-scale applications, whereas

higher frequency systems are used for construction purposes, e.g. identification of shallow rebar in concrete. The antenna frequency of systems previously used to characterize fractures ranges from 25 MHz to 200 MHz (Grasmueck, 1996; Tsoflias et al., 2004; Porsani et al., 2005; Bradford and Deeds, 2006; Porsani et al., 2006; Tsoflias and Becker, 2008; Becker and Tsoflias, 2010).

The frequency of the antenna dictates the size of the physical analog, where antenna size scales inversely with frequency. The physical analog would need to be proportionally larger for lower frequency antennas to limit edge effects (reflections of the wave off the edges and bottom of the block). Although the 1000 MHz system in this study would, in general, not be used for typical hydrologic applications, use of this antenna frequency allows us to minimize the size of the physical model.

The resolution limit of the GPR system is directly related to the frequency of the antennas: higher frequency equates to higher resolution. Because this study focuses on fractures that are smaller than the resolution limit defined by Widess (1973), choosing a high frequency antenna inherently defines the size of the fractures to be studied. The resolution limit is $\lambda/4$, and the wavelength of a GPR signal is related to the medium (ε_r in Equation 2.1 and List 2.1 presents values for this study) and the frequency of the antenna (f in Equation 2.1).

$$\lambda_i = \frac{c}{f\sqrt{\varepsilon_r}} \quad (2.1)$$

where:

$\lambda_i = wavelength\ (m)$

$f = frequency\ (Hz)$

$c = speed\ of\ light\ (299{,}792{,}458\ m/s)$

$\varepsilon_r = relative\ dielectric\ permittivity, dimensionless$

For the physical fracture analog and the GPR system in this study, the wavelength is 0.3 m. The standard calculation for a resolution limit is therefore 8 mm. By choosing a high-resolution antenna, the fracture aperture must be smaller than 8 mm to accurately evaluate the behavior of the GPR response to sub-resolution limit fractures (*see* Section 3.3 for description of fracture apertures and inserts).

The pulseEKKO PRO antennas generate linearly polarized EM waves. Transmitting antenna orientation with respect to the receiving antenna governs the polarization of the recorded wave. Because interaction with an interface can alter the polarization of the incident wave, GPR antenna orientation governs nature of the reflections and interpretation of the data (Baker et al., 2007). The nature of the subsurface target generally determines the appropriate antenna configuration, but perpendicular broadside/transverse electric (EH/TE) and

parallel end-fire/transverse magnetic (EV/TM) modes are most commonly used (*see* Appendix A for further description). In EH/TE mode—hereafter referred to as EH following Baker et al. (2007)—the incident electric field is polarized perpendicular to the interface. This configuration typically provides a higher signal-to-noise ratio (S/N) and is less susceptible to noise generated by response from features located off the survey line (Baker et al., 2007). As EH mode is generally more preferable for real-world applications, profiles for this study were collected in this mode.

2.2.1 Data Collection

For both fracture aperture and lateral extent tests, a 1000 MHz Sensors & Software pulseEKKO PRO antenna was used with constant separation, step size, sampling interval, and stacking as described in List 2.1. A plastic sled houses the antennas, ensuring constant separation, and an odometer wheel controls the step size by triggering the transmitting antenna (*see* Figure 2.5). The standard recommended settings for all variables shown in List 2.1 were used based on the frequency. The only modification was to the stacking setting (from 16 to 32) to increase both the averaging and S/N.

The GPR profile lines were collected parallel to the edges of the block. For the fracture aperture test, two profiles were collected from the center of one edge to the center of the opposite (*see* Figure 2.6a). The location of these profiles

minimizes out-of-plane edge effects. For the test of lateral variations in fracture aperture, the centerline of the fracture aligns with the centerline of the block in one direction. Three profiles were collected parallel to the fracture and three profiles perpendicular to the fracture (*see* Figure 2.6b), including the centerline profiles taken for the first test.

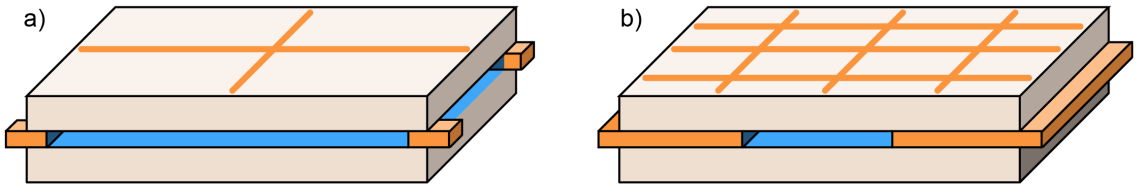

Figure 2.6. a) Profile locations (orange lines) for the fracture aperture test, and b) Profile locations (orange lines) for the lateral extent test.

2.2.2 Post-Processing for Amplitude, Reflection Coefficient, and Phase Extraction

For the initial GPR processing, Sensors & Software's EKKOView Deluxe software was used. The raw data was cropped (*see* Figure 2.7a) to the center 41 traces to remove in-plane edge effects (angled lines in Figure 2.7a) and to the first 10 ns to reduce data file size for further processing. A standard DEWOW filter was applied to remove low frequency noise, and interpolated from a 0.1 ns to a 0.05 ns sampling interval to minimize any processing artifacts (*see* Figure 2.7b). Previous research by Burns (2008) further processed the data within EKKOView Deluxe, but this introduced more errors into the results and did not

allow for statistical evaluation (*see* Appendix C for full discussion); thus, no additional signal processing was used for the data in this study.

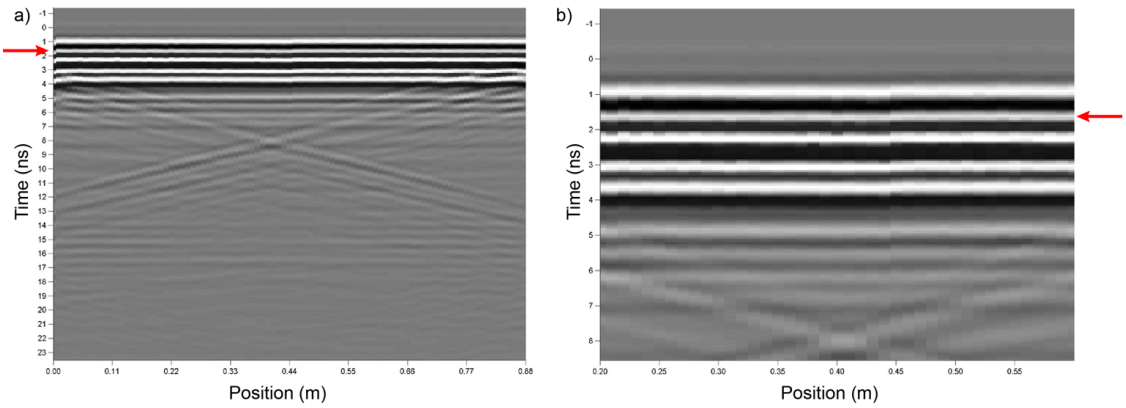

Figure 2.7. a) Profile of a raw dataset over a 1.5 mm fracture aperture (indicated by the red arrow in both a and b). The angled anomalies are edge effects generated from reflections from the vertical sides of the block. b) Processed profile clipped to the center 41 traces to eliminate edges effects and the first 10 ns to reduce file size, filtered for low frequency noise using a DEWOW filter, and interpolated. The slight vertical offset at approximately 0.45 m is inherent of the GPR system and is a main reason for the difference in processing between my research and Burns' (2008) research (*see* Appendix C).

Matlab processing code (*see* Appendix D) was developed to extract the GPR reflection amplitude from the fracture. The code imports a suite of traces from a single profile, extracts the direct wave amplitude for calculation of the reflection coefficient, and the amplitude of the wave reflected from the fracture (*see* Figure 2.8).

Although this research is focused on GPR amplitude response, the amplitude of the wave measured over the physical analog cannot be directly compared to results from the theoretical equations and the numerical modeling. All data were converted into a measure of reflection coefficient using the direct wave (the energy travelling directly from the transmitter to the receiver through the block without reflecting). The path length from transmitting antenna to fracture plane is similar to the separation of the antennas—0.17 m and 0.15 m, respectively. Modeling accomplished for this study using an industry-standard, finite-difference time-domain software, GPRMax 2D (Giannopoulos, 2005) suggests that this difference in path length means that the direct wave overestimates the actual magnitude of the incident wave and therefore this calculation underestimates the reflection coefficient by ~0.1 (~4.5% of the calculated reflection coefficient). The direct wave can also have evanescent reflections, but the similarity of the direct wave shape regardless of

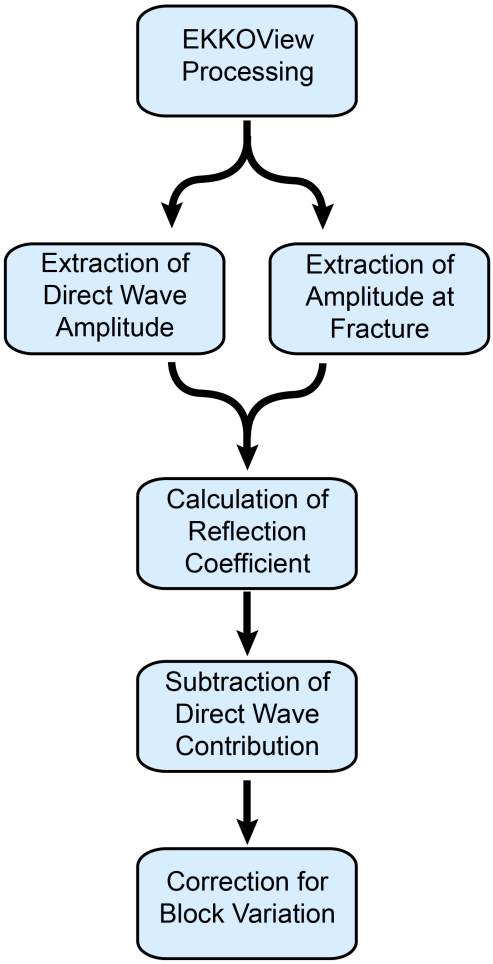

Figure 2.8. Processing flow chart for my Matlab scripts. The 'EkkoView Processing' block incorporates all processing described in Figure 2.7. The text describes the other blocks, and Figure 2.10 explains the correction for the block variation due to temperature.

fracture aperture suggests that the direct wave is fairly consistent and can be used as a proxy for the incident wave. The reflection coefficient is therefore calculated by dividing the amplitude of the wave reflected from the fracture by the amplitude of the direct wave.

Because the blocks are relatively thin, reflection multiples of the direct wave overprint the reflection from the fracture (*see* Figure 2.9). In data collected across a 'zero aperture fracture'—e.g. no fluid between the top and bottom blocks of the physical bedrock fracture analog—the amplitude at the fracture depth is solely due to the direct wave. The contribution of the direct wave reflection multiple was calculated in terms of reflection coefficients by dividing the amplitude at the fracture depth by the zero-aperture direct wave. The contribution of the direct wave from each trace was therefore subtracted to calculate the reflection coefficient of the fracture (*see* Figure 2.8).

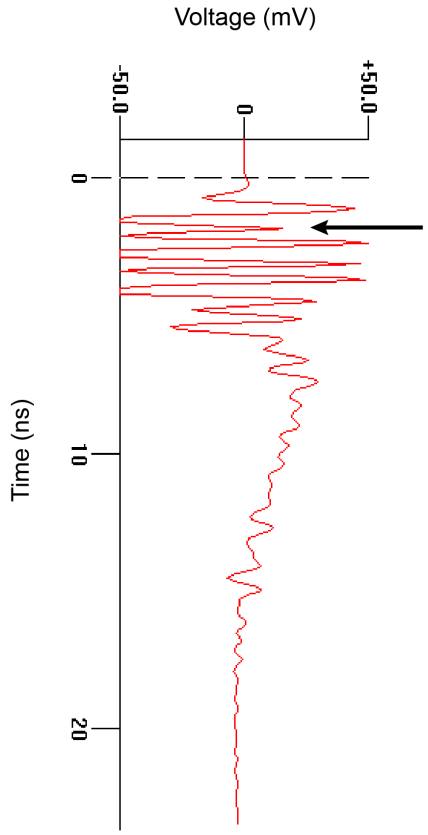

Figure 2.9. Example zero-aperture trace. The black arrow indicates the voltage at the depth of the fracture aperture. The fact that the voltage is not zero is due to a reflection multiple of the direct wave (first positive spike).

Evaluation of preliminary results along with field observations suggested a dependence on temperature, where differential thermal contraction of the block changed the fracture aperture. Because the theoretical equations suggest that reflection amplitude depends strongly on aperture below the resolution limit (Tsoflias et al., 2001), changes in the fracture aperture due to block contraction affect reflection coefficients for fractures smaller than the resolution limit more significantly than for fractures larger than that limit. Correction for temperature dependence, therefore, is not a strictly linear correction. The results are assumed to be independent of fluid conductivity and used to determine the average best-fit relationship for aperture and reflection coefficient for all conductivities (*see* Figure 2.10). Using this relationship, the change in aperture necessary to lower the zero-aperture measurement to a reflection coefficient of 0.0 was determined, and the change in reflection coefficient due to that error in aperture was calculated for the other fracture apertures and was corrected.

Results from the physical analog, theoretical equations, and numerical modeling all suggest, however, that the reflection coefficient is not independent of conductivity. The temperature correction used for this project is a reasonable first approximation, but statistical detrending offers a more sophisticated and alternative correction. Section 2.2.3 presents statistical detrending, and the results are presented in Chapter 3.

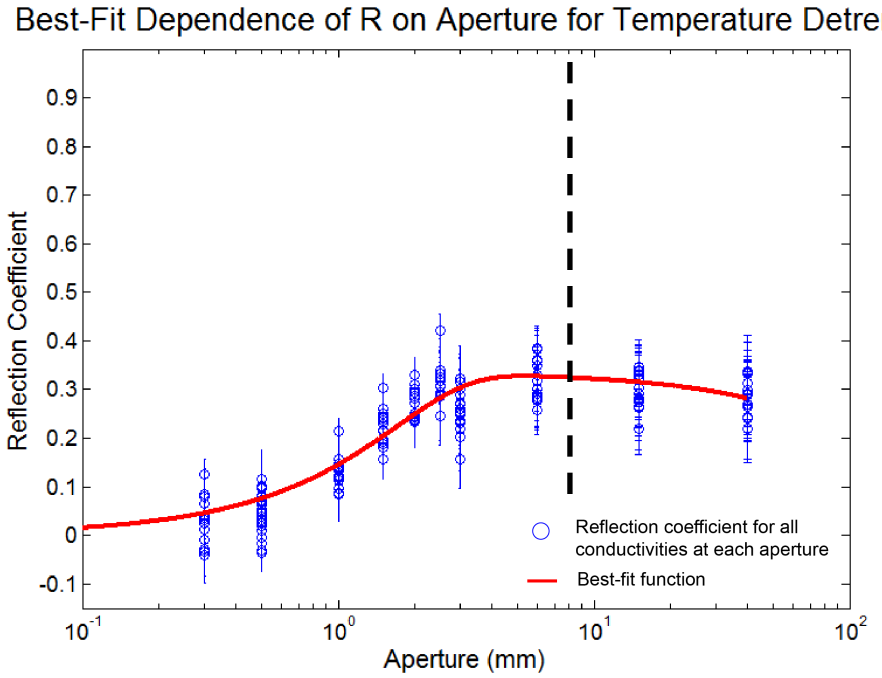

Figure 2.10. Curve fitting for the relationship between aperture and reflection coefficient (red line). This fit assumes no dependence on conductivity, so it is the best fit for the spread of all the data (blue circles) and follows the form $y = c_1 erf(x/c_2) – c_3 x$. The black dashed line indicates the theoretical resolution limit of $\lambda/4$. The break in slope for this best fit line occurs at $\lambda/4\pi$ instead of the theoretical resolution limit as discussed in Sections 2.3.1 and 3.5.

Matlab processing code (*see* Appendix D) was developed to extract the GPR phase from the fracture. The code imports a suite of traces from a single profile, extracts the direct wave phase contribution, and the phase of the wave reflected from the fracture.

The EM signal generated by a GPR system is composed of real and imaginary components. Typically, a GPR system records and plots only the real component of the trace. This is sufficient for extracting the amplitude of the wave but does

not provide any information about the phase of the wave. In order to determine phase variations due to aperture or conductivity variations, an estimate of the imaginary component of the trace is required. The EKKOView Deluxe software uses a Hilbert Transform to calculate the imaginary component over a time window of 1.5 pulse widths (Sensors & Software Inc., 2003).

This transformation converts each trace to a measurement of wrapped phase versus time (*see* Figure 2.11a), that needs to be unwrapped for measurement of the true phase (*see* Figure 2.11b). Wrapped phase is constrained between $-\pi$ and π; phase values that would increase above π are shifted down to start at $-\pi$, hence the saw-tooth appearance of the plot in Figure 2.11a. Almost all phase traces have significant noise in the first second of the trace where the values increase and decrease multiple times over the wrap point of 360°. This confounds both Matlab's built-in unwrapping script and an unwrapping script developed specifically for this study, where continuously increasing or decreasing phase is assumed. Use of either of these scripts results in anomalous extra steps in the phase unwrapping (*see* Figure 2.12). To mitigate this, the traces were clipped to start at a time greater than 0.1 nanoseconds, which provided the most accurate unwrapping with minimal loss in information.

For each aperture/conductivity pair, the phase was measured at the fracture aperture. Because the direct wave response overlays the reflection from the

fracture, the phase contribution from the direct wave was subtracted from the measured phase, as described for reflection coefficient above.

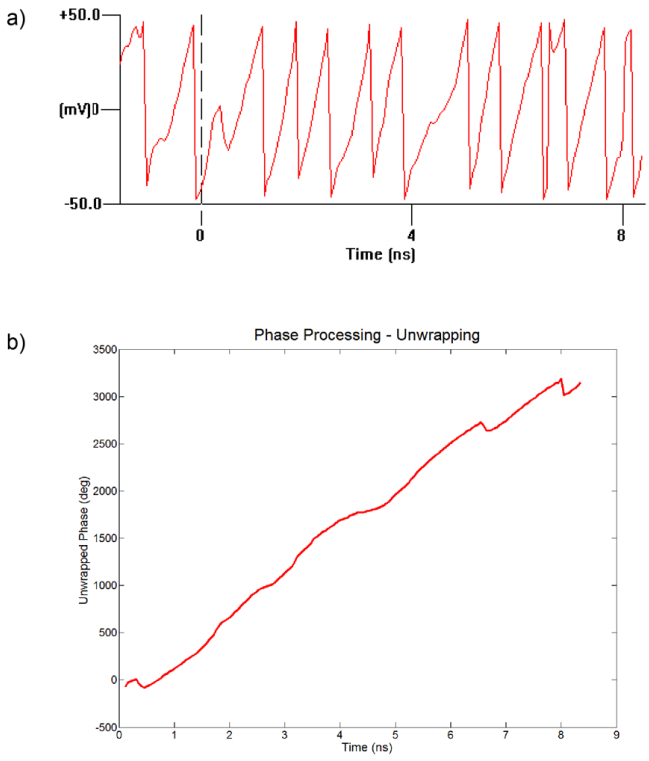

Figure 2.11. a) Wrapped phase calculated using a built-in Hilbert transform in EKKOView Deluxe. b) Unwrapped phase from the same trace.

As with the reflection coefficient, temperature has a significant affect on the shape of the block and the effective aperture of the fracture. The reflection coefficient is composed of a real – the magnitude of the reflected wave – and imaginary – the phase of the reflected wave – component. Because the conductivity factors into the imaginary portion of the reflection coefficient, therefore, phase should depend on conductivity. The simplistic fitting described

above cannot be used to correct the phase for variations in aperture. The fitting does, however, estimate the error in aperture caused by temperature variation. For phase, the results are evaluated versus temperature-corrected aperture.

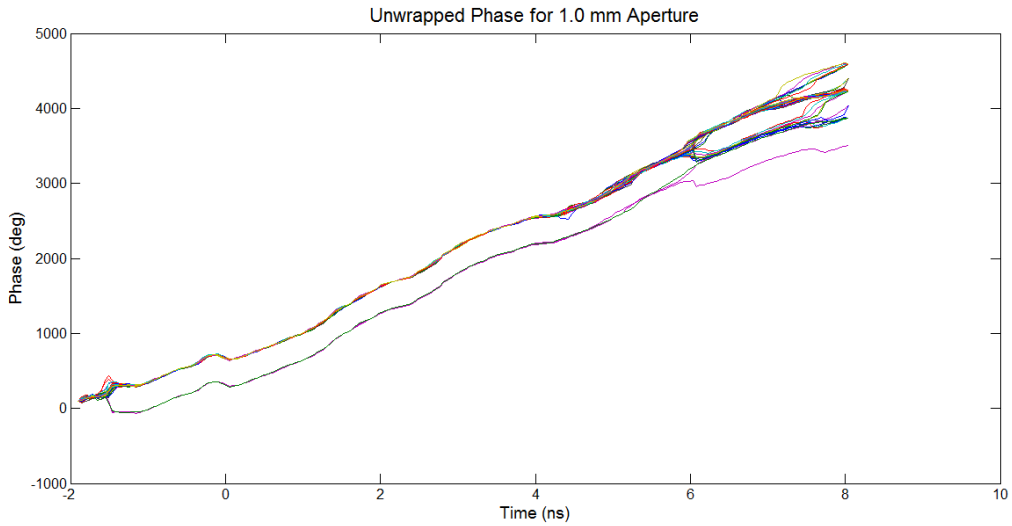

Figure 2.12. Anomalous extra steps in unwrapped phase over the 41 traces for a given aperture/conductivity pair (colored lines). This introduces errors of 360° in the estimated phase. Clipping the trace so that it starts at 0.1 ns mitigates these unwrapping errors.

2.2.3 Statistical Evaluation of Data

The data from the physical analog is composed of 82 traces taken every 0.01 m per fracture aperture per fluid conductivity. The main variables tested in this study are fracture aperture and fluid conductivity, but temperature and position of the trace may also have a significant contribution. Due to the size of the data set and the number of repetitions, the data were analyzed using an analysis of variation (ANOVA) in SAS (SAS Institute Inc, 2011) to test the main variables

(fracture aperture, conductivity, temperature, and position, as described above) for significance as well as the interaction between aperture and conductivity. Any F-value greater than 0.05 is considered significant. Statistical analysis indicated that all variables are significant; therefore, the temperature correction described in Section 2.2.2 is not accurate. The data were evaluated using an Analysis of Covariance (ANCOVA) in SAS to statistically remove the temperature dependence, and the results of both correction methods are compared in Chapter 3.

2.3 Theoretical Equations

Theoretical equations for modeling GPR focus primarily on the behavior of the EM wave at an interface by calculating how much of the wave energy is transmitted and how much is reflected. Simplistic analytical models typically consist of a discretized grid of reflection coefficients (R_{ij} in the equations below) that can be multiplied by a representative wavelet to generate a synthetic GPR profile (Annan, 2005a). In the case of a thin layer or small aperture fracture, the effective reflection coefficient (R_{12} in the equations below) is a combination of reflection and transmission from both the top and bottom interfaces (Widess, 1973; Hollender and Tillard, 1998; Annan, 2005a).

The thin layer equations treat the finite layer as two superimposed, infinite half-spaces, where the Fresnel reflection and transmission coefficients for each interface are determined separately and then combined. Hollender and Tillard (1998) and Annan (2005a) derived equations for the Fresnel reflection coefficient for perpendicular broadside/transverse electric (EH/TE) and parallel end-fire/transverse magnetic (EV/TM) modes. Equations 2.2-2.11 present Annan's equations (2005a) for EH mode only because of the orientation of the GPR antennas used in this study (*see* Appendix E for full set of equations).

Annan (2005a) defined the reflection coefficient with respect to the wave admittance (Y):

$$R_{12} = \frac{Y_1 \cos\theta_i - Y_2 \cos\theta_t}{Y_1 \cos\theta_i + Y_2 \cos\theta_t} \tag{2.2}$$

$$T_{12} = 1 + R_{12} = \frac{2Y_1 \cos\theta_i}{Y_1 \cos\theta_i + Y_2 \cos\theta_t} \tag{2.3}$$

$$Y_i = \frac{1}{Z_i} = \sqrt{\frac{\varepsilon_i + i\frac{\sigma_i}{\omega}}{\mu_i}} \tag{2.4}$$

$$k_1 \sin\theta_i = k_2 \sin\theta_t \tag{2.5}$$

$$\theta_i = \tan^{-1}\left(\frac{0.5S}{D}\right) \quad (2.6)$$

where:

$R_{12} = \ reflection\ coefficient\ of\ the\ layer\ 1\ and\ 2\ interface\ (Equation\ 2.2)$

$T_{12} = \ transmission\ coefficient\ of\ the\ layer\ 1\ and\ 2\ interface\ (Equation\ 2.3)$

$Y_i = wave\ admittance\ (Equation\ 2.4)$

$\theta_i = angle\ of\ incidence$

$\theta_t = angle\ of\ transmission\ (Equation\ 2.6)$

$Z_i = wave\ impedence$

$\varepsilon_i = dielectric\ permittivity\ (F/m)$

$\sigma_i = conductivity\ (S/m)$

$\mu_i = magnetic\ permeability\ (H/m)$

$k_i = wave\ number\ (m^{-1})\ (Equations\ 2.7 - 2.11)$

$S = antenna\ separation\ (m)$

$D = depth\ to\ the\ interface\ (m)$

List 2.1 (Section 2.1.1) summarizes the values of the system-specific parameters for this study. For most geologic materials, including those used in this study, μ_i is equal to the magnetic permeability of free space ($\mu_0, 4\pi\ x\ 10^{-7}\ H/m$), and the wave number ($k_i$) is calculated as follows:

$$k_i = \frac{\omega}{v_i} - i\alpha_i \tag{2.7}$$

$$\omega = 2\pi f \tag{2.8}$$

$$v_i = \frac{c}{\sqrt{\varepsilon_r}} \tag{2.9}$$

$$\alpha_i = \frac{\sigma_i}{2}\sqrt{\frac{\mu_i}{\varepsilon_i}} \tag{2.10}$$

$$\varepsilon_i = \varepsilon_r \varepsilon_0 \tag{2.11}$$

where:

$k_i = wave\ number\ (m^{-1})\ (Equations\ 2.7 - 2.11)$

$\omega = angular\ frequency\ (rad/s)$

$v_i = wave\ velocity\ (m/s)$

$\alpha_i = attenuation\ (Np/m)$

$f = frequency\ (Hz)$

$c = speed\ of\ light\ (299{,}792{,}458\ m/s)$

$\varepsilon_r = relative\ dielectric\ permittivity, dimensionless$

$\sigma_i = conductivity\ (S/m)$

$\mu_i = magnetic\ permeability\ (H/m)$

$\varepsilon = dielectric\ permittivity\ of\ free\ space\ (8.854\ x\ 10^{-12}\ F/m)$

Using these basic definitions, Widess (1973), Hollender and Tillard (1998), and Annan (2005a) derived equations for the reflection from a sub-resolution fracture. The equations produce a measure of the reflection coefficient composed of a real and imaginary part. The modulus of the complex value is the reflection coefficient, and the phase angle is the phase. For this project, a Matlab function was developed (*see* Appendix D) to calculate the reflection coefficient and phase for any frequency electromagnetic wave reflecting off a layer of any material embedded within any homogenous matrix. Coding of the function also allows for simultaneous calculation for a user-defined range of both the thin-layer thickness and conductivity. The basic equations are presented and described in the following sections.

2.3.1 Widess (1973)

Widess (1973) approximated the main peak of the wavelet as a sine wave and derived the reflection coefficient based on the time delay between the reflection from the top and bottom interfaces. For this experiment, R_{12} is calculated as the reflection coefficient from UHMW-PE to the water filling the fracture.

$$R_{max} = R_{12}\left(\frac{2}{1 + R_{12}^2}\right) \tag{2.12}$$

$$R_t = \frac{4\pi d_2}{\lambda_2} R_{max} \tag{2.13}$$

where:

$R_{max} = theoretical\ reflection\ coefficient\ from\ a\ thick\ layer, dimensionless$

$R_{12} = reflection\ coefficient\ from\ layer\ 1\ to\ layer\ 2, dimensionless$

$R_t = reflection\ coefficient\ \ for\ the\ thin\ layer, dimensionless$

$d_2 = layer\ thickness\ (m)$

$\lambda_2 = wavelength\ of\ the\ thin\ layer\ (m)$

This equation takes the form of the theoretical reflection coefficient from a very thick bed (R_{max}) multiplied by a scaling factor related by the thickness of the bed. This equation applies to layers that are thinner than the resolution limit of λ/4. In the limit of a very thick bed, R_t should approach R_{max}, so $4\pi d_2/\lambda_2$ should approach 1 in the limit of large d_2. The scaling factor, however, continues to increase with increasing thickness of the bed and does not reach a limit. For the application of this equation, if the calculated scaling factor is greater than 1 for a given bed thickness, R_t is set equal to R_{max}. This modification to the equation accounts for the continuous increase in the scaling factor.

Given the nature of the equation, however, the modification does have the inherent assumption that all layers thicker than λ/4π, as opposed to λ/4, can be approximated with a reflection coefficient equal to that of a very thick bed (R_{max}).

Section 3.5 contains an in-depth discussion of this assumption as applied to results from the physical fracture analog.

2.3.2 Hollender and Tillard (1998)

Hollender and Tillard (1998) introduced a measurement of effective dielectric permittivity that can be used to write all governing equations for electromagnetic wave propagation. Because the effective dielectric permittivity depends on frequency, they derived three frequency-independent parameters—Jonscher parameters—for a range of geologic materials from multi-frequency laboratory measurements of effective dielectric permittivity.

The materials in this study have not been characterized in Jonscher parameters, so the wave number was calculated using standard variables and Equation 2.7. Hollender and Tillard's (1998) formulation of the reflection coefficient of the thin-bed does not require Jonscher parameters, so the Fresnel reflection and transmission coefficients are calculated using Annan's (2005a) equations (*see* Equation 2.2 and 2.3).

$$R_t = R_{12} + T_{12}T_{21}\sum_{n=1}^{\infty} R_{12}^{(2n-1)} e^{-in2d_2k_2\cos\theta_t} \tag{2.14}$$

where:

$R_{21} = reflection\ coefficient\ from\ layer\ 2\ to\ layer\ 1, dimensionless$

$T_{12} = transmission\ coefficient\ from\ layer\ 1\ to\ layer\ 2, dimensionless$

$T_{21} = transmission\ coefficient\ from\ layer\ 2\ to\ layer\ 1, dimensionless$

$k_2 = wave\ number\ for\ layer\ 2\ (m^{-1})$

2.3.3 Annan (2005a)

The Annan (2005a) equation (*see* Equations 2.15-2.16) calculates the reflection coefficient of a thin layer as a combination of the reflection from the top interface and a sum of the reverberations within the layer. The original formulation uses a measurement of the thickness of the layer (d_2) that assumes normal incidence regardless of the incidence and transmission angles used to calculate the reflection and transmission coefficients. The equation is modified to include the actual path length within the layer ($d_2/\cos\theta_t$).

$$R_t = R_{12} + \frac{T_{12}T_{21}R_{21}\Delta}{1 - {R_{21}}^2\Delta} \tag{2.15}$$

$$\Delta = e^{i2k_2d_2/\cos\theta_t} \tag{2.16}$$

For this system, the contrast between the wave number of the UHMW-PE block and the water is such that the transmission angle (calculated using Equation 2.6) is close to vertical. Even though factoring in the difference in path length does not

greatly affect the results because the transmission angle is small, all of the results presented here do include the path length correction. Because the transmission angle is dependent on the material filling the layer or fracture, the developed Matlab function does factor in the difference in path length, allowing for a wider range of applications.

2.4 Numerical Model

The programs GPRMax2D and GPRMax3D are finite-difference time-domain numerical modeling software for GPR trace simulation (Giannopoulos, 2005). The user generates a discretized 2D or 3D model composed of finite areas (cells or elements – the term 'cell' is used here to match the GPRMax2D nomenclature) or volumes of constant dielectric permittivity, conductivity, and magnetic susceptibility and defines a source and receiver of electromagnetic waves to include frequency, wave shape, position, and step size. The GPRMax software numerically propagates the electromagnetic wave generated by the source and evaluates Maxwell's equations (e.g., Griffiths, 1999) at each cell within the model.

Because it is dealing with smaller models and simpler equations, GPRMax2D is more computationally effective and is therefore preferable if the underlying assumptions are acceptable for the model. By only defining a 2D model, the user

assumes that the model has infinite extent in the third dimension. For some applications, this is not a reasonable assumption. For both fracture aperture and lateral extent tests in this study, the block is much larger than the footprint of the GPR in the direction perpendicular to the survey and the fracture is constant in that direction. Infinite extent is, therefore, a reasonable assumption, and simulations were conducted in GPRMax2D.

One drawback to using GPRMax2D as opposed to 3D is that the simulation of the source is limited. Although an infinitesimal dipole is a more accurate representation of the GPR antennas (G. Johnston, personal communication), GPRMax2D can only simulate a linear dipole source. The discretization necessary in the vertical direction to model a sub-millimeter fracture aperture results in a computation time for a GPRMax3D model of approximately 2 hours per trace. Between both tests, this study required modeling of over 3400 traces, or roughly 40 weeks of straight computer time on the Dell Inspiron N4110 with four 2.3 Gb IntelCore processors used in this research. Despite the drawback to the simulation of the source, therefore, all traces were modeled in GPRMax2D. Sections 3.4, 3.5, 4.4, and 4.5 further cover the results from GPRMax2D.

2.4.1 GPRMax2D

Figure 2.13 shows a cross-section through the GPRMax2D model. The model domain is 1.6m wide by 2m thick. Each color in Figure 2.13 defines a separate

material within the GPRMax2D model domain. The physical model contains four main materials—free space, UHMW-PE, fluid, and soil—with set values for μ_r, ε_r, and σ (*see* List 2.1). Both the conductivity of the fluid layer and the thickness of the fluid layer were varied to match the values tested with the physical model.

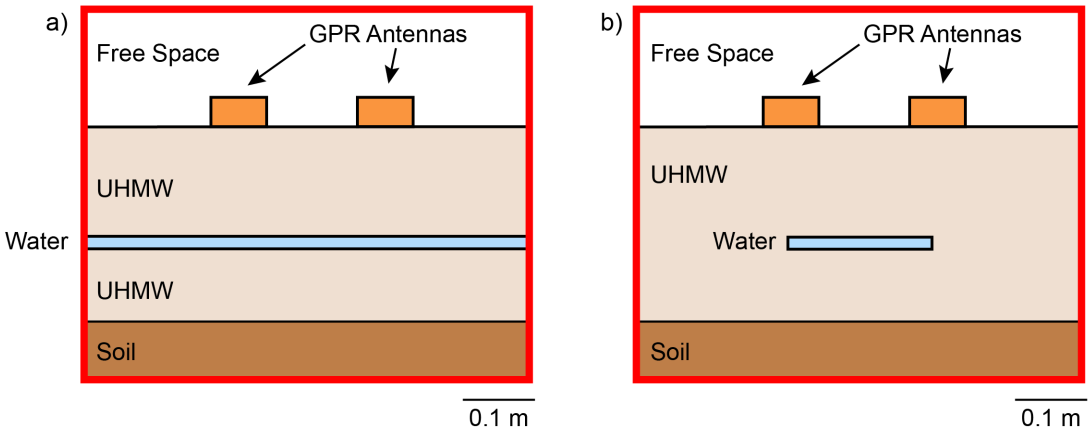

Figure 2.13. GPRMax2D model diagrams for the fracture aperture (a) and lateral extent (b) tests. For the lateral extent tests, the simulated antennas collected 100 traces across the model space.

This GPRMax2D model is slightly larger than the physical model to account for the cells needed to implement the absorbing boundary conditions (ABCs) employed by GPRMax2D (denoted by the red lines in Figure 2.13). At these cells, the propagating wave is fully absorbed, which simulates the wave continuing to infinity without encountering any interfaces. Because the behavior of the wave in these cells is not governed by either standard wave propagation equations or the defined characteristics of the material, the simulated antennas are placed at least 15 cells – where each cell is 0.0025 m by 0.0001 m and so

has an aspect ration of 2.5:1 - away from the boundary. This adds an extra band around the model equivalent to 15Δ, where Δ is the size of the discretization in that dimension - 0.0025 m in the x-direction and 0.0001 m in the y-direction.

Finite-difference time-domain models divide the given domain into discrete cells with prescribed length and height. The horizontal discretization (Δx) was selected using the equation for the recommended value provided by Giannopoulos (2005; *see* Appendix F); the vertical discretization (Δy), however, must be smaller to accurately model the sub-millimeter fracture apertures. The Δy was selected at one third the size of the smallest aperture tested (*see* Appendix F). This ensured that the fracture was represented by a minimum of three cells in the model. Smaller discretization values for Δy increased the computation time, but did not significantly affect the resulting modeled trace. This was evaluated by examining the difference in amplitude between the results of models with different vertical discretization values. The amplitude variation is less than 0.05% of the reflection coefficient (0.40 versus 0.3908).

The GPRMax2D trace does not require any standard GPR processing such as trace deletion, DEWOW filtering, or interpolation, because no noise is inherently applied to modeled waveform. For evaluating the amplitude response, data were directly imported into Matlab, and extracted the amplitude and calculated reflection coefficient were determined using the same process as with the

physical analog data (*see* Section 2.2.2 and Matlab scripts available in Appendix D). For determining the phase, Sensors & Software developed conversion software to upload GPRMax2D output files into EKKOView Deluxe, and the processing to extract the phase at the fracture aperture follows Section 2.2.2.

CHAPTER 3: FRACTURE APERTURE

3.1 Abstract

Accurate characterization of subsurface fractures is indispensible for contaminant transport and fresh water resource modeling because discharge is cubically related to the fracture aperture; thus, minor errors in aperture estimates may yield major errors in a modeled hydrologic response. Ground penetrating radar (GPR) has been successfully used to noninvasively estimate fracture aperture for sub-horizontal fractures at the outcrop scale, but limits on vertical resolution are a concern. Additionally, theoretical formulations and field tests have demonstrated increased GPR amplitude response with the addition of a saline tracer in a sub-millimeter fracture. However, robust verification of existing theoretical equations without an accurate measure of aperture variation across a fracture surface is difficult. This work is directed at better verification of theoretical predictions of GPR response. The response of a 1000 MHz PulseEKKO Pro transducer to a fluid-filled bedrock fracture analog composed of two plastic (UHMW-PE) blocks was measured, where fracture aperture ranged from 0-40 ± 0.3 mm and fluid conductivity from 0-5700 ± 5 mS/m. The GPR profiles were acquired down the centerline of the block, horizontally stacked to reduce errors, normalized to the control response at zero aperture, and used to calculate reflection coefficient by dividing by the magnitude of the direct wave and the instantaneous phase using a Hilbert transform. Comparison of the measured GPR response to previously formulated theoretical equations and numerical modeling suggests that numerical modeling best predicts both amplitude and phase response variations for

changes in fracture aperture and conductivity. The Widess equation combined with an empirically derived scaling factor also predicts GPR amplitude response but not phase. Future applications to inversions of field data to map subsurface fracture networks will rely on easily invertible models, and numerical modeling using GPRMax2D can help develop a theoretical model for computationally effective and accurate inversion.

3.2 Introduction

Accurate modeling of contaminant transport in the subsurface relies on characterization of fracture networks. Discharge through a fracture system is related to the cube of the fracture aperture (Lamb, 1932; Snow, 1969) so even small fractures can have a significant impact on groundwater flow. Although ground penetrating radar (GPR) systems can characterize fractures, they are limited by inherent resolution limits below which the fracture cannot be identified by standard GPR interpretation techniques.

Evaluation of the behavior of the reflected wavelets from a sub-resolution fracture suggests that the amplitude and phase of the wave changes in a predictable manner related to fracture aperture, fracture fill type, and conductivity (*see* Chapters 1 and 2 for further discussion). Widess (1973), Hollender and Tillard (1998), and Annan (2005a) derived theoretical equations describing the behavior

of the wavelet, and previous research used these theoretical equations as the basis for inversion of field data to determine fracture aperture (Deparis and Garambois, 2009; Sassen and Everett, 2009). Use of these equations allows for characterization of sub-resolution fractures and will help to improve modeling of contaminant transport, but it begs the question as to whether these equations accurately predict the behavior of the amplitude of the reflected GPR wave with respect to fracture aperture, fluid type, and fluid conductivity.

The first part of the experiment considers the simplest case: a horizontal fracture with constant aperture and infinite extent (*see* Chapter 3). Data were collected over a physical bedrock fracture analog (*see* Figures 1.3a and 2.1) for fracture apertures of 0-40 ± 0.3 mm and conductivities of 0-5700 ± 10 mS/m, then the amplitude and phase of the wave reflected from the fracture was extracted, and the reflection coefficient was calculated (*see* Sections 2.1 and 2.2 for a full description of the process). The previously derived theoretical equations and numerical modeling produce predictions of reflection coefficient and phase, and the results were compared among the three techniques to determine the applicability of either the theoretical equations or numerical modeling to inverting real-world data.

3.3 Methodology

For this portion of the study, the physical analog configuration includes two blocks of ultra-high molecular weight polyethylene (UHMW-PE) stacked on top of each other and separated by inserts at the four corners, forming the constant-aperture fracture analog. The fracture is completely saturated by immersing the blocks in a stock tank, and GPR data were collected along two orthogonal lines through the center of the block and parallel to the sides for a discrete set of fracture apertures and fluid conductivities (*see* Chapter 2 for a full discussion of the physical analog and the procedure for varying aperture and fluid conductivity).

3.3.1 Physical Analog

Overhead transparency inserts between each corner of the top and bottom block act as spacers to form the fracture. The inserts are squares cut from standard overhead transparency sheets made from cellulose acetate and stacked together. Each insert is 0.098 ± 0.001 mm thick (Burns, 2008). Error introduced by variations in thickness of the inserts is minimal compared to variations in thickness of the block (J. Batchik, personal communication); thus, the inserts are considered to be 0.1 mm thick which is reasonable, given the accuracy of the rest of the physical analog. For the largest aperture, 40.0 mm, the stack of inserts was not stable due to low friction between the inserts. Therefore, a 25.0 ± 0.5

mm block of UHMW-PE was used in conjunction with a 15.0 ± 0.015 mm stack of overhead transparency inserts. To minimize variation between the data sets, I used the same sets of inserts and blocks of UHMW-PE for every aperture test.

Previous evaluation of the theoretical equations suggested a steep relationship between reflection coefficient and aperture below the theoretical resolution limit (Tsoflias et al., 2001; Burns, 2008). Behavior above the theoretical resolution limit (8 mm for this system) is well established, and should be comparable to the Fresnel reflection from a single interface—e.g., UHMW-PE into water. Nine apertures were selected below the resolution limit that span the steep increase from 0.0 mm to 8.0 mm, and two above the resolution limit (*see* List 3.1).

List 3.1. Apertures and conductivities measured in the fracture aperture test. Green highlighted cells are fracture apertures smaller than the resolution limit and red highlighted cells are larger.

Fracture aperture (mm)

0.0	0.3	0.5	1.0	1.5	2.0	2.5	3.0	6.0	15.0	40.0

Fluid Conductivity (mS/m)

0.0	2.0	5.0	7.0	10.0	15.0	20.0	25.0	35.0
45.0	55.0	75.0	100.0	150.0	200.0	300.0	400.0	500.0
800.0	1100.0	2000.0	2900.0	4000.0	4800.0	5700.0		

As the thickness of the block has a variance of ± 0.3 mm, the 0.3 and 0.5 mm fractures in this study may seem to be beyond the accuracy of the system and, therefore, not worthwhile. Field research by Talley et al. (2005), Tsoflias and Becker (2008), and Becker and Tsoflias (2010), however, demonstrated increased response to a high conductivity tracer in a 0.5 mm bedrock fracture in quartzose sandstone at the Altona Flatrock site near Plattsburgh, New York. A single study by Burns (2008) evaluated the response to a 0.5 mm fracture saturated with high conductivity fluid (500-5700 mS/m) in an effort to compare to the results published by Talley et al. (2005), Tsoflias and Becker (2008), and Becker and Tsoflias (2010). Although his results seemed to suggest a complex relationship between fluid conductivity and GPR response, variability in the GPR traces indicated that this was likely due to air bubbles in the fracture. Therefore, the 0.3 and 0.5 mm fractures were included to compare to Burns' previous results and to evaluate the accuracy of the physical analog—i.e., to determine the smallest fracture that would yield data that would still produce useful information.

Conductivities ranged from 0 mS/m (distilled water) to 5700 mS/m (seawater; *see* List 3.1). Approximately equal numbers of conductivities were selected in each order of magnitude to allow for coverage of GPR behavior over a wide range of conductivities. Because conductivities on the order of 10's or 100's of mS/m are more likely in a real-world system, more data steps were measured in those

conductivities. Selected higher values are equal to conductivities previously tested by Burns (2008) to allow for comparison (*see* Appendix C for discussion).

Some errors are inherently introduced in the physical analog data, namely air bubbles and temperature variations of the block. Although a number of steps in the data collection process were designed to minimize air bubbles in the fracture (*see* Section 2.1), the removal of all air bubbles could not be guaranteed. Research by Burns (2008) suggested that air bubbles in the fracture would affect the shape of the GPR trace; however, there was no similar evidence of variation in the traces that would indicate systematic air bubbles.

The largest, systematic error in the fracture aperture was caused by ambient temperature variations causing unequal thermal expansion or contraction of the block. This was especially noticeable while gathering data in the late fall of 2012 where temperatures overnight were drastically lower than during the day. Even though the top block was flat during the previous day, the outer edge would contract overnight to form a 0.5-1.0 mm (0.5-1% of the size of the block) gap around the edges. The block was allowed to equilibrate with the ambient temperature, i.e., flatten out, before collecting data. However, temperature clearly had a strong control on the data, and temperature variations are statistically significant to variations in the data. This is likely due to changes in shape of the block. Although conductivity also varies with temperature, the conductivity was

measured for each data set, so that variation is accounted for in the data. Processing of the data removes a portion of the contribution due to temperature, but the error is still present in the data.

3.3.2 Analytical Models

Because the analytical models are computationally efficient, models were run over a spectrum between the minimum and maximum aperture and conductivity (*see* List 3.1). From this matrix of results, the discrete fracture apertures and conductivities were selected to allow for direct comparison to field results.

3.3.3 Numerical Model

By moving the GPR across the surface of the physical analog, between 89 and 100 traces were collected per fracture aperture for each conductivity step. This allowed for averaging and minimization of inherent system noise. The GPRMax2D model does not include noise or random surface variation, so simulating traces at different horizontal locations in the model does not provide any additional information. The GPR response was modeled on the center point of the numeric model to generate a single trace for each aperture and conductivity, using the exact conductivity values measured in the field (*see* List 3.1). The set-up of the numerical model and the process of generating a single trace at the center of the model do not account for the edge effects seen in the

physical analog results. Because the physical analog results are cropped to eliminate edge effects, simulating a single trace does not bias the results.

3.4 Results

Sections 3.4.1 - 3.4.3 detail the results for each technique and present 3D surface plots of fracture aperture, fluid conductivity, and reflection coefficient as well as 2D plots at the discrete aperture values measured using the physical analog. Phase is shown as 2D plots of phase and aperture at discrete conductivities. The black dashed line indicates the resolution limit of 8 mm for this system.

3.4.1 Physical Analog

Figure 3.1 shows the results for the reflection coefficient calculated from data gathered over the physical bedrock fracture analog versus fracture aperture and fluid conductivity (*see* Figure 3.1a) and fluid conductivity only (*see* Figure 3.1b). Each mesh point in Figure 3.1a represents an average measurement of reflection coefficient for a discrete aperture/conductivity pair. The reflection coefficient increases steeply from null at 0.0 ± 0.3 mm aperture to a maximum reflection coefficient of 0.45 ± 0.05 at 2.5 ± 0.3 mm aperture and 5700 ± 10 mS/m. Beyond the theoretical resolution limit, the reflection coefficient plateaus to approximately

0.3. The reflection coefficient then declines by 0.05 between the 2.5 mm to 3.0 mm aperture results.

Error bars in Figure 3.1b show the standard deviation of calculated reflection coefficient for each aperture/conductivity pair and are on average 0.05. Reflection coefficients for apertures between 0.5 ± 0.3 mm and 2.5 ± 0.3 mm do not to overlap even when error bars are taken into account.

Reflection coefficient varies strongly with fluid conductivity at high conductivities (*see* Figure 3.1b). This break in slope occurs between 2000 mS/m and 4000 mS/m (*see* Figure 3.1b), and the reflection coefficients increase by approximately 0.1 for fracture apertures between 0.0 ± 0.3 mm and 2.5 ± 0.3 mm.

Statistical analyses of the results indicate that all main contributing factors—aperture, conductivity, position along the profile, and temperature—are significant (*see* Table 3.1). That aperture and conductivity are significant is expected, but given that the block is homogenous and isotropic and thickness variations should be random, the position should be a random factor. The F-value in Table 3.1 indicates that position is less significant than the others, but that it is still a contributing factor. Figure 3.2 plots deviation from the mean reflection coefficient versus position across the block for representative fracture apertures and

conductivities. Position does not have an obvious trend, but still is significant according to the ANOVA results.

The ANCOVA (*see* Section 2.2.3) corrects statistically for the dependence of the reflection coefficient on temperature. The results of the ANCOVA (*see* Figure 3.3) are similar to the results corrected for temperature using a best-fit detrend (*see* Section 2.2.2 and Figure 3.1). The results deviate between the two corrections for small apertures, 0.0 mm and 0.5 mm.

Table 3.1. Results of the ANOVA for data that has been corrected for temperature variation using the process described in Section 2.2.2. Aperture has the most significant control on the reflection coefficient, followed by conductivity. Temperature has a smaller but still significant contribution as does position on the block (see Figure 3.2 and Section 2.2.2).

Source	Degrees of Freedom	Type I SS	Mean	F Value	Pr > F
Model	328	397.28	1.21	485.69	< 0.001
Aperture	10	361.97	36.19	14514.5	< 0.001
Conductivity	24	10.23	0.43	170.99	< 0.001
Ap*Cond	212	24.56	0.12	46.45	< 0.001
Position	81	0.47	0.01	2.33	< 0.001
Temperature	1	0.056	0.06	22.63	< 0.001

Figure 3.4 shows the phase results for 10 apertures and 18 conductivities. Behavior of the phase is fairly independent of conductivity but increases sharply over 0.0-3.0 mm aperture for all conductivities. At conductivities of 73-5702 mS/m, the phase is constant for 6.0– 40.0 mm apertures. At low conductivities, 5-50 mS/m, and large apertures, the phase data are more scattered, but still follow a similar trend for the majority of data points.

3.4.2 Theoretical Equations

Figure 3.5 shows 3D (left) and 2D (right) plots of the results using the Widess (a), Hollender and Tillard (b), and Annan (c) theoretical equations. All three predict a steep increase in reflection coefficient of 0.0 for a 0.0 mm aperture to a maximum of 0.95 for a 5.0 mm aperture at medium conductivities. Hollender & Tillard as well as Annan both predict complex behavior at larger apertures and high conductivities: decreased reflection around resonance apertures and dips in reflection at higher conductivities. Figure 3.5b and c show the behavior of discrete fracture apertures over a range of conductivities, and indicate that the 15.0 mm fracture aperture should have a lower reflection coefficient than either the 6.0 mm or 40.0 mm fracture by approximately 0.2. The Widess equation predicts a steep increase and flat response for fractures larger than $\lambda/4\pi$ (*see* Section 2.3.1 for a description as to why this occurs) as well as a slight increase in reflection coefficient at large fracture apertures and high fluid conductivities.

Figure 3.6 shows the phase results using the Widess (a), Hollender and Tillard (b), and Annan (c) equations. Calculated phase using the Widess (1973) equation is 0° for all conductivities and all apertures (*see* Figure 3.6a). The only deviation from this relationship occurs at high conductivities, where the phase increases by ~1°. The phase results using the Hollender and Tillard (1998) and Annan (2005a) equations show similar response. For conductivities less than 500.5 mS/m, the Hollender and Tillard calculated phase decreases from 100° and wraps at each 0° crossing, and the Annan calculated phase increases from 275° and wraps at each 360° crossing, with slight deviations at the wrap points. The phase wrap occurs at approximately the same apertures as the null reflection coefficient points observed in Figure 3.5a. At conductivities greater than 1102 mS/m, the phase decreases from 100° to 0° (b) or increases from 275° to 360° (c) with little to no wrapping.

3.4.3 Numerical Model

Figure 3.7 shows 3D and 2D plots of the results from GPRMax 2D numerical modeling. Numerical modeling suggests a steep increase in reflection coefficient from 0.0 for a 0.0 mm fracture aperture to 0.45 for a 2.67 mm ($\lambda/4\pi$) fracture aperture. Behavior for fracture apertures larger than the theoretical resolution limit is relatively constant for a given conductivity but does increase at high fluid conductivities. The increase is shallower than that observed in the physical

analog data. The reflection coefficient increases by approximately 0.1, but this break in slope occurs between 300-400 mS/m.

Figure 3.8 shows the phase results from GPRMax2D numerical modeling. At small apertures, less than 3.0 mm, and all conductivities, the phase decreases and increases by ~100°. The phase is relatively constant at large fracture apertures and conductivities lower than 1000 mS/m but decreases for the 40.0 mm aperture at conductivities higher than 1000 mS/m.

3.5 Discussion

Results suggest that, of the techniques examined here, numerical modeling is the most robust technique for predicting the reflection coefficient magnitudes that were measured using the physical analog. The shape of the aperture-conductivity-reflection coefficient surface from numerical modeling most closely matches the shape measured over the physical analog. Two of the three theoretical equations produce nodes of zero or decreased reflection that should be measurable in the 15.0 mm aperture data, but do not occur in either the physical analog or numerical modeling results.

The magnitude of the reflection coefficient predicted by the numerical modeling, however, is higher than the magnitude calculated from the physical analog data

by 0.1 on average (~4.5% of the calculated reflection coefficient). The numerical modeling does not overestimate the reflection coefficient as much as the theoretical equations but still does not exactly predict the magnitude. Furthermore, the dependence on conductivity predicted by the numerical modeling is a simple increase in reflection coefficient at high conductivities. The physical analog results do not suggest a complex dependence on conductivity as predicted by either the Hollender and Tillard (1998) or Annan (2005a) equations, and although the initial increase in reflection coefficient occurs at a higher conductivity in the physical model, the overall behavior is more closely replicated by the numerical modeling.

Either variation in the physical analog or the inherent nature of the numerical modeling can account for these discrepancies. Variations in the physical analog fracture aperture may cause averaging errors (in spite of attempts to the contrary) that result in a consistently smaller fracture aperture than set with the inserts, which would result in smaller measured reflection coefficients due to the smaller aperture. While this explains the dependence on fracture aperture, it does not explain the difference in the dependence on conductivity. Alternatively, representing the antennas as simple line sources may introduce errors. Warren and Giannopoulos (2011) demonstrated improved GPRMax model results by incorporating internal antenna electronics and materials. More robust modeling of the antennas is needed to determine whether the difference in reflection

magnitude and behavior is due to the simplicity of my modeling or to an actual deficit in how well the numerical modeling predicts real-world data.

The Hollender and Tillard and Annan equations both predict low-reflection coefficient nodes at discrete apertures that are not measured over the physical analog or predicted by the numerical modeling or Widess equation. These are related to destructive interference between the reflections from the top and bottom interface. The Hollender and Tillard and Annan equations are both derived from the Fresnel reflection coefficients, as opposed to a sine wavelet as used for the Widess. The results suggest that the GPR response is not well modeled using the Fresnel reflection coefficients as a basis for derivation.

Out of the three theoretical equations, the Widess model best predicts the behavior of the reflection coefficient, although it also overestimates the magnitude. The reflection coefficient increases slightly at high conductivities, as seen in the physical analog results, and there are no low-reflection nodes at larger apertures. The lack of low-reflection nodes is slightly artificial (*see* Section 2.3.1 for a full description), because the equation assumes that the fracture behaves as a very thick layer for all apertures greater than $\lambda/4\pi$. This is much smaller than the resolution limit derived by Widess (1973) but supports the behavior of all of the physical analog data, theoretical equations, and numerical

modeling. In all three cases the reflection coefficient reaches an asymptote between 2.0 and 4.0 mm.

For this system, results indicate that fractures larger than $\lambda/4\pi$ can be approximated as thick layers. This complicates potential inversion applications because fractures with apertures such that $\lambda/4\pi < d < \lambda/4$ will not be identifiable using standard GPR interpretation techniques but will also not have a unique reflection coefficient that would allow them to be characterized using the amplitude of the reflected wave (*see* Figure 3.1b, Figure 3.6a, and Figure 3.8b, where the reflection coefficients of all fractures larger than 3.0 mm plot on top of each other). This effectively gives the technique a “blind spot” of approximately 4.0-6.0 mm where a fracture could be identified in the amplitude variation but could not be accurately characterized. Results from the physical analog, however, suggest a more complex behavior of the reflection coefficient at those fracture apertures than what either the Widess (1973) equation or the numerical modeling results indicate. More work is needed to characterize this behavior and modify either the numerical modeling or the Widess equation for possible inversion applications.

As with the results for GPR reflection amplitude response discussed above, the phase results from the numerical modeling most closely match the results from the physical analog model. Although the behavior predicted by the numerical

modeling at large fracture apertures and high conductivities does not match the results from the physical analog, the overall behavior at the majority of apertures and conductivities is similar between the physical analog and the numerical modeling. Furthermore, the decrease and increase in phase predicted by the numerical modeling over fracture apertures less than 3.0 mm may explain the scatter in the measured phase at small apertures (*see* Figure 3.4). Small errors in the actual aperture of the physical analog could result in large errors in measured phase if the numerical modeling is accurate. The Annan equation, however, predicts the overall behavior of the phase at small fracture apertures and low conductivities – increasing phase with increasing aperture – but does not predict the magnitude of the phase. The Hollender and Tillard (1998) equation predicts deceasing phase with increasing fracture aperture, and the Widess (1973) equation predicts no phase change. Both the Annan and Hollender and Tillard equations predict little to no phase response at high conductivities that is not seen in the results from the physical analog.

Although the numerical model does a better job predicting the response, determination of fracture aperture from field data by inverting a numerical model would require a library of results from various fracture apertures, depth, fluid type, fluid conductivity, etc. The Widess equation is easier to invert but overestimates the reflection coefficient calculated from the physical analog data and does not predict the phase response. By scaling the Widess equation, an

easily-invertible relationship to be used on field data may be developed. The scale factor, however, appears to depend on dielectric permittivity because the Widess equation does a good job predicting the magnitude of reflection coefficient for an air-filled fracture (*see* Burns, 2008), but overestimates it for a water-filled fracture, as shown in this research. More work is needed to determine the scaling factor needed to invert real-world data using the Widess equation.

3.6 Conclusions

Calculated reflection coefficients from the physical analog indicate a strong dependence on fracture aperture below the resolution limit of λ/4 and a dependence on conductivity at conductivities higher than 2000 mS/m. Comparison among the three theoretical equations and the numerical modeling indicates that the numerical modeling best replicates the measured relationship between reflection coefficient, fracture aperture, and conductivity. The numerical modeling slightly overestimates the reflection coefficient, but this is likely due to the simplicity of the representation of the GPR antennas in the model. More sophisticated modeling of the antennas may produce better results.

The numerical modeling done with GPRMax2D best predicts the variation of the phase of the reflected wave with changing aperture and conductivity. Out of the

theoretical equations, the Annan equation produces the most accurate results, but the magnitude and the behavior at large apertures and high conductivities differ from the phase response measured over the physical analog.

The accuracy of the numerical modeling does, however, allow for testing that cannot be easily accomplished using the physical analog. Characterizing the GPR response to a constant and continuous fracture, along with initial characterization of the response to changes in fracture lateral extent (*see* Chapter 4) is the first step but does not represent a natural fracture surface. For example, surface roughness and variations on a scale smaller than the footprint of the GPR antenna will be averaged into each measurement and will, therefore, affect the calculated reflection coefficient and phase. Numerical modeling, because it appears to accurately represent actual GPR wave behavior, will allow future research to investigate the control of these variations without relying on a physical analog.

The primary application for the results of this research is to set the stage for an accurate inversion scheme that can extract fracture aperture from real-world data, but numerical modeling is next to impossible to invert. Any inversion would require a library of results for any contributing variable to changes in the reflection coefficient—e.g., host material, GPR system, fracture aperture, fracture depth, fracture fill, etc.—so a theoretical equation is preferable. The Widess

equation does not accurately predict phase response and significantly overestimates the reflection coefficient for any aperture/conductivity pair, but the predicted reflection coefficient has a similar shape to both the physical analog and numerical modeling results. With the addition of a scaling factor, the Widess model may be an option for future inversion applications. The scaling factor, however, appears to depend on the nature of the material filling the fracture – the Widess equation accurately matches the response to an air-filled fracture (Burns, 2008) but overestimates the response to a fluid-filled fracture - so calculation would require additional data generated by either the physical analog or numerical modeling.

Physical Analog

a)

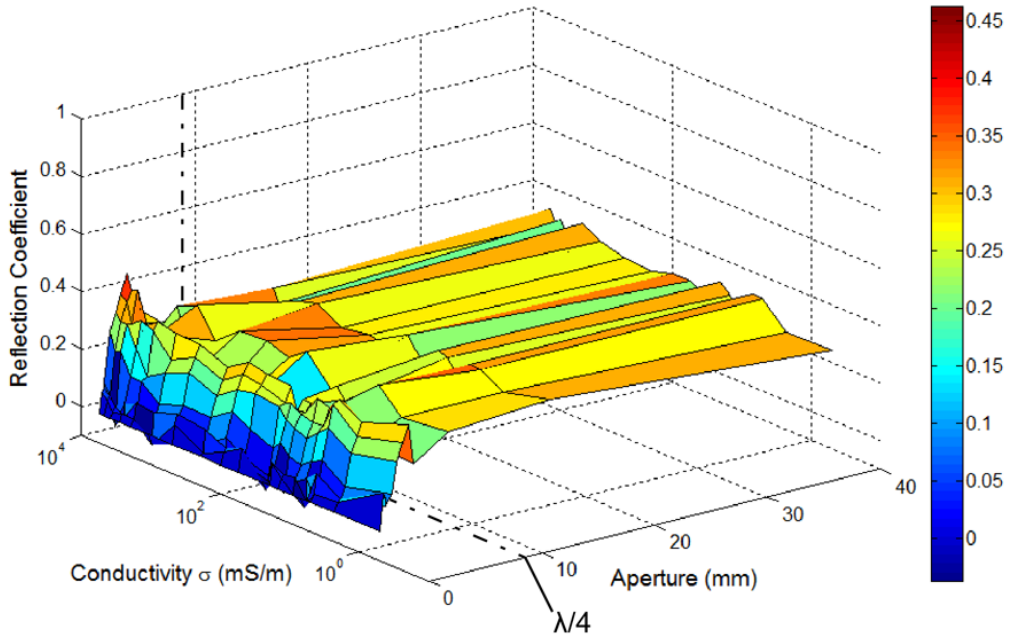

b)

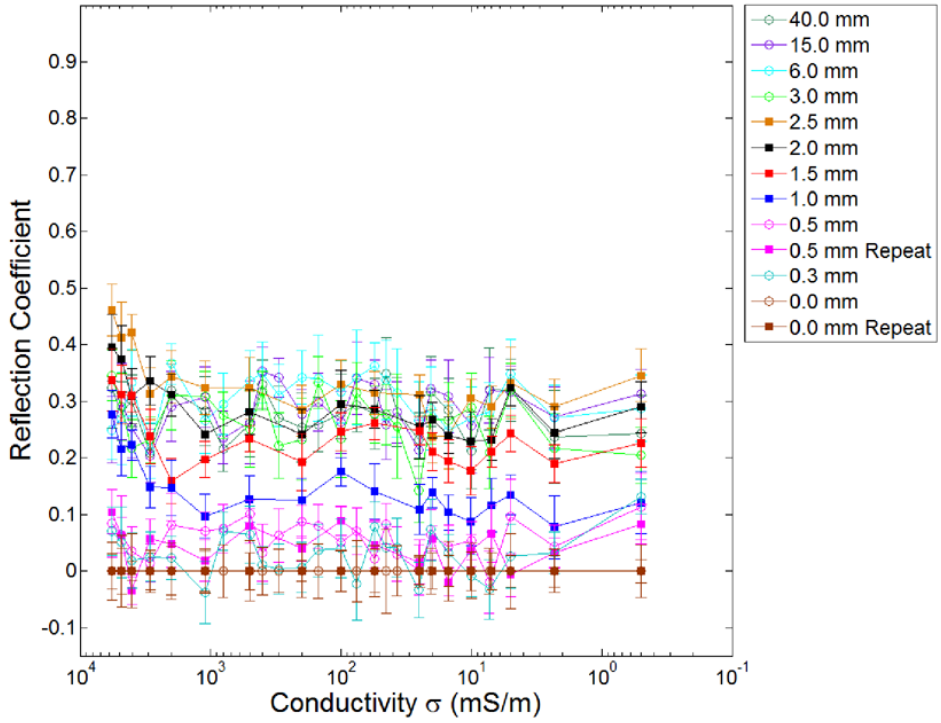

Figure 3.1. a) Reflection coefficient calculated from physical analog data versus conductivity and aperture, and b) Reflection coefficient versus conductivity at discrete apertures. Both plots show a steep increase of reflection coefficient below the resolution limit and an increase at higher conductivities.

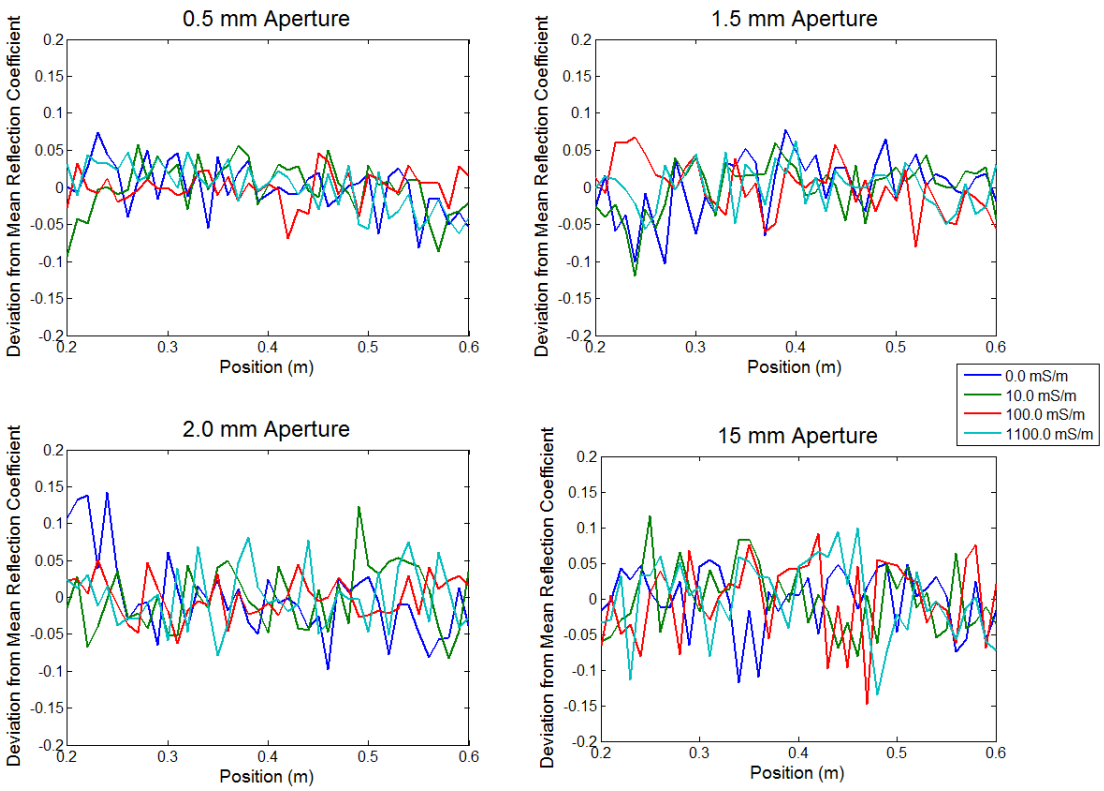

Figure 3.2. Reflection coefficient versus position for selected apertures and conductivities. Variation in reflection coefficient appears to be random, however, statistical analysis indicates that there is a slight dependence.

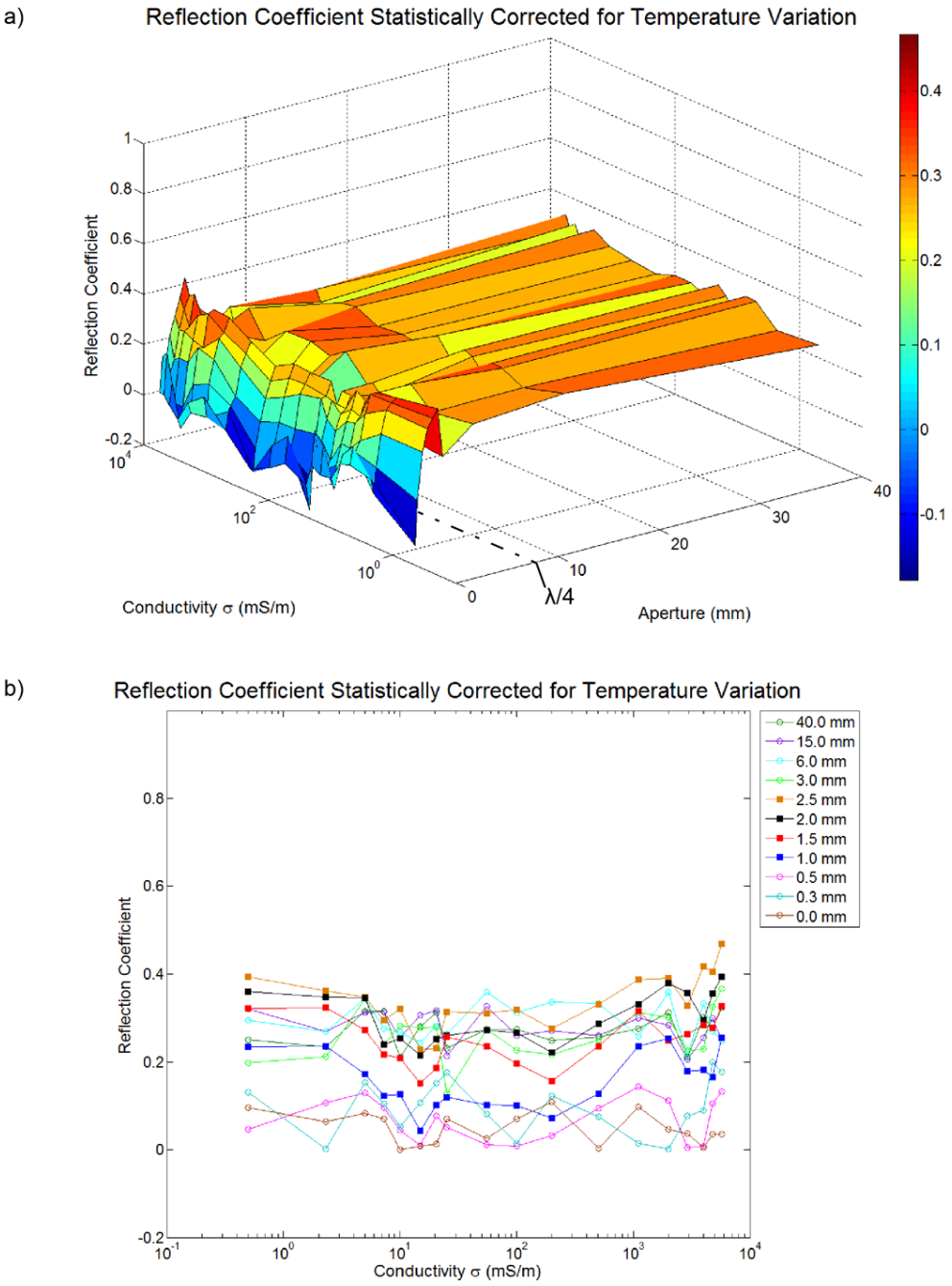

Figure 3.3. a) Temperature-corrected reflection coefficient calculated from physical analog data versus conductivity and aperture, and b) Temperature-corrected reflection coefficient versus conductivity at discrete apertures. Temperature correction was accomplished by statistically removing temperature dependence using an ANCOVA. Overall behavior of the reflection coefficient is similar to the simple correction shown in Figure 3.1.

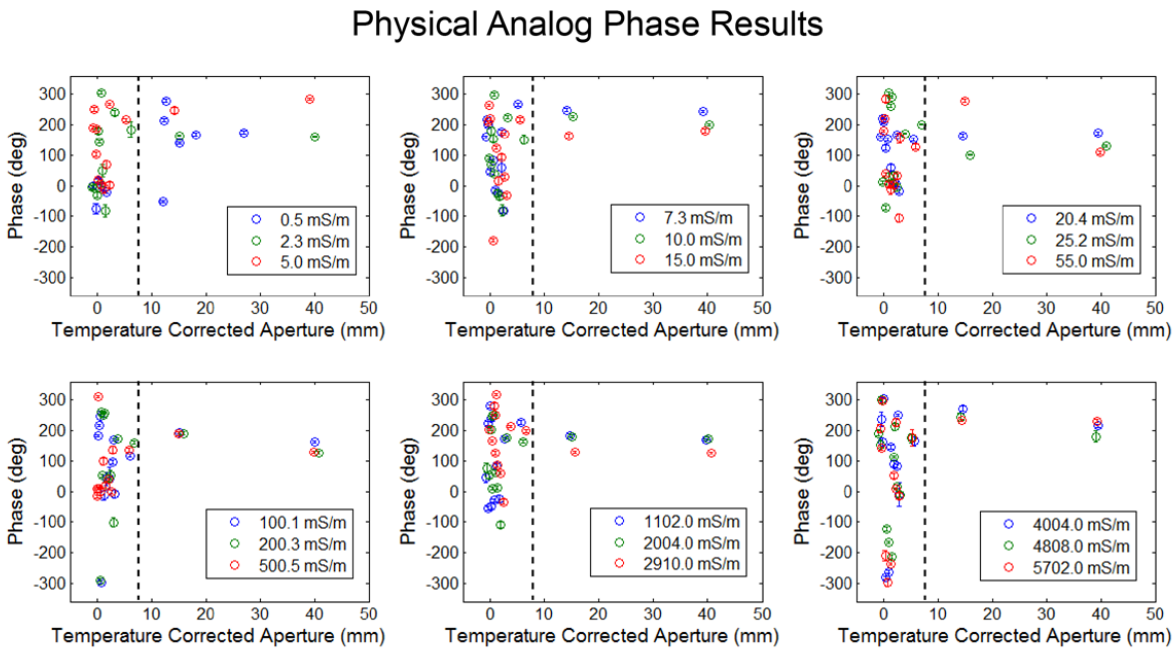

Figure 3.4. Phase response measured over the physical analog at discrete conductivities versus aperture. Phase increases over small fracture apertures, 0.0-3.0 mm, to a maximum of ~250°. The black dashed line marks the resolution limit.

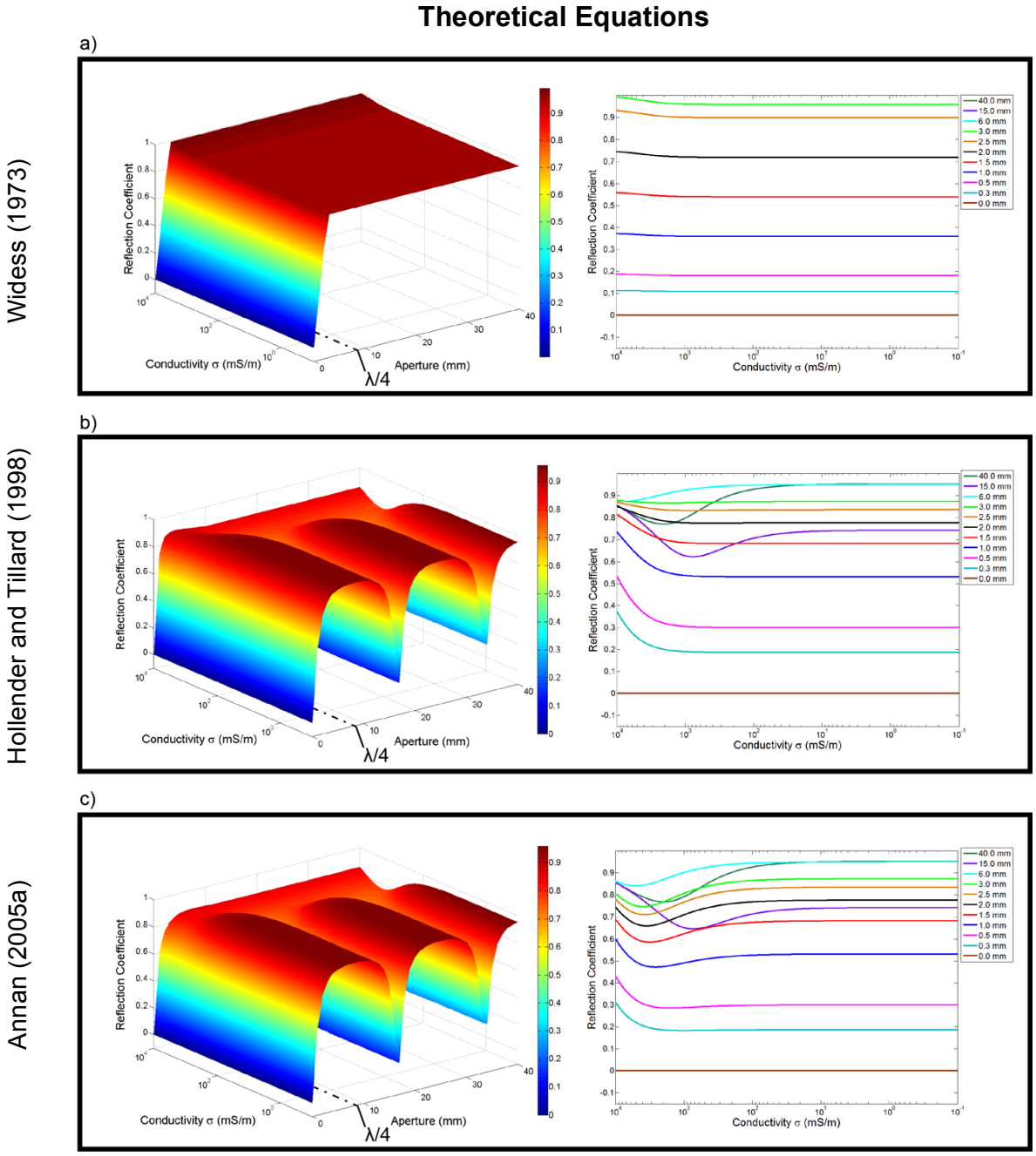

Figure 3.5. Results for the Widess (a), Hollender and Tillard (b), and Annan (c) equations. The Hollender and Tillard and Annan results predict low-reflection nodes and complex behavior at high conductivities not seen in either the Widess or physical analog results. All three theoretical equations have a steep response to changes in fracture aperture below the theoretical resolution limit and predict reflection coefficients larger than measured with the physical analog.

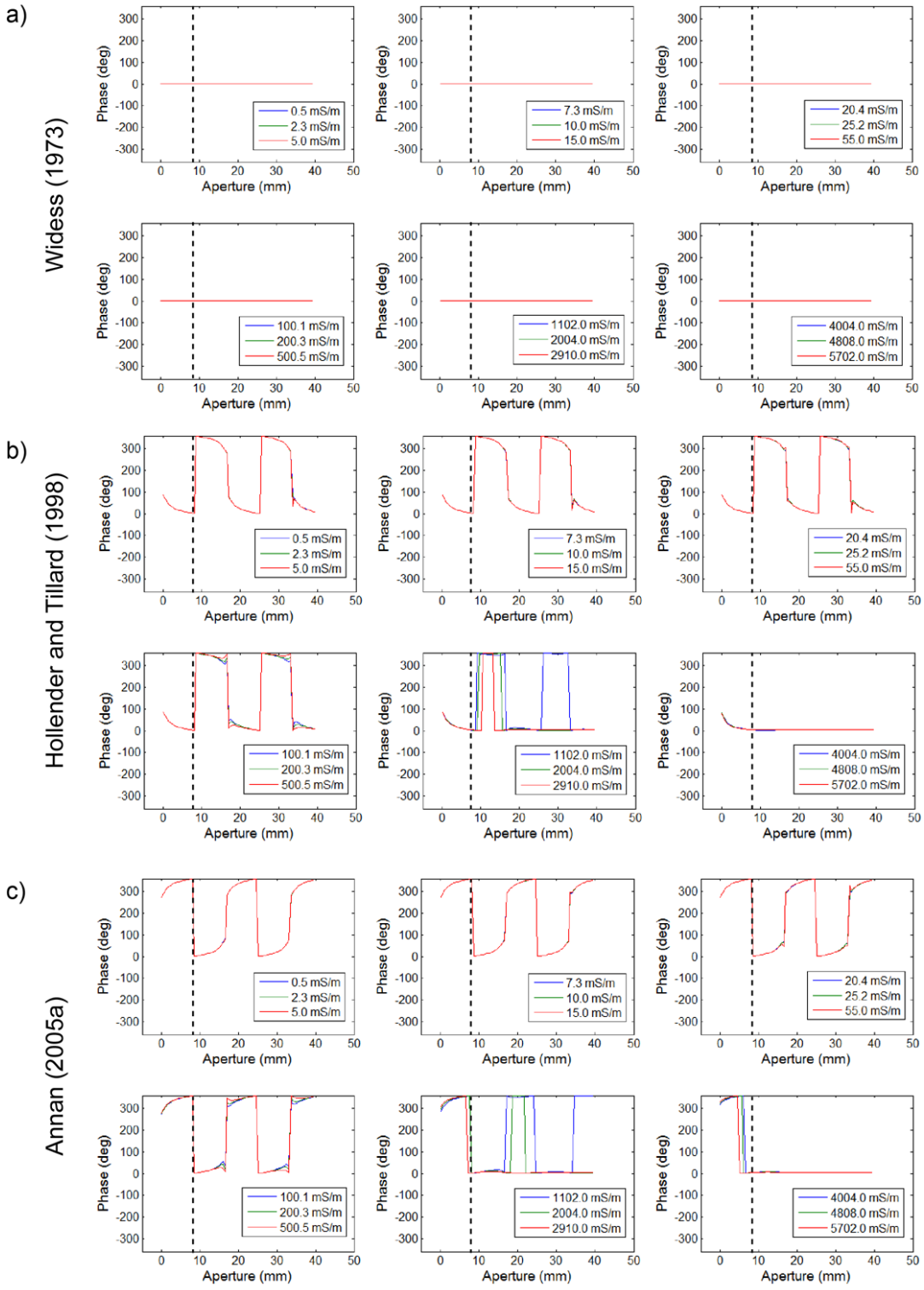

Figure 3.6. Phase results for the Widess (a), Hollender and Tillard (b), and Annan (c) equations. The Hollender and Tillard and Annan results predict decreasing and increasing phase response, respectively, and limited response at high conductivities not seen in the physical analog results. The Widess results predict no phase response. The black dashed line marks the resolution limit.

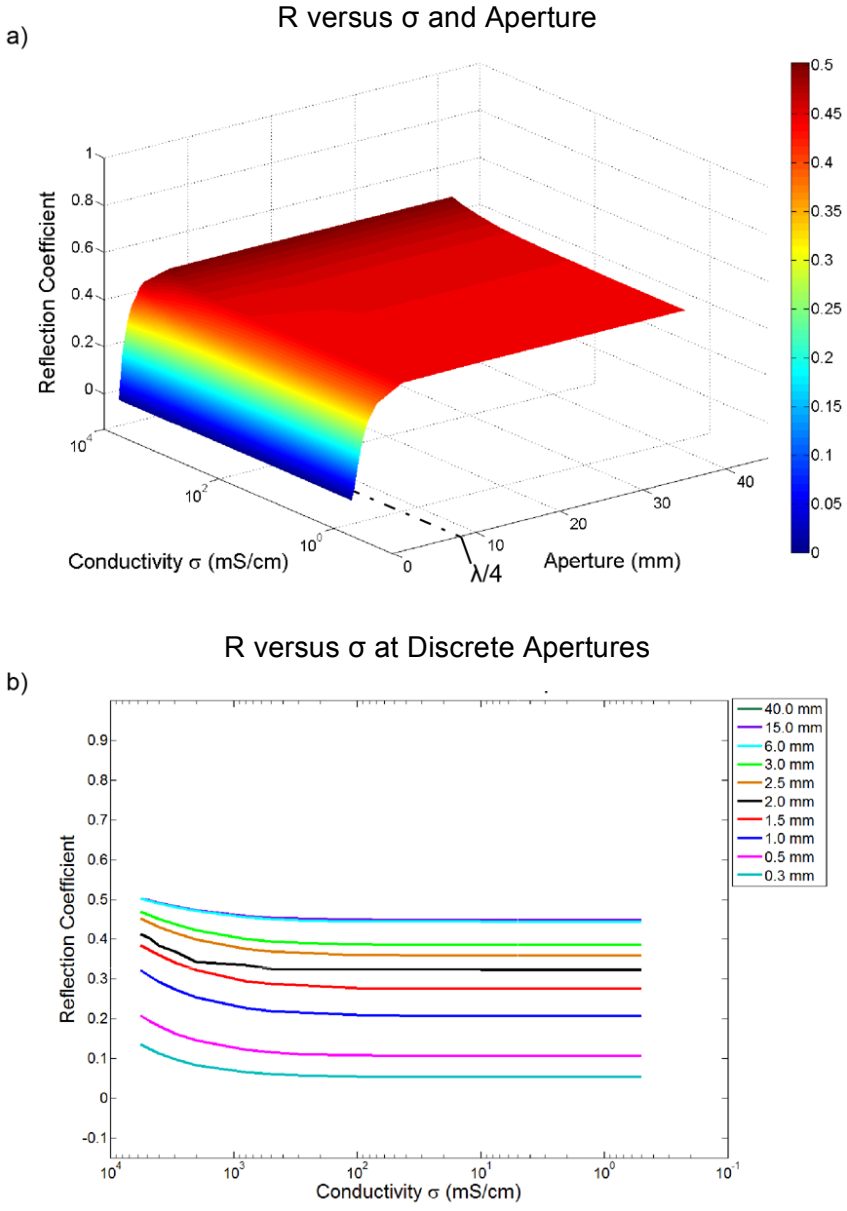

Figure 3.7. Reflection coefficient from the GPRMax2D numerical models versus conductivity and aperture (a) and versus conductivity at discrete apertures (b). The numerical modeling predicts a steep increase in reflection coefficient at fracture apertures smaller than the resolution limit and a slight increase at high conductivities.

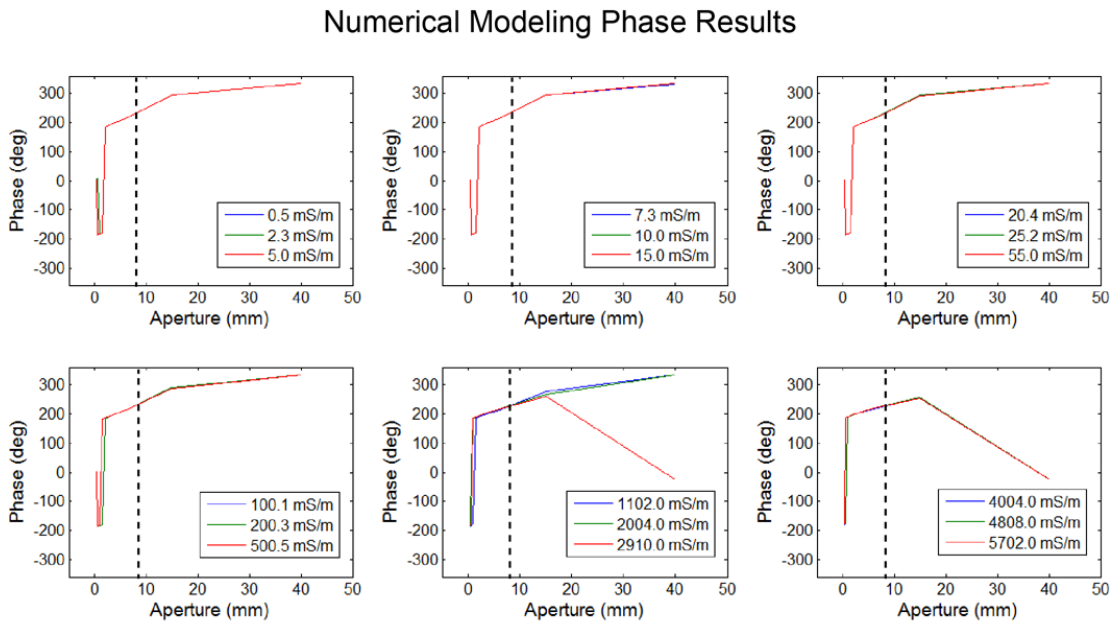

Figure 3.8. Phase from the GPRMax2D numerical models at discrete conductivities versus aperture. The numerical modeling predicts a steep decrease and increase in phase at fracture apertures smaller than 3.0 mm and a decrease at high conductivities for a 40.0 mm aperture. The black dashed line marks the resolution limit.

CHAPTER 4: LATERAL FRACTURE EXTENT

4.1 Abstract

Accurate characterization of subsurface fractures is indispensible for contaminant transport and fresh water resource modeling because discharge is cubically related to the fracture aperture; thus, minor errors in aperture estimates may yield major errors in a modeled hydrologic response. Ground penetrating radar (GPR) has been successfully used to identify fractures larger than the system's resolution limit, and Chapter 3 indicates that GPR amplitude response in combination with numerical modeling can characterize laterally extensive sub-resolution fractures. However, all GPR systems also have horizontal resolution limits, so characterization of fractures with lateral extents smaller than the resolution of the GPR system also relies on non-traditional interpretation. Therefore, the response of a 1000 MHz PulseEKKO Pro transducer to a fluid-filled bedrock fracture analog composed of two plastic (UHMW-PE) blocks was investigated, where lateral fracture extent ranged from 0-20 cm and fluid conductivity from 20-5700 ± 5 mS/m. The GPR profiles are acquired parallel and perpendicular to the fracture, normalized to the control response at zero aperture, the reflection coefficient is calculated by dividing the response by the magnitude of the direct wave, and the instantaneous phase is calculated using a Hilbert transform. Comparison of the measured GPR response to numerical modeling suggests that numerical modeling predicts the phase and amplitude response variations for changes in fracture lateral extent. The Widess equation

combined with an empirically derived scaling factor also predicts GPR amplitude response but not phase. Future applications to inversions of field data to map subsurface fracture networks will rely on easily invertible models, and numerical modeling using GPRMax2D can help develop a theoretical model for computationally effective and accurate inversion.

4.2 Introduction

Chapter 3 considered the simple case of a fracture with constant aperture and infinite extent. In a real world case, fractures have finite extent, and detection of finite, horizontally-limited fractures is constrained by the resolution of the system. As with detecting separate reflections from the top and bottom interfaces of a fracture, reflections from two laterally separated points can only be distinctly identified when the separation is greater than the resolution (*see* Figure 1.2). Annan (2005a) derived an expression for lateral resolution that corresponds to the radius of the Fresnel zone.

$$\Delta l = \sqrt{\frac{D\lambda_1}{2}} \tag{4.1}$$

where:

$\Delta l = lateral\ resolution, m$

$D = depth\ to\ the\ interface, m$

$\lambda_1 = wavelength\ in\ layer\ 1, m$

Below the resolution limit, the reflections from the fracture are superimposed and effectively averaged over the width of the GPR footprint. This perturbs the amplitude of the wave and generates an anomaly that cannot be adequately interpreted. For example, two fractures with unequal lateral extents that are smaller than the resolution limit of the system would appear as a single anomaly.

Results from Chapter 3 suggest, however, that sub-resolution features do have a predictable effect on the amplitude of the reflected GPR wave. Here, the GPR response to horizontal fractures with constant aperture and lateral extents both shorter and longer than the resolution limit are investigated using a physical bedrock fracture analog. The results are compared to numerical modeling to evaluate the accuracy of the GPRMax2D results.

4.3 Methodology

Two 6.8 ± 0.2 mm sheets of ultra-high molecular weight polyethylene (UHMW-PE) placed between the top and bottom block form a horizontally finite fracture model (*see* Figures 1.3 and 2.2). The contact between the two sheets was parallel to the centerline of the block, and the separation between the two edges of the sheets were adjusted to form a rectangular fracture centered on the centerline of the block. Inflexible spacers were used to set the lateral extent for

each conductivity measurement. Data were collected over all four fractures for each conductivity before increasing the conductivity (*see* Chapter 2 for full discussion).

Unlike the fracture aperture test (*see* Chapter 3), only results from the physical analog and numerical modeling were compared. The theoretical equations calculate reflection coefficients for a single point and so inherently assume infinite extent of the interface. For investigation of the response to changes in lateral extent, the interfaces are inherently finite. An analytical model could apply the theoretical equations to each point in a discretized mesh representing the system (Annan, 2005a) but would also have to combine those values with antenna radiation patterns to accurately predict GPR response.

4.3.1 Physical Analog

The lateral resolution is related to the time delay between the reflected wavelets from each target and is, therefore, dependent on EM propagation wavelength in the matrix, as opposed to in the fluid in the fracture. The lateral resolution in the block is 13.2 cm (*see* Equation 4.1 with values from List 2.1). This is significantly bigger than the vertical resolution within the fracture because the wavelength in water is much shorter due to the higher dielectric permittivity. Data were collected over two fractures with lateral extents smaller than the resolution limit and two larger (List 4.1).

List 4.1. Lateral extents and conductivities measured in the fracture lateral extent test. Green highlighted cells are fracture extents smaller than the resolution limit and red highlighted cells are larger.

Fracture extent (cm)

5.0	10.0	15.0	20.0

Fluid Conductivity (mS/m)

20.0	500.0	1000.0	1500.0	2000.0	3000.0	4000.0	5000.0

Conductivities ranging from 20-5700 mS/m (*see* List 4.1) were selected, with the majority of data points focused on the higher end of the range. Reflection coefficient is relatively independent of conductivity except at high conductivities for an infinite fracture (*see* Chapter 3), so the selected conductivities provide additional data points to characterize that relationship.

Measuring over a fracture with finite lateral extent in a physical analog has the potential to suffer from the same errors as in the vertical resolution test (*see* Section 2.1 for full discussion); namely, air bubbles and temperature variation effects. The same procedure was implemented for clearing air bubbles from the fracture as described in Chapter 3. No correction for the temperature variation and possible expansion and contraction of the block was used for this test

because all data were collected over four days when temperature fluctuations were minimal.

The main source of error in this test is the use of a different top block of the same material from the one used in the fracture aperture test (Chapter 3). The top block used by Burns (2008) was left on inserts at all four corners for four years, resulting in a measurable sag of approximately 3 mm from edge to center. Across the maximum width of the fracture, however, the variation in fracture aperture is less than 0.5 mm. Results from the fracture aperture test suggest that there is little variation in reflection coefficient with increasing aperture from 3 mm to 6 mm aperture, so this variation should introduce a limited error in the results.

4.3.2 Numerical Model

The GPRMax2D program was used to model GPR response from a rectangular fracture in a block of UHMW-PE. GPRMax2D is more computationally efficient than GPRMax3D but does assume infinite extent perpendicular to the simulated GPR line. This assumption is reasonable in this case because the footprint of the GPR is small compared to the size of the physical analog. Because the fracture aperture varies across the 2D model, a GPR profile composed of 100 traces was simulated, as opposed to a single trace (used for the fracture aperture test and described in Section 3.3.3). The model step size for the GPR antennas was 0.01 m, the same as in the physical analog data. The numerical modeling was run

after gathering the physical analog data using the actual conductivity values measured in the field.

4.4 Results

The 2D plots in each section present the reflection coefficient and phase versus position along the GPR profile. The data plotted are from the GPR profile down the centerline of the block perpendicular to the fracture. Black dashed lines indicate the position of the fracture edges and green dashed lines indicate the center of the fracture in Figures 4.1-4.4.

4.4.1 Physical Analog

Figure 4.1 shows the reflection coefficient measured over the physical analog for a fracture with lateral extent of: (a) 5 cm, (b) 10 cm, (c) 15 cm, and (d) 20 cm. Conductivity variations of the fluid result in no consistent variation in reflection coefficient, but lateral fracture extent does appear to control reflection coefficient. Reflection coefficient increases with increasing fracture extent from a maximum of 0.3 to 0.55 and shows a slight peak in the center for both the 15 cm and 20 cm wide fractures (*see* Figure 4.1c and d). For all fractures, the first increase in reflection coefficient occurs at approximately 10 cm from the edge of the fracture.

The center 15 traces from each fracture were used to calculate an Analysis of Variation (ANOVA) evaluating the significance of lateral extent and fluid conductivity on the measured reflection coefficient (*see* Table 4.1). Although conductivity does not appear to be significant in Figure 4.1, the ANOVA results suggest that both conductivity and lateral extent are significant.

Table 4.1. Results of the ANOVA for the fracture lateral extent data presented in Figure 4.1. Fracture lateral extent has the most significant control on the reflection coefficient.

Source	Degrees of Freedom	Type I SS	Mean	F Value	Pr > F
Model	31	3.21	0.10	80.34	< 0.001
Lateral Extent	3	2.92	0.97	756.38	< 0.001
Conductivity	7	0.13	0.02	14.29	< 0.001
Ex*Cond	21	0.16	0.01	5.77	< 0.001

The results were taken over four days with limited temperature variation and the block shape did not vary throughout the testing. Temperature variation is not corrected in these results, therefore, and an ANCOVA was not evaluated.

Figure 4.2 shows phase variation measured across the physical analog versus position for four fracture lateral extents and eight conductivities. Phase response increases from 0° to ~280° at the edge of each fracture. Phase variation is independent of conductivity within the error bars of the measurements.

4.4.2 Numerical Model

Figure 4.3 shows calculated reflection coefficients for a (a) 5 cm, (b) 10 cm, (c) 15 cm, and (d) 20 cm fracture. As with the physical analog, reflection coefficient increases with increasing fracture extent and shows a slight peak for both 15 cm and 20 cm wide fractures (*see* Figure 4.3c and d). The magnitude of the reflection coefficients is, however, larger than that measured in the physical analog—e.g., a maximum of 0.2 for a 5 cm wide fracture versus the measured reflection coefficient of 0.3—and the first increase in reflection coefficient occurs at approximately 15 cm from the edge of the fracture.

Numerical modeling, however, does predict slight variation with changes in conductivity. The maximum range in reflection coefficient due to conductivity variations is 0.1 (*see* Figure 4.3d). This variation is well within the error bars of the reflection amplitude calculated for the physical analog, but is significant in the physical analog data as calculated from the ANOVA (*see* Table 4.1).

Figure 4.4 shows phase variation calculated from numerical modeling results versus position for four fracture lateral extents and eight conductivities. Phase response decreases from 0° to -100° at ~10 cm from the edge of the fracture. Phase variation is independent of conductivity.

4.5 Discussion

For features smaller than the lateral resolution of the system, the profiles appear similar (*see* Figure 4.5). Standard GPR interpretation techniques cannot extract accurate fracture extent. The increase in reflection coefficient, however, occurs approximately 10 cm from the edge of the fracture for all fracture extents. This provides a distinct measurement of fracture extent.

As with the fracture aperture test described in Chapter 3, numerical modeling does predict reflection coefficient magnitudes that are close to the measured reflection coefficients of the physical analog. The shape of the curves is approximately the same, including the peaks in reflection coefficient at the center of the fracture seen in the 15 cm and 20 cm wide fractures (*see* Figure 4.1 and 4.3c and d). The numerical modeling suggests a predictable dependence on conductivity that the results from the physical model do not show, but the variation is within the error bars of the data collected from the physical model.

The numerical modeling overestimates the magnitude of the reflection coefficient and predicts a wider anomaly than what was measured over the physical analog. The increase in reflection coefficient occurs approximately 15 cm from the edge of the fracture, as opposed to 10 cm from the edge of the fracture as shown in the results from the physical analog. The difference here is likely related to the

simplification of the GPR antennas in the numerical modeling (*see* Section 3.5 for full description). Further work is needed to determine if improvement of GPR antenna modeling results in more accurate replication of field results.

The slight difference in response at the center of the anomaly—a high peak for a 5 cm wide fracture, and a broad, shallow peak for the three other fracture extents—could be due to the variation in fracture aperture caused by the warp in the top UHMW block. The anomaly, however, is well reproduced by the numerical modeling, which does not include the sag in the block, suggesting that the shape of the anomaly is not due to error in the physical model.

The peaks in the center of the anomalies may be caused by the vertical edges of the UHMW sheets used to form the fracture. Diffraction of the wave around the edge would affect the reflection coefficient. Further investigation using numerical modeling can help determine the source of this shape and behavior of GPR reflection coefficient over a more natural fracture with pinched-out edges as opposed to vertical termination.

The absolute magnitude of the phase change predicted by numerical modeling does not match the phase measured across the physical analog, but the overall behavior is similar. The phase varies consistently with distance from the fracture edge and the lateral extent of the fracture. The difference between the magnitude

and shape of the response is likely due to the simplification of the model, as discussed for the amplitude results above. More sophisticated modeling of the antennas may improve the match of the absolute magnitude of the phase.

Results from the fracture aperture test (*see* Chapter 3) suggest that among the three standard theoretical equations, the Widess equation (1973) best replicates real-world behavior of the GPR wave. The physical analog results for the lateral fracture extent test cannot be compared to the theoretical equations, as described in Section 4.3. Although numerical modeling can help provide better characterization of GPR amplitude response to fractures of finite extent, inversion of field data using a numerical model is complicated if not impossible. Development of a theoretical equation that accurately replicates the physical model results from this test is preferable.

4.6 Conclusions

The fracture aperture test detailed in Chapter 3 assumes a constant and infinite fracture aperture. To better understand response to real-world fractures—i.e., fractures with finite extent—and to characterize GPR amplitude response to fractures with lateral extent smaller than the lateral resolution limit of the system, results from the physical analog and numerical modeling were compared for four finite fractures, two larger and two smaller than the predicted resolution limit.

The reflection coefficient and phase response across the fracture shows a characteristic shape. The reflection coefficient increases approximately 10 cm from the leading edge of the fracture and decreases to 0 at approximately 10 cm from the trailing edge, while phase increases at the leading edge of the fracture and decreases approximately 2 cm beyond the trailing edge. This allows for accurate measurement of fracture extent from the variation in reflection coefficient even from fractures that are smaller than the predicted lateral resolution limit.

Numerical modeling replicates the relationship between reflection coefficient, phase, and fracture aperture extent but underestimates the magnitude of the reflection coefficient and overestimates the width of the anomaly. This is likely due to the simple representation of the GPR antennas within the model. Improved modeling of the GPR antennas will be needed to determine whether the discrepancy is due to the nature of the GPRMax2D modeling accomplished in my test or whether the modeling simply does not accurately represent the GPR behavior in the real-world.

For future applications, inversion of real-world data using a numerical model is untenable as discussed in Chapter 3. Because of the nature of the theoretical equations, their robustness cannot be assessed without developing an analytical

model that incorporates the radiation patterns of the transmitting and receiving antennas. Out of the three theoretical equations, the Widess equation (1973) would likely best predict GPR amplitude behavior but would need a scaling factor. Further work is needed to evaluate and develop a readily invertible equation.

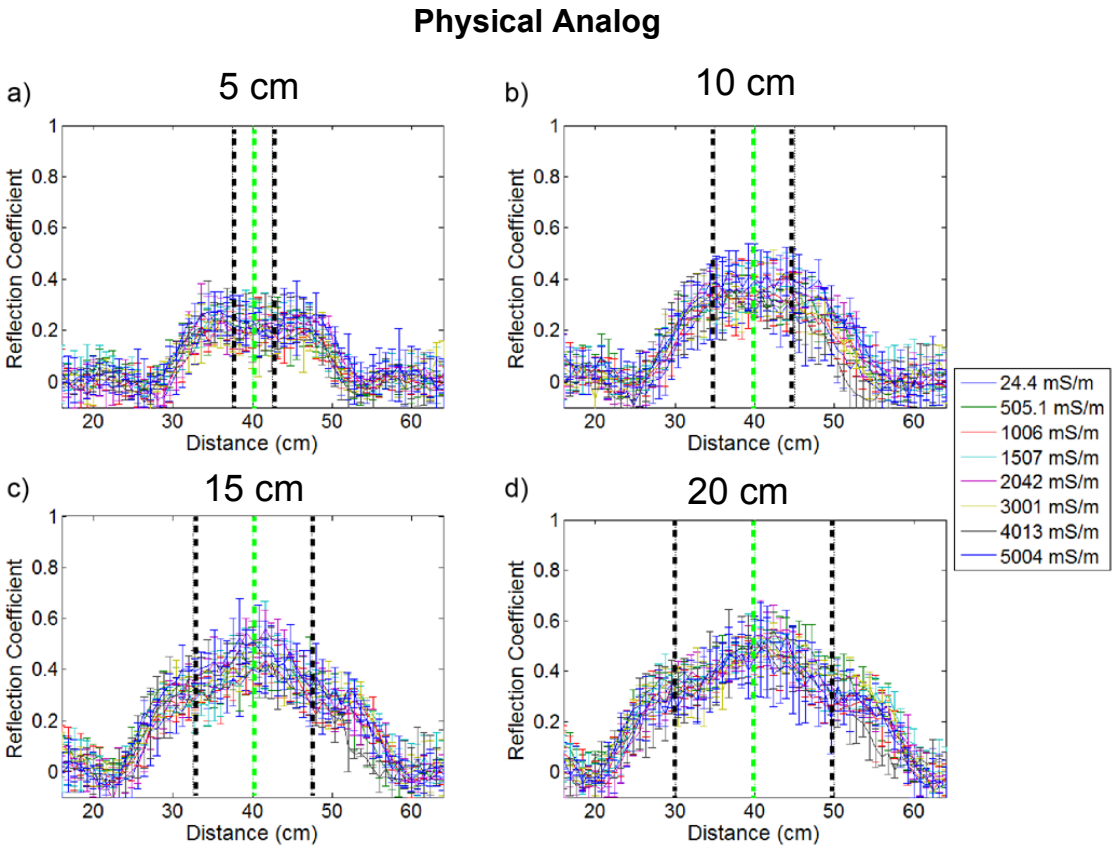

Figure 4.1. Reflection coefficient calculated from data from the physical analog over a fracture with lateral extent of 5 cm (a), 10 cm (b), 15 cm (c), and 20 cm (d). The green dashed line indicates the center of the fracture, and the black dashed lines indicate the edge. Increase in the reflection coefficient occurs at ~10 cm from the edge for each lateral extent.

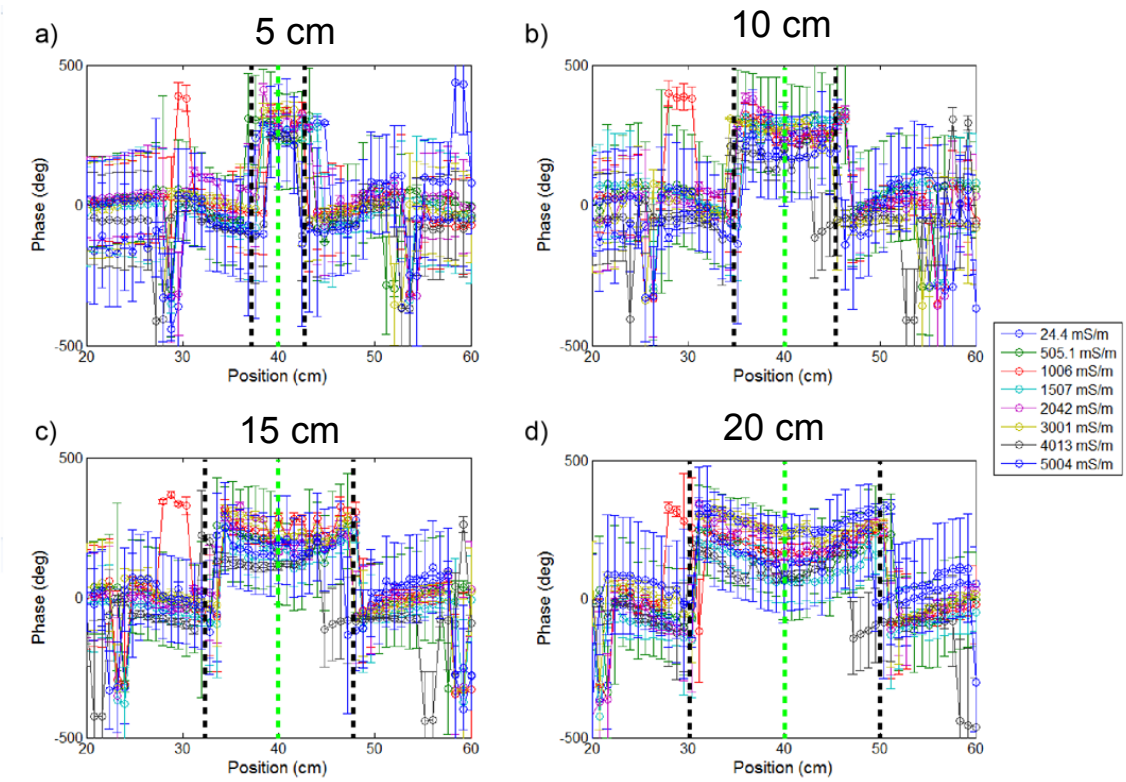

Figure 4.2. Phase calculated from data from the physical analog over a fracture with lateral extent of 5 cm (a), 10 cm (b), 15 cm (c), and 20 cm (d). The green dashed line indicates the center of the fracture, and the black dashed lines indicate the edge. Increase in phase occurs at approximately the edge of the fracture for each lateral extent.

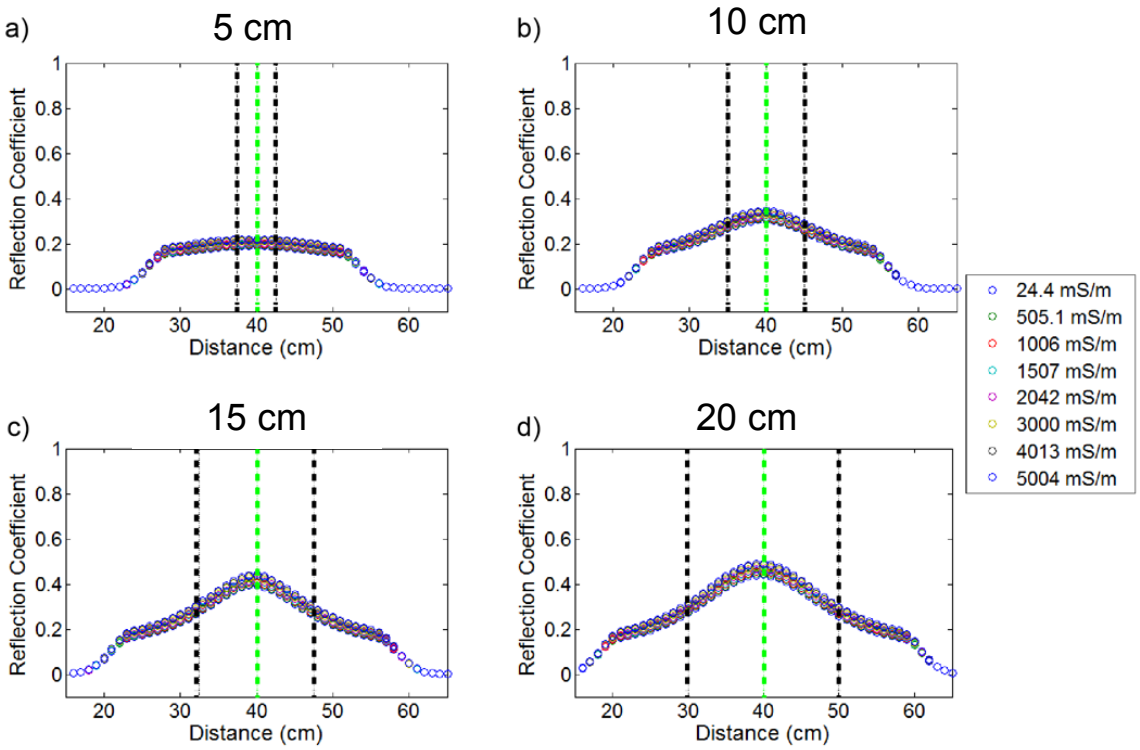

Figure 4.3. Reflection coefficient calculated from numerical modeling over a fracture with lateral extent of 5 cm (a), 10 cm (b), 15 cm (c), and 20 cm (d). The green dashed line indicates the center of the fracture, and the black dashed lines indicate the edge. Increase in the reflection coefficient occurs at ~15 cm from the edge for each lateral extent.

Numerical Modeling Phase Results

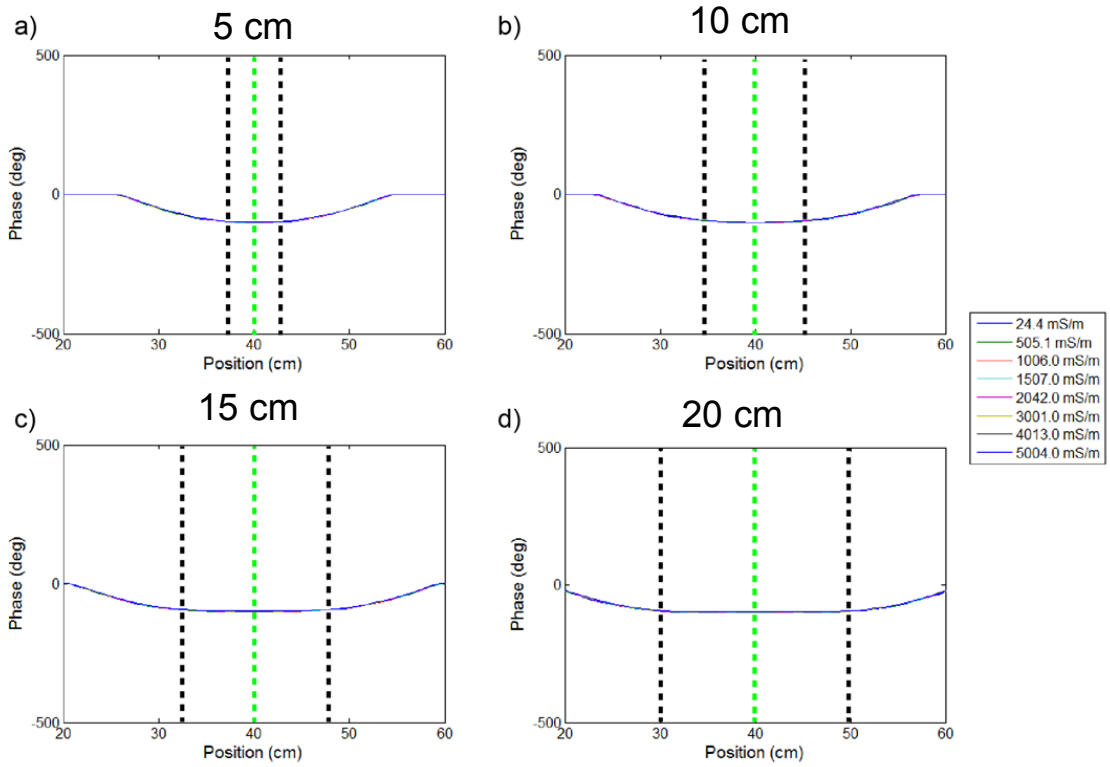

Figure 4.4. Phase calculated from numerical modeling over a fracture with lateral extent of 5 cm (a), 10 cm (b), 15 cm (c), and 20 cm (d). The green dashed line indicates the center of the fracture, and the black dashed lines indicate the edge. Decrease in the phase occurs at ~10 cm from the edge of the fracture for each lateral extent.

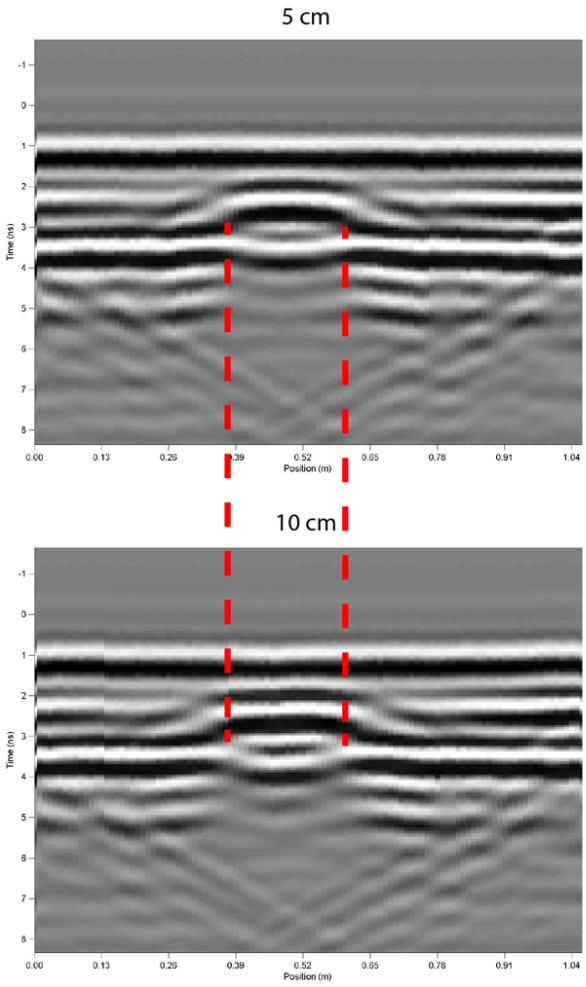

Figure 4.5. Example profile across a fracture with 5 cm (top) and 10 cm (bottom) lateral extent. The red lines indicate the extent of the center anomaly in the profile.

CHAPTER 5: CONCLUSIONS

5.1 Conclusions

Accurate characterization of subsurface fracture networks is indispensible for modeling of contaminant transport in groundwater. Even though previous researchers have demonstrated the applicability of GPR to characterize fracture networks, fractures below the resolution limit of the GPR system are not identifiable using standard interpretation techniques. Due to the cubic dependence of discharge on fracture aperture (Lamb, 1932; Snow, 1969), even small fractures can have strong control on groundwater flow, so characterization of sub-resolution fractures is imperative. Widess (1973), Hollender & Tillard (1998), and Annan (2005a) derived separate theoretical equations that suggest that fractures below the resolution have a predictable and measurable effect on the reflected amplitude of the wave related to the fracture aperture and the nature of the material filling the fracture. Although these equations have both been applied to and qualitatively evaluated on real-world data, the accuracy of these equations needs to be verified before they are used to invert data. To address this issue, results from a physical bedrock fracture analog with varying fracture aperture, extent, and fluid conductivity were compared to results from the three theoretical equations and from GPRMax2D modeling.

This research included three hypotheses: (1) the reflection amplitude of 1000 MHz GPR radar signal increases with both increasing conductivity and increasing fracture aperture, (2) Widess' equation for reflection amplitude is the best fit for

the 1000 MHz data, as suggested by data collected by Burns (2008) and (3) GPR reflection amplitude of 1000 MHz data has a low-slope relationship with conductivity, as predicted by my initial modeling. All three hypotheses are supported by the data, but the results from the physical analog suggest more complex relationships than expected.

In both tests—fracture aperture variation and lateral extent variation—the numerical modeling closely replicates the results from the physical analog. For the fracture aperture test, the physical analog results suggest that GPR reflection coefficient and phase for a 1000 MHz GPR system depends strongly on fracture aperture below the resolution limit, 0.0-8.0 mm, and reflection coefficient depends on fluid conductivity for high conductivity fluids, 2000+ mS/m. Numerical modeling in GPRMax2D generates reflection coefficients with higher absolute magnitudes than those measured with the physical analog, but the shape of the dependence on fracture aperture and conductivity is similar. The phase response predicted by the numerical modeling is similar in magnitude and response at low conductivities, with a slight deviation at 40 mm aperture and >1100 mS/m conductivity. For the fracture lateral extent, numerical modeling matches the shape of the anomaly, but predicts lower magnitude reflection coefficients and phase and a broader anomaly than measured over the physical analog. The discrepancy in magnitude for both tests and anomaly shape for the second test is likely due to the simple representation of the GPR antennas in the GPRMax2D

models. More sophisticated modeling including internal electronics (e.g., Warren and Giannopoulos, 2011) may improve the accuracy of the models.

Among the three tested theoretical equations, the Widess equation (1973) best predicts the reflection coefficient results from the physical analog but not the phase. All three equations overestimate the magnitude of the reflection coefficient, but do predict the steep increase in reflection coefficient with increase in fracture aperture for apertures less than the resolution limit. The zero reflection coefficient or low reflection coefficient nodes in both the Hollender & Tillard (1998) and the Annan (2005a) results are not present in the data from the physical analog and neither is the complex dependency on conductivity. Widess' equation (1973), however, shows a similar dependence on fracture aperture and conductivity as measured over the physical analog despite overestimation of the magnitude. This suggests that the Widess equation may be applicable if scaled properly.

5.2 Future Work

One of the most significant outcomes of the research presented here is the verification of numerical modeling as a viable proxy for the use of a physical analog. Although development of more accurate models requires further research, this result suggests that investigations of complex fracture geometries

(small scale variation of the aperture, dip of the fracture surface, termination of the fracture, surface roughness) and variations in the GPR system (frequency, collection parameters, etc.) can use GPRMax2D or 3D models as opposed to a physical analog. Most of these studies would be impractical, if not impossible, with a physical analog because of size constraints.

Although the numerical modeling represents the GPR amplitude response measured using the physical analog, it would be next to impossible to use as a technique to invert real-world data. Inversion using a numerical model would require a library of pre-calculated results encompassing all controlling variables – aperture, extent, fluid type, fluid conductivity, depth, etc. The Widess equation overestimates the magnitude but would be preferable for inversion applications. The results from the physical model as well as future results from the numerical modeling can help to determine a scaling factor for application of the Widess equation.

Besides contaminant transport modeling, this research may also apply to any investigation of sub-resolution fractures. Most fracture characterization applications, e.g. economic mining evaluations by Porsani et al. (2006) or rock fall hazard analysis (Orlando, 2003), do not require identification of sub-resolution fractures. The resolution of any GPR system is, however, dependent on the frequency and a trade-off exists between penetration depth and

resolution. Future application of the techniques investigated in my research may allow for use of lower frequency antennas without sacrificing resolution for fracture characterization. Furthermore, this can be applied to monitoring of micro-fractures in soils, levees, dams, or columns to better understand and predict failure envelopes.

LIST OF REFERENCES

Annan, A.P., 2005a, Ground-penetrating radar, in Butler D.K., ed., Near-surface geophysics: Society of Exploration Geophysics, p. 357-438.

Annan, A. P., 2005b, GPR methods for hydrogeological studies: Hydrogeophysics, 50, p. 185-213.

Baker, G.S., Jordan, T.E., and Talley, J., 2007, An introduction to ground penetrating radar (GPR): Geological Society of America Special Paper 432, p. 1-18.

Becker, M.W. and Tsoflias, G.P., 2010, Comparing flux-averaged and resident concentration in a fractured bedrock using ground penetrating radar: Water Resources Research, 46, W09518.

Berkowitz, B., 2002, Characterizing flow and transport in fractured geological media: a review: Advances in Water Resources 25, p. 861-884.

Boedeker Plastics Inc, 2013, Polyethylene Datasheet: http://www.boedeker.com/polye_p.htm (accessed February 2013).

Bradford, J.H. and Deeds, J.C., 2006, Ground-penetrating radar theory and application of thin-bed offset-dependent reflectivity: Geophysics, 71, p. K47-K57.

Burns, K.E., 2008, Ground penetrating radar investigations on the relationship between horizontal sub-wavelength 'thin-layer' bedrock fractures and reflection amplitudes (Master's Thesis).

Davis, J. L., and Annan, A. P., 1989, Ground-penetrating radar for high-resolution mapping of soil and rock stratigraphy: Geophysical Prospecting, 37, p. 531-551.

Day-Lewis, F. D., Lane, J. W., Harris, J. M., Gorelick, S. M., 2003, Time-lapse imaging of saline-tracer transport in fractured rock using difference-attenuation radar tomography: Water Resources Research, 39, p. 1290.

Deparis, J., and Garambois, S., 2009, On the use of dispersive APVO GPR curves for thin-bed properties estimation: theory and application to fracture characterization: Geophysics, 74, p. J1-J12.

Edmunds, M. P., 2012, Azimuthal seismic first-arrival tomography for the detection and characterization of hydraulically conductive fracture networks (Master's Thesis).

Giannopoulos, A., 2005, GPRMax2D/3D user's manual.

Goodfellow, 2013, Polyethylene – UHMW material information: www.goodfellow.com/E/Polyethylene-UHMW.html (accessed February 2013).

Grasmueck, M., 1996, 3-D ground-penetrating radar applied to fracture imaging in gneiss: Geophysics, 61, p. 1050-1064.

Gregiore, C., and Hollender, F., 2004, Discontinuity characterization by inversion of the spectral content of ground-penetrating radar (GPR) reflection – application of the Jonscher model: Geophysics, 69, p. 1414-1424.

Griffiths, D. J., 1999, Introduction to Electrodynamics, Third Edition: Upper Saddle River, N.J., Prentice Hall.

Grisso, R., Alley, M., Holshouser, D., and Thomason, W., 2009, Precision farming tools: soil electrical conductivity: Virginia Cooperative Extension. Publication, p. 442-508.

Hollender, F., and Tillard, S., 1998, Modeling ground-penetrating radar wave propagation and reflection with the Jonscher parameterization: Geophysics, 63, p. 1933-1942.

Jordan, T. E., Baker, G. S., Henn, K., and Messier, J. P., 2004, Using amplitude variation with offset and normalized residual polarization analysis of ground penetrating radar data to differentiate an NAPL release from stratigraphic changes: Journal of Applied Geophysics, 56, p. 41-58.

Jeannin, M., Garambois, S., Gregoire, C., and Jongmans, D., 2006, Multiconfiguration GPR measurements for geometric fracture characterization in limestone cliffs (Alps): Geophysics, 71, p. B85-B92.

LaBrecque, D. J., Sharpe, R., Wood, T., and Heath, G., 2004, Small-scale electrical resistivity tomography of wet fractured rocks: Groundwater, 42, p. 111-118.

Lamb, H., 1932, Hydrodynamics: Dover Publications, New York.

Leucci, G., Persico, R., and Soldovieri, F., 2007, Detection of fractures from GPR data: the case history of the Cathedral of Otranto: Journal of Geophysics and Engineering, 4, p 452.

Mellet, J. S., 1995, Ground penetrating radar applications in engineering, environmental management, and geology: Journal of Applied Geophysics, 33, p. 157-166.

Orlando, L., 2003, Semiquantitative evaluation of massive rock quality using ground penetrating radar: Journal of Applied Geophysics, 52, p. 1-9.

Porsani, J. L., Sauck, W. A., and Júnior, A. O. S., 2006, GPR for mapping fractures and as a guide for the extraction of ornamental granite from a quarry: a case study from southern Brazil: Journal of Applied Geophysics, 59, p. 177-187.

Porsani, J. L., Vagner, R. E., and Hiodo, F. Y., 2005, Geophysical inverstigations for the characterization of fractured rock aquifers in Itu, SE Brazil: Journal of Applied Geophysics, 57.

Puryear, C. I., and Castagna, J. P., 2008, Layer-thickness determination and stratigraphic interpretation using spectral inversion: theory and application: Geophysics, 73 p. R37-R48.

Robinson, J., Slater, L. D., Johnson, T. J., Ntarlagiannis, D., Lacombe, P., Johnson, C. D., Tiedeman, C. R., Good, D., Day-Lewis, F. D., Shapiro, A. M., and Lane, J. W., 2012, Towards improved 3D cross-borehole electrical resistivity imaging of discrete fracture networks: 2012 AGU Fall Meeting.

SAS, 2011, SAS 9.3 Software Overview Brochure: http://www.sas.com/software/sas9/ (accessed February 2013).

Sassen, D. S., and Everett, M. E., 2009, 3D polarimetric GPR coherency attributes and full-waveform inversion of transmission data or characterizing fractured rock: Geophysics, 74, p. J23-J34.

Sellman, P.V., Arcone, S. A., and Delaney, A.J., 1983, Radar profiling of buried reflectors and the groundwater table: CRREL Report 83-11, p. 1-10.

Sensors & Software Inc, 2003, EKKOView enhanced and EKKOView deluxe user's manual: Sensors & Software Inc.

Serzu, M. H., Kozak, E. T., Lodha, G. S., Everitt, R. A., and Woodcock, D. R., 2004, Use of borehole radar techniques to characterize fractured granitic bedrock at AECL's underground research laboratory: Journal of Applied Geophysics, 55, p. 137-150.

Snow D.T., 1969, Anisotropic permeability of fractured media: Water Resource Research, 5, p.1273-1289.

Talley, J., Baker, G.S., Becker, M.W. and Beyrle, N., 2005, Four dimensional mapping of tracer channelization in subhorizontal bedrock fractures using surface ground penetrating radar: Geophysical Research Letters, 32, p. 732-735.

Tsoflias, G.P. and Becker, M.W., 2008, Ground-penetrating-radar response to fracture-fluid salinity: why lower frequencies are favorable for resolving salinity changes: Geophysics, 73, p. J25-J30.

Tsoflias, G. P., Halihan, T., and Muldoon, M. A., 2004, Fracture fluid flow properties investigation using GPR and hydraulic testing methods: Tenth International Conference on Ground Penetrating Radar, p. 521-524.

Tsoflias, G. P., Halihan, T., and Sharp, J. M., 2001, Monitoring pumping test response in a fracture aquifer using ground-penetrating radar: Water Resources Research, 37, p. 1221-1229.

Warren, C., and Giannopoulos, A., 2011, Creating finite-difference time-domain models of commercial ground-penetrating radar antennas using Taguchi's optimization method: Geophysics, 76, p. G37-G47.

Widess, M.B., 1973, How thin is a thin bed?: Geophysics, 38, p. 1176-1180.

APPENDICES

Appendix A: Overview of Ground Penetrating Radar

For an in-depth discussion of Ground Penetrating Radar (GPR) techniques complete with governing equations, see both Baker et al. (2007) and Annan (2005a). This appendix contains a brief overview of GPR and various GPR techniques.

Ground Penetrating Radar systems use reflection and/or transmission of electromagnetic waves in the subsurface to develop a cross-sectional representation of contrasts in the dielectric permittivities in the subsurface. A GPR transmitting antenna emits a high frequency (12.5 - 2600 MHz) electromagnetic pulse into the subsurface. When the wave encounters an interface between two materials of contrasting dielectric permittivity, a portion of the wave is reflected and a portion is transmitted (*see* Figure 2.3). The receiving antenna measures either the reflections (in common offset or common midpoint modes, discussed below) or the transmissions (in cross-borehole mode, discussed below) as well as the difference in time between emission and reception. Signal amplitude plotted versus two-way travel time for a pulse at a single location produces a 'trace' (*see* Figure 2.4a), and a set of traces plotted along a profile line produces a cross-section of the subsurface (*see* Figure 2.4b).

The amplitude of the reflection from each interface depends on the contrast between the dielectric permittivities on either side of the interface. Higher contrast interfaces will produce stronger reflections. Figure A.1 lists dielectric permittivities for common materials. The high contrast between water and geologic materials, relative dielectric permittivity of 80 versus 3-40, means that GPR works well at identifying interfaces between water and rock, e.g. locating the water table (e.g., Sellman et al., 1983).

Material	ε_r; Davis and Annan (1989)	ε_r; Daniels (1996)	Velocity (m/ns)	Velocity (ft/ns)
Air	1	1	0.3	0.98
Distilled water	80		0.03	0.11
Fresh water	80	81	0.03	0.11
Sea water	80		0.03	0.49–0.57
Fresh water ice	3–4	4	0.15–0.17	0.35–0.49
Sea water ice		4–8	0.11–0.15	0.28–0.35
Snow		8–12	0.09–0.11	0.35–0.50
Permafrost		4–8	0.11–0.16	0.40–0.57
Sand, dry	3–5	4–6	0.12–0.17	0.18–0.31
Sand, wet	20–30	10–30	0.05–0.09	0.57–0.70
Sandstone, dry		2–3	0.17–0.21	0.31–0.44
Sandstone, wet		5–10	0.09–0.13	0.35–0.49
Limestones	4–8		0.11–0.15	0.37
Limestone, dry		7	0.11	0.35
Limestone, wet		8	0.11	0.25–0.44
Shales	5–15		0.08–0.13	0.33–0.40
Shale, wet		6–9	0.10–0.12	0.18–0.44
Silts	3–30		0.05–0.13	0.16–0.44
Clays	5–40		0.05–0.13	0.16–0.44
Clay, dry		2–6	0.12–0.21	0.40–0.70
Clay, wet		15–40	0.05–0.08	0.16–0.25
Soil, sandy dry		4–6	0.12–0.15	0.40–0.49
Soil, sandy wet		15–30	0.05–0.08	0.18–0.25
Soil, loamy dry		4–6	0.05–0.08	0.40–0.49
Soil, loamy wet		15–30	0.07–0.09	0.22–0.31
Soil clayey dry		4–6	0.12–0.15	0.40–0.49
Soil, clayey wet		10–15	0.08–0.09	0.25–0.31
Coal, dry		3.5	0.16	0.53
Coal, wet		8	0.11	0.35
Granites	4–6		0.12–0.15	0.40–0.49
Granite, dry		5	0.13	0.44
Granite, wet		7	0.11	0.37
Salt, dry	5–6	4–7	0.11–0.15	0.37–0.49

Figure A.1. List of dielectric permittivities and velocities for common materials (from Baker et al., 2007).

The large range of frequencies available for GPR allows for a number of different applications. The frequency of the emitted pulse controls both resolution and depth of penetration, where a higher frequency pulse will produce higher resolution data but will attenuate faster, reducing the depth that the system is able to image. This phenomenon is due to frequency dependence of the wave velocity and attenuation at frequencies greater than approximately 1000 MHz. At these high frequencies, attenuation increases significantly with increasing frequency. Furthermore, relaxation of water molecules at high frequencies increases the dissipation of the energy of the wave, drastically increasing the attenuation of the wave. Although this puts an upper limit on inherent GPR resolution, the wide range of useable frequencies allows for a wide range of applications.

Typically used frequencies range from 12.5 – 2600+ MHz, and the frequency is selected based on the application and data requirements. Lower frequency antennas have been used to map large scale features, e.g. bedrock, the water table, and contaminant plumes (e.g., Davis and Annan 1989; Bradford and Deeds, 2006; Jordan et al., 2004), and higher frequency antennas to map small scale, shallow features, e.g. underground storage tanks, rebar, large fractures, and rock competence (e.g. Mellet, 1995; Porsani et al., 2005).

As with the frequency, the target type and question to be answered dictate the most useful the orientation of the GPR antennas and mode of the survey. A brief discussion is included below.

Figure A.2 shows common antenna orientations for extensive (a) and discrete (b) targets. The Fresnel zone of the antennas – the area illuminated in the subsurface by the EM wave – is an ellipse with the long axis oriented perpendicular to the long axis of the antenna. Use of either parallel end-fire or parallel broadside orientations increases the signal received from targets off the survey line. This tends to increase noise in the measurement so most surveys are taken in perpendicular broadside orientation. Both the antenna orientation and the nature of the target, however, govern the behavior of the reflected wave. Although perpendicular broadside orientation generates data with the highest signal-to-noise ratio, other antenna orientations can provide valuable information about the nature of the subsurface, and data collected with all antenna orientations (3D polarimetric, e.g., Sassen and Everett, 2009) eliminates orientation biases.

All of the antenna orientations in Figure A.2 are defined for common offset (CO) survey mode, where the transmitting and receiving antennas are fixed with respect to each other and moved along a survey line at set intervals. This mode is akin to reflection seismology and produces a profile (*see* Figure A.3a).

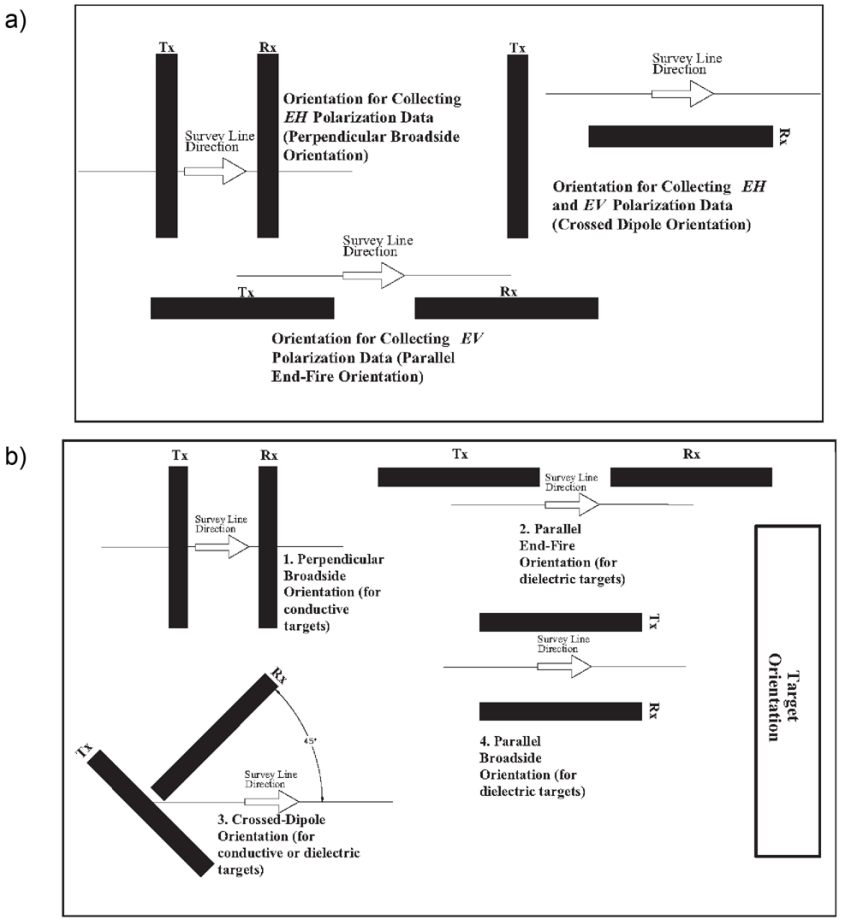

Figure A.2. Common antenna orientations for identifying extensive (a) and discrete (b) targets.

Data can also be collected in common midpoint survey mode (CMP, see Figure A.3b). The transmitting and receiving antennas are moved away from a central point at set intervals. This survey mode is akin to refraction seismology or seismic first arrival tomography, and allows for both velocity mapping and calculation of amplitude variation with offset (AVO) (Bradford and Deeds, 2006; Jordan et al., 2004). For the purposes of contaminant transport, AVO helps

detect and characterize the presence of contamination. This is of particular importance in areas where anomalies due to contamination can mimic stratigraphic anomalies—e.g., silt or clay lenses, or a perched water table (Jordan et al., 2004)— and in areas contaminated by non-aqueous phase liquids (NAPLs) forms a thin film on the water table (Bradford and Deeds, 2006).

Both CO and CMP survey modes use the transmitting and receiving antennas on the surface and measure reflections from interfaces in the subsurface, but GPR can be used to measure transmissions in a cross-borehole mode. In this mode, the receiver and transmitter are placed in separate boreholes and measure the transmission through the volume between the two at discrete points down the borehole. The resulting data must be processed using raypath tracing and tomography in order to interpret the subsurface characteristics. Day-Lewis et al. (2003) demonstrated imaging of the movement of a saline tracer through fractured bedrock using cross-borehole GPR data.

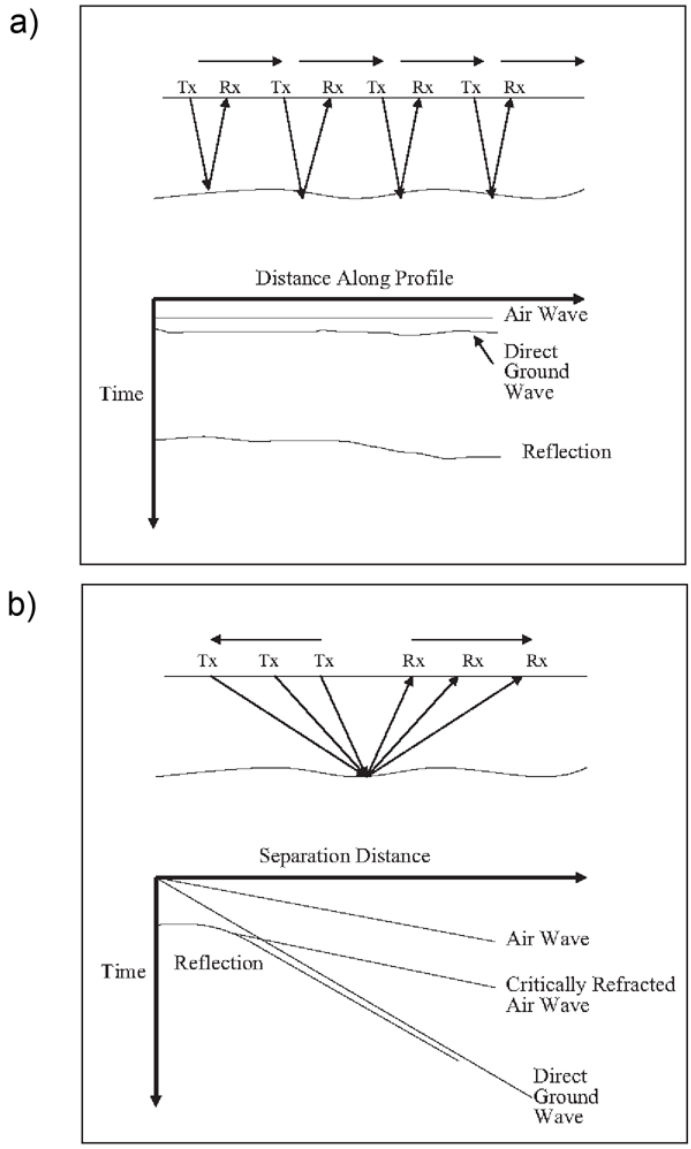

Figure A.3. Diagrams of common offset (a) and common midpoint (b) GPR data collection modes.

Appendix B: Physical Analog Materials

Ultra-high molecular weight polyethylene (UHMW-PE) is used for a variety of applications because of its negligible fluid absorption and high abrasion and impact resistance. For this application, UHMW-PE is an ideal substance. It is homogenous and isotropic, allowing for averaging over the entire survey line and averaging between survey lines of different orientations. Furthermore, UHMW-PE is a low density material. Edge effects from the edges of the block corrupt the reflected GPR signal, and use of a large block of low-density material minimizes those effects and the overall weight and maneuverability of the physical analog.

The blocks used in this study are natural UHMW-PE. UHMW-PE is also available in virgin, reprocessed and several other trade names. Although these other varieties of UHMW-PE are more expensive, they do not improve the abrasion, impact and chemical resistance of natural UHMW-PE. List B1 covers the physical properties of natural UHMW-PE characteristics.

List B1. Physical properties of UHMW-PE (Boedeker Plastics Inc, 2013; [a]Goodfellow, 2013).

Electrical properties	Value	Units
Surface resistivity	$>10^{15}$	Ohm/m^2
Volume resistivity[a]	$>10^{15}$	Ohm-m

Thermal Properties	Value	Units
Approximate melting point	136	°C
Coefficient of thermal expansion	11	10^{-5}K

Physical Properties	Value	Units
Density	0.93	g/cm^3
Water absorption	<0.01	%

The original blocks purchased by Burns in 2007 remained in the field under a semi-weatherproof tarp between the end of his research in 2008 and the beginning of this research in 2012. The top block sat on ~ 5 mm inserts at each of the corners, and measurements of the block in mid-2012 revealed that the center had sagged ~3 mm. Due to the small inherent resolution of a water-filled fracture and steep response of reflection coefficient with changes in fracture aperture at small apertures, an error in fracture aperture of ±1.5 mm along the survey line would generate unreasonable errors in the results. Although the sag could be mitigated by several hours of direct solar radiation on the surface of the block – where the expansion of the top of the block counteracted the central sag – that solution required high solar angles and perfect weather conditions, i.e. no clouds, to work. As this would have greatly limited the data collection, the original top block was replaced. The original, warped top block was used for the fracture lateral extent test and the new top block for the fracture aperture test. Over the widest fracture extent, 20 cm, the sag in the block was both not pronounced enough to greatly affect the results and was consistent through all of the data sets.

Only SABIC Polymershapes can supply UHMW-PE sheets of the required thickness with the required accuracy for this physical model. Both Total Plastics and Piedmont Plastics in Knoxville carry 6” UHMW, but the thickness accuracy is ±0.08 in. This would add an error of approximately ±2 mm to the fracture aperture and would not be a significant improvement over the warped block. SABIC Polymershapes supplied both the original blocks ordered by Burns in 2008 and the replacement top block purchased in 2012. See List B2 for contact information.

List B2. Contact information for the supplier of the UHMW-PE blocks, SABIC Polymershapes.

SABIC Polymershapes	
Website:	http://www.sabicpolymershapes.com
Address:	4703 Middlecreek Lane Knoxville, Tn 37921
Contact:	Joe Batchik Branch Manager - Knoxville, TN
E-mail:	joseph.batchik@sabic-ip.com
Telephone:	(865) 583-8200
Fax:	(865) 583-3088

Appendix C: Comparison to Previous Work on Physical Analog

C.1 Differences in Processing

Burns (2008) pioneered processing of data over the physical bedrock fracture analog used in my study. Figure C.1 diagrams his processing steps. A time zero recalculation of 1% was applied to the data, the time window was cropped to 10 ns (*see* Figure C.1b), the data were cropped the data to the center 41 traces before further cropping due to shifts in the GPR traces (*see* Figure C.1c), a DEWOW filter was applied, and all traces for a given aperture were averaged into a single trace and interpolated to 0.05 ns (*see* Figure C.1d).

To calculate the amplitude response, Burns normalized the fracture reflection to a 0 mm aperture data set. The data were exported from EKKO View Deluxe to a Parallel Geosciences' Seismic Processing Workstation (SPW) v2.2.7, and a static DC shift was applied in three iterations to match the airwave peak amplitudes (Burns, 2008). The normalization factor – direct wave amplitude for any given aperture divided by the direct wave amplitude for the 0.0 mm aperture – was calculated and each respective trace was divided by it. To remove direct wave contribution at the fracture aperture, the 0.0 mm trace was subtracted from the trace at any given aperture. These steps allowed for a single measurement of normalized and corrected reflection amplitude for each fracture aperture.

In the research presented here, similar processing steps were applied, including cropping in both traces and time, applying a DEWOW filter, and interpolating. However, a time zero recalculation was not applied, as the time of the fracture reflection was well constrained by Burns' work (2008), and the traces were not averaged prior to calculating the reflection amplitude.

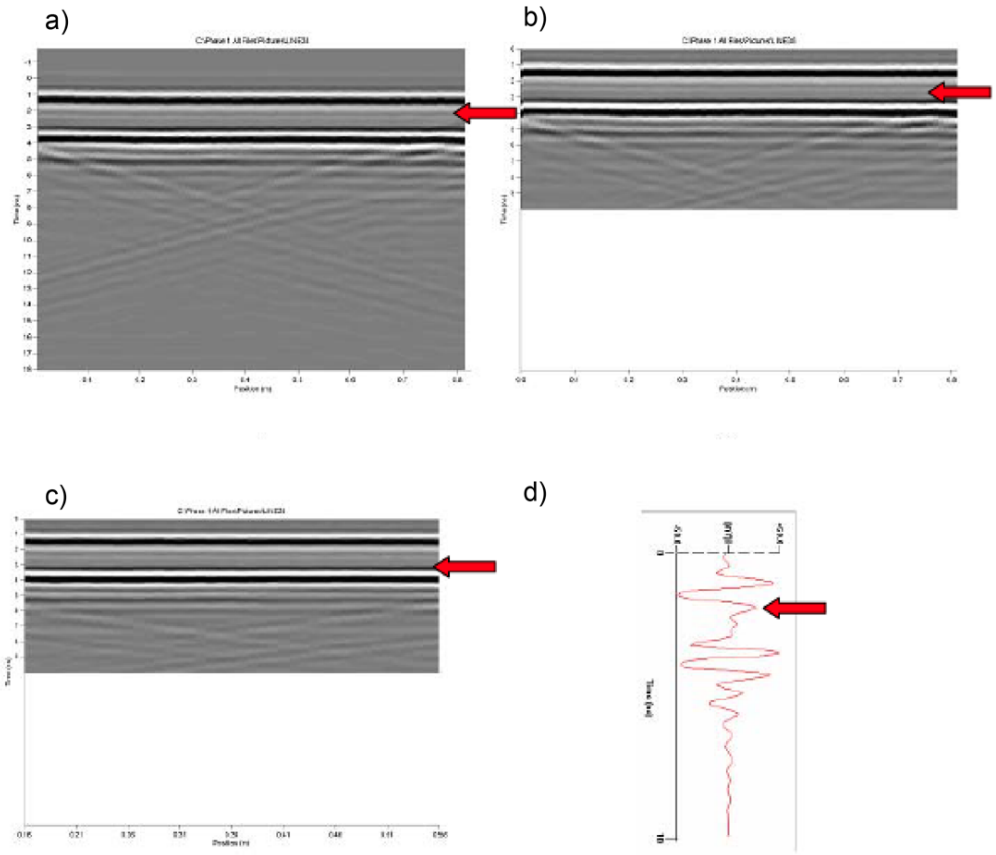

modified from Burns (2008)

Figure C.1. Processing applied by Burns (2008). Raw data (a) was clipped to the first 10 ns (b) and center 41 traces (c). The traces were averaged to a single trace (d).

Results from this research show the same jagged offsets in the ground wave (*see* Figure 2.7b). These are likely due to internal adjustments as the GPR warms up (G. Johnston, personal communication); however, 20 minutes of warm up time did not completely remove these jumps from the data. Extracting the amplitude for each trace separately before averaging the amplitudes allowed for the use of all 41 center traces. If the traces are averaged before the amplitude is extracted, static shifts between sets of traces introduce inherent errors into the results. By extracting and processing the amplitudes from each trace separately before averaging, the overall processing error is reduced and the measurement of the error in the final data set is improved—where 82 data points per aperture per conductivity are calculated, averaged, and the standard deviation can be determined, as opposed to a single data point per aperture with no measure of the standard deviation.

C.2 Comparison to Burns' Results for Varying Conductivity over Fixed Fracture Aperture

Though his research primarily focused on GPR amplitude response to air-filled fractures, Burns conducted a single test with fracture aperture fixed at 0.5 mm and fluid conductivity ranging from 0-5700 mS/m. Figure C.2 shows his results. Because he was only comparing between the results from the theoretical equations and from the physical analog, Burns measured the magnitude of the amplitude response in mV. He converted the calculated reflection coefficient from

the theoretical equations using the direct wave amplitude to convert the reflection coefficient. Furthermore, clipping of the reflected trace that was not observed in this data forced Burns to take measurements of a reflection multiple of the fracture. These two facts eliminate the possibility of direct comparison between his results and those measured in this study, but by approximating the direct wave amplitude at 30,000 mV, his results were converted to reflection coefficients (*see* y-axis on the right side of Figure C.2). The absolute magnitude cannot be compared between his results and the results of this study because he measured a reflection multiple, but the trend and relative spread of the estimated reflection coefficient can be compared.

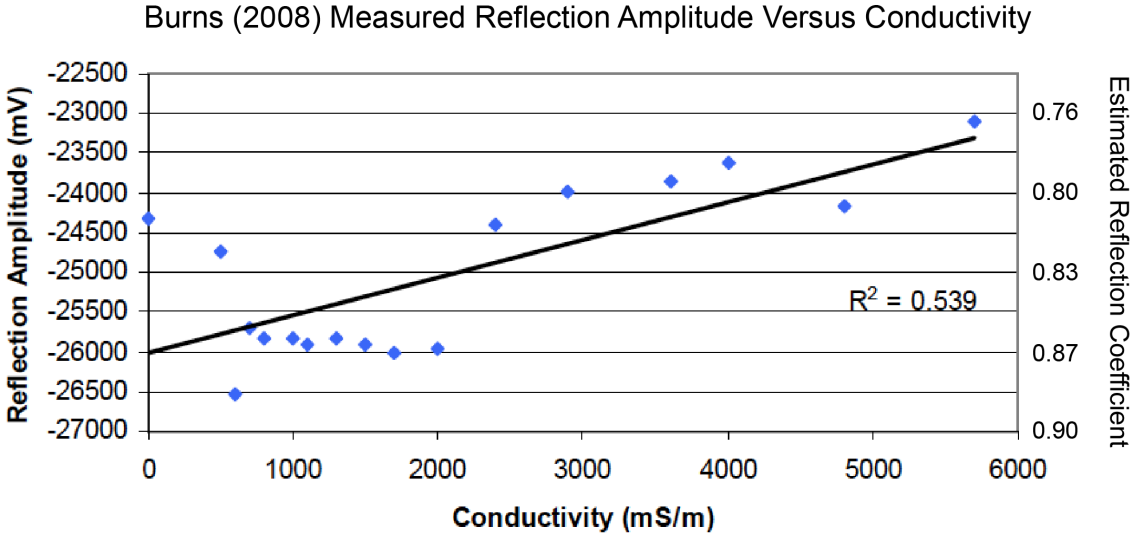

modified from Burns (2008)

Figure C.2. Reflection amplitude versus conductivity for a fracture aperture of 0.5 mm measured by Burns (2008).

Burns interpreted these results originally as a bimodal trend—decreasing amplitude at relatively low conductivities and increasing amplitude at relatively high conductivities. These data points are averaged over ~41 traces, but due to the processing discussed above, do not have a measurement of standard deviation. By looking at the reflection coefficient range, however, the variation at low conductivities appears to be within the standard range of error observed over the results in this study. Furthermore, numerical modeling using GPRMax2D indicates that the behavior of reflection multiples can be inverted from the main reflection—i.e., reflection amplitude decreases with increasing conductivity, as in Burns' results in Figure C.2. Although the absolute value of reflection coefficient is different due to the estimated magnitude of the direct wave and the use of a reflection multiple, reflection coefficient clearly depends on conductivity at these higher conductivities (*see* Figure 3.1). Assuming that the behavior of the reflection multiple is inverted with respect to the actual reflection, the behavior is similar to the results in this study. Combined with the two measurements of reflection coefficients over a 0.5 mm fracture aperture, this demonstrates similar amplitude response to changes in conductivity at a fixed fracture aperture, within the error of the system.

Appendix D: Matlab Scripts for Data Processing

This digital appendix contains all of the Matlab processing scripts for calculating and plotting reflection coefficient and phase from physical analog data, numerical modeling data, and using the theoretical equations. All scripts contain instructions, detail inputs, outputs, and required file formats and are commented to allow for easy modification.

The attached appendix is a .zip file consisting of a folder for each test – fracture aperture and fracture lateral extent – and the relevant scripts are located in each folder under their respective portions of the test – physical analog (PA), theoretical equations (TE), and numerical modeling (NM).

Appendix E: Theoretical Equations for Analytical Models

Theoretical equations for EH and EV mode as defined by both Annan (2005a) and Hollender and Tillard (1998) are presented below. Although these Equations E.3-E.8 were not applied to this research, this appendix is included for completeness and to gather equations from two different publications into a single place.

E.1 Annan (2005a) Equations

For an incident electric field polarized perpendicular to the interface, perpendicular broadside orientation (electric-horizontal (EH) or transverse electric (TE) mode, see Figure A.2), the Fresnel reflection and transmission coefficients are defined as:

$$R_{12} = \frac{Y_1 \cos\theta_i - Y_2 \cos\theta_t}{Y_1 \cos\theta_i + Y_2 \cos\theta_t} \quad \text{(E.1)}$$

$$T_{12} = 1 + R_{12} = \frac{2Y_1 \cos\theta_i}{Y_1 \cos\theta_i + Y_2 \cos\theta_t} \quad \text{(E.2)}$$

where:

$R_{12} = \ reflection\ coefficient\ of\ the\ layer\ 1\ and\ 2\ interface\ (Equation\ E.1)$

$T_{12} = \ transmission\ coefficient\ of\ the\ layer\ 1\ and\ 2\ interface\ (Equation\ E.2)$

$Y_i = wave\ admittance\ (Equation\ 2.4)$

$\theta_i = angle\ of\ incidence$

$\theta_t = angle\ of\ transmission\ (Equation\ 2.6)$

For an incident electric field polarized parallel to the interface, parallel end-fire orientation (electric-vertical (EV) or transverse magnetic (TM) mode, see Figure A.2), the Fresnel reflection coefficient is defined as:

$$R_{12} = \frac{Z_1 \cos\theta_i - Z_2 \cos\theta_t}{Z_1 \cos\theta_i + Z_2 \cos\theta_t} \tag{E.3}$$

$$T_{12} = 1 + R_{12} = \frac{2Z_1 \cos\theta_i}{Z_1 \cos\theta_i + Z_2 \cos\theta_t} \tag{E.4}$$

where:

$Z_i = wave\ impedance\ (Equation\ 2.4)$

E.2 Hollender and Tillard (1998) Equations

For an incident electric field polarized perpendicular to the interface, perpendicular broadside orientation (electric-horizontal (EH) or transverse

electric (TE) mode, see Figure A.2), the Fresnel reflection and transmission coefficients are defined as:

$$R_{12} = \frac{\mu_2 k_1 \cos\theta_i - \mu_1\sqrt{k_2^2 - k_1^2 sin^2\theta_i}}{\mu_2 k_1 \cos\theta_i + \mu_1\sqrt{k_2^2 - k_1^2 sin^2\theta_i}} \quad \text{(E.5)}$$

$$T_{12} = \frac{2\mu_2 k_1 \cos\theta_i}{\mu_2 k_1 \cos\theta_i + \mu_1\sqrt{k_2^2 - k_1^2 sin^2\theta_i}} \quad \text{(E.6)}$$

Where:

$\theta_i = angle\ of\ incidence$

$\mu_i = magnetic\ permeability\ (H/m)$

$k_i = wave\ number\ (m^{-1})\ (Equation\ 2.7 - 2.11)$

For an incident electric field polarized parallel to the interface, parallel end-fire orientation (electric-vertical (EV) or transverse magnetic (TM) mode, see Figure A.2), the Fresnel reflection coefficient is defined as:

$$R_{12} = \frac{\mu_2 k_1\sqrt{k_2^2 - k_1^2 sin^2\theta_i} - \mu_1 k_2^2 \cos\theta_i}{\mu_1 k_2^2 \cos\theta_i + \mu_2 k_1\sqrt{k_2^2 - k_1^2 sin^2\theta_i}} \quad \text{(E.7)}$$

$$T_{12} = \frac{2\mu_2 k_1 k_2 \cos\theta_i}{\mu_1 k_2^2 \cos\theta_i + \mu_2 k_1\sqrt{k_2^2 - k_1^2 sin^2\theta_i}} \quad \text{(E.8)}$$

Appendix F: GPRMax2D

GPRMax2D and 3D are finite-difference, time-domain (FDTD) modeling software developed by Giannopoulos (2005). Users develop a 2D or 3D representation of the subsurface by specifying discretization, dielectric permittivity of layers or targets, source and receiver frequency, position and motion across the model. The software solves Maxwell's equations for a propagating electromagnetic wave at the boundary of each discretized cell.

The software can be downloaded for free at www.gprmax.org for use on a Mac or Windows platform and has an additional graphical user interface (GUI) developed by and available from Sensors and Software. The software manual includes several example input files for the software. All models for this project were run using ASCI input files as opposed to the GUI. Figure F.1 shows an example input file for this system. Model files for each fracture aperture/extent and one fluid conductivity can be found in digital Appendix F. List F.1 presents the software-specific constants (system-specific constants, e.g. dielectric permittivity and GPR frequency are shown in List 2.1).

List F.1. Software-specific constants used for GPRMax2D modeling. For the model volume, Δx and Δy are the discretization in either dimension, and the time window is the length of time recorded by the simulated antennas. For the source, the input wavelet is a standard ricker wavelet with amplitude of 1. Because the GPRMax amplitudes cannot be directly compared to the results from the physical analog and no noise is added to the system, the amplitude is arbitrary. For the media, the values are those recommended by Giannopoulos (2005) and are a reasonable approximation for most natural materials.

Model Volume	Δx (m)	0.0025
	Δy (m)	0.0001
	Time Window (s)	5×10^{-9}
Source	Source Wave Type	Ricker
	Source Amplitude	1
Media	Relative Permittivity at Infinite Frequency, $\varepsilon_{r\infty}$	0
	Relaxation Time of Media, τ (s)	0
	Magnetic Conductivity, σ*	0

```
#medium: 80.0 0.0 0.0 1.6000 1.0 0.0 water
#medium: 2.0 0.0 0.0 0.0000000000001 1.0 0.0 block
#medium: 4.0 0.0 0.0 0.01 1.0 0.0 sand
---------------------------------------------------------------
#domain: 1.266 1
#dx_dy: 0.0025 0.0001
#time_window: 5e-9
---------------------------------------------------------------
#box: 0.0 0.0 1.266 0.6098 block
#box: 0.0 0.4538 1.266 0.4558 water
#box: 0.0 0.0 1.266 0.3522 sand
---------------------------------------------------------------
#line_source: 1.0 1000e6 ricker MyLineSource
---------------------------------------------------------------
#analysis: 1 02p0mm_16p000.out a
#tx: 0.558 0.6098 MyLineSource 0.0 5e-9
#rx: .708 0.6098
#tx_steps: 0.02 0.0
#rx_steps: 0.02 0.0
#end_analysis:
---------------------------------------------------------------
#geometry_file: 02p0mm_16p000.geo
#title: BRE Model 1
#messages: y
```

Figure F.1. Example input file for GPRMax2D. Input files for each aperture and a single conductivity are included in the digital appendix.

VITA

Carolyn M. Tewksbury-Christle conducted research on Venusian geology throughout middle and high school and focused on both geology and physics for her undergraduate degree, researching geology, geophysics, and physics. She graduated with a Bachelor of Arts in Geology and Physics from Smith College in 2007 and commissioned into the United States Air Force.